Terahertz Electrodynamics of Dirac Fermions in Graphene

Terahertz Electrodynamics of Dirac Fermions in Graphene

A dissertation presented

by

Alex James Frenzel

to

the Department of Physics

in partial fulfillment of the requirements

for the degree of

Doctor of Philosophy

in the subject of

Physics

Harvard University

Cambridge, Massachusetts

April 2015

Thesis advisor

Professor Nuh Gedik

Author

Alex James Frenzel

Terahertz Electrodynamics of Dirac Fermions in Graphene

Abstract

Charge carriers in graphene mimic two-dimensional massless Dirac fermions with linear energy dispersion, resulting in unique optical and electronic properties. They exhibit high mobility and strong interaction with electromagnetic radiation over a broad frequency range. Interband transitions in graphene give rise to pronounced optical absorption in the mid-infrared to visible spectral range, where the optical conductivity is close to a universal value $\sigma_0 = \pi e^2/2h$. Free-carrier intraband transitions, on the other hand, cause low-frequency absorption, which varies significantly with charge density and results in strong light extinction at high carrier density. These properties together suggest a rich variety of possible optoelectronic applications for graphene.

In this thesis, we investigate the optoelectronic properties of graphene by measuring transient photoconductivity with optical pump-terahertz probe spectroscopy. We demonstrate that graphene exhibits semiconducting positive photoconductivity near zero carrier density, which crosses over to metallic negative photoconductivity at high carrier density. These observations are accounted for by the interplay between photoinduced changes of both the Drude weight and carrier scattering rate. Our findings provide a complete picture to explain the opposite photoconductivity behavior reported in (undoped) graphene grown epitaxially and (doped) graphene grown by chemical vapor deposition. Our measurements also reveal the non-monotonic temperature dependence of the Drude weight in graphene, a unique property of two-dimensional massless Dirac fermions.

Contents

List of Figures

Acknowledgments

Graduate school is often compared to running a marathon, but in my experience, it is more akin to participating in the World Rally Championship. While the driver of the winning car receives the majority of the praise and recognition, his victory is made possible by a large team of navigators, mechanics, and managers. There are many ups and downs, some epic crashes, and not all participants finish. In the same way, while this dissertation bears my name, it would not have been possible without a massive team working behind the scenes to ensure my success, and completion was not guaranteed at the outset.

I am first and foremost grateful to my research advisor, Professor Nuh Gedik, for the many opportunities he has provided to me over the past several years. He trusted me with the freedom to pursue projects that interested me and gave me the resources to see them through to completion. In this he taught me to be an independent researcher, and for that I thank him.

Gedik group members past and future have also contributed immensely to my graduate career. Working closely with Joshua Lui has truly been a pleasure. He came alongside me early on, when I had a huge pile of data and an aimlessly written manuscript, and showed me how to turn it into a story worth telling. His attention to detail and skill at providing context elevated my work to a higher level of quality. Dan Pilon got me started in the laser lab, introduced me to terahertz spectroscopy, and helped troubleshoot myriad equipment problems. He was also a good companion with whom to suffer through our innumerable laser malfunctions and repairs. My former officemate now professor Darius "the Torch" Torchinsky is the best experimentalist I know and taught me much of what I know about lasers and optics. I have learned so much through sharing many scientific (and otherwise) conversations with Fahad Mahmood, Edbert Sie, Ozge Ozel, David Hsieh, Changmin Lee, Mahmoud Ghulman, Inna Vishik, Timm Rohwer, and James McIver. I also need to acknowledge Wilfredo Gonzalez, our Spectra-Physics laser service engineer, who

made this dissertation possible by keeping the amplifier up and running when it seemed determined to ruin me.

My other committee members, Prof. Jenny Hoffman and Prof. Subir Sachdev, graciously shared their time to meet with me and made sure research was progressing satisfactorily. Monica Wolf and Lisa Cacciabaudo, administrators at MIT and Harvard, were instrumental in making my dual-institution graduate school experience as smooth as possible. Former Harvard administrator Sheila Ferguson's admonition, "Don't give up easy," helped keep me going when research was difficult.

I certainly could not have done any of the work presented in this thesis without samples. Yong Cheol Shin and Wenjing Fang in the group of Jing Kong at MIT generously provided high-quality CVD graphene samples, assisted with characterization, and creatively solved fabrication challenges. Aside from obtaining graphene, I also had to fabricate the samples into devices, a task completely outside the expertise of my group. Without the patience and generosity of Valla Fatemi, Javier Sanchez-Yamagishi, Qiong Ma, Hadar Steinberg, Patrick Herring, and Nathan Gabor in Pablo Jarillo-Herrero's group, this would not have been possible. They taught me everything I know about device fabrication, trained me to use their lab equipment, helped me troubleshoot measurements, and put up with endless questions from me. My research would not have been successful without their help.

I am grateful to the many other mentors I have had over the years. Prof. Dimitri Basov and his students Omar Khatib, Drew LaForge, Brian Chapler and Alex Schafgans at UC San Diego first introduced me to research in condensed matter physics and have continued to graciously share their time and wisdom with me. Dimitri's postdoc Mumtaz Qazilbash (now professor at College of William and Mary) walked me through my first publication as lead author. Prof. Dan Arovas provided me with a solid foundation in statistical physics, and his lecture notes for several classes have served as indispensable

references throughout my graduate career. Prof. David Lee of Gordon College and Mr. Rob Lapointe of Lutheran High School of Orange County first got me interested in physics and set me on this path.

My many friends at Harvard have greatly enriched my graduate experience. Justin Song, my fellow defector to MIT, first introduced me to graphene and was a great friend to have on campus, to play frisbee and eat lunch with. Living at 21 Mellen with Tout Wang, Tony Jia, Carl Erickson, Dan Huang, and Mithun Mansinghani was a thoroughly enjoyable experience. Mike Yee, Elise Novitski, and Alex Thomson, along with Justin, always helped me get out of the lab to eat fine food and share good conversation. Gary Sing and Andrew Mao from the Harvard Graduate Christian Community have been consistent friends since they first helped me get settled at Harvard.

My community at Park Street Church has served as a solid foundation for me during my time in graduate school. It has been a blessing to share life with my friends Seth van Liew, Dan Cogswell, Adam Kurihara, Chris Pletcher, Jonathan Baker, Andrew Noh, Matt Carey, Andy Huss, Ben Shuleva, Bryan Collins, Dan Fehlauer, Andy Hopper, Nathan Hancock and many others.

My family perhaps played the most significant role in my successful completion of graduate school. My parents, Larry and Shawna, taught me how to work hard and persevere by their example. I am exceedingly thankful for their unconditional love and support. My brothers and sisters Jason, Whitney, Kyle, Kayla, Allison, Lauren, Ed, and Sam, my niece Mariah, and my nephew Jamil have made my visits to California so much more rejuvenating, and I am thankful for the time we were able to spend together in Cambridge during their visits.

My wife, Amy, has been more loving, encouraging, and supportive, than I could have ever asked. I am so proud of her and so thankful for her.

To my parents, Larry and Shawna.

Chapter 1

Introduction

Two-dimensional graphene is characterized by its distinctive Dirac electronic structure and the associated remarkable optical properties, specifically, a strong and broadband optical absorption from far-infrared to ultraviolet wavelengths [1–4]. The unique absorption spectrum of graphene, together with the great tunability of its Fermi level by electrical gating, has made it a promising material for next-generation optoelectronic applications [5–7]. For instance, it exhibits superior functionality as an ultrafast photodetector [8, 9] and photothermoelectric midinfrared sensor [10]. Additionally, it has been demonstrated to efficiently modulate incident terahertz (THz) radiation [**?**, 11–15], which has recently led to the fabrication of graphene-based THz detectors [16–18]. To further optimize these optoelectronic devices, it is important to understand the fundamental physics underlying graphene photodetection.

Optoelectronic properties are most often characterized by performing transport and photocurrent experiments. A wealth of information has been gained from such experiments. For example, scanning photocurrent experiments have disentangled the relative importance of photothermoelectric [19–22] and photovoltaic [23] contributions to photocurrent generation in inhomogeneous graphene devices. In these experiments, however, contacts

and engineered inhomogeneities play dominant roles in the observed phenomenon and can mask intrinsic properties of light-matter interaction in graphene [24]. Additionally, intrinsic limits for high frequency device operation are often estimated by extrapolation [8, 9]. Access to intrinsic optoelectronic properties on characteristic ultrafast timescales in graphene would greatly enhance our knowledge and ability to optimize optoelectronic devices based on graphene.

Time resolved terahertz spectroscopy [24, 25] is capable of measuring the high-frequency transport properties of graphene without the complications of proximal contacts [26, 27]. Additionally, it can be incorporated into ultrafast measurements to examine the effects of optical excitation on the transport properties with sub-picosecond time resolution [24, 25, 28]. In this dissertation, we apply this technique to study optoelectronic properties of Dirac fermion quasiparticles in graphene. We demonstrate electrical control over the sign of the photoconductive response of graphene and report our discovery of unconventional photoconductivity mechanisms in this unique two-dimensional material.

This dissertation is structured as follows. We first provide relevant introductory information about graphene, focusing on salient transport properties which will be important in the analysis of our experiments. We then introduce optical spectroscopic measurements and discuss mechanisms which give rise to optical absorption in graphene. Next, we discuss the experimental techniques used for the optoelectronic measurements presented in this dissertation, highlighting technical improvements made in our lab during the course of this work. We then present initial measurements of the anomalous negative photoconductive properties of doped graphene. Finally, we demonstrate control over these properties using electrical gating and discuss the properties of quasiparticles in graphene which give rise to the observed phenomena.

Chapter 2

Background: graphene and electrodynamics of solids

2.1 Electronic properties of graphene

Many of graphene's spectacular transport and optical properties are a direct consequence of its unique electronic band structure. The strict confinement of carriers to two dimensions also has a profound impact on graphene's physical properties. In this section, we review the elementary electronic properties of graphene.

2.1.1 Graphene lattice in real and reciprocal space

Graphene is a two-dimensional (2D) honeycomb lattice of carbon atoms. The real-space structure of the lattice is shown in Fig. 2.1. The honeycomb lattice is not a Bravais lattice, but comprises a triangular lattice with a two-atom basis [2,3]. Alternatively, it can be viewed as two interpenetrating triangular sublattices, designated A and B. In Fig. 2.1, the atoms on the A sublattice are colored light grey, while atoms on the B sublattice are colored dark grey. The lattice primitive vectors are $\boldsymbol{a}_1 = a_0\sqrt{3}\hat{y}$ and $\boldsymbol{a}_2 = a_0\sqrt{3}\left[(3/2)\hat{x} + (1/2)\hat{y}\right]$, where $a_0 = 1.42\,\text{Å}$ is the carbon-carbon distance. These vectors are shown in Fig. 2.1 as black

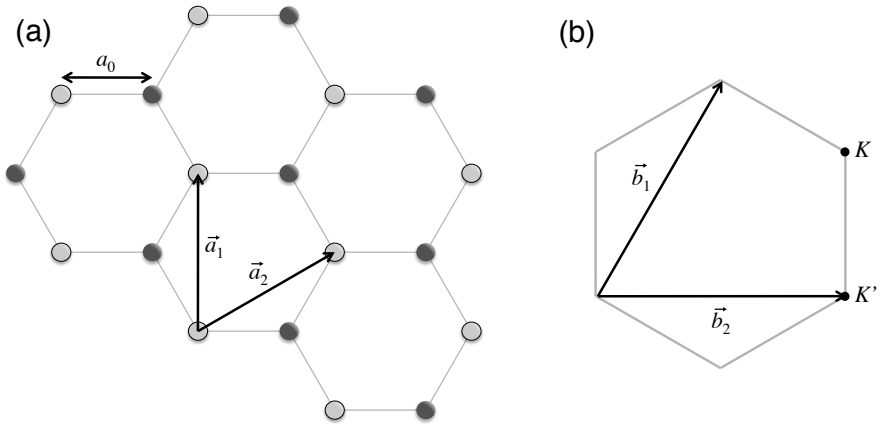

Figure 2.1: Graphene structure in real and reciprocal space. (a) Real space lattice structure. Carbon atoms on the A sublattice are light grey, while atoms on the B sublattice are dark grey. The two primitive lattice vectors $\boldsymbol{a}_1$ and $\boldsymbol{a}_2$ are shown as black arrows. The carbon-carbon distance is denoted by a_0. (b) Brillouin zone in reciprocal space. .

arrows. The lattice basis vectors are $\boldsymbol{\tau}_1 = 0$ and $\boldsymbol{\tau}_2 = a_0\left[(1/2)\hat{x} + (\sqrt{3}/2)\hat{y}\right]$.

The reciprocal lattice vectors can be found in the usual way [29] to be $\boldsymbol{b}_1 = (2\pi/3a_0)(\hat{x} + \sqrt{3}\hat{y})$ and $\boldsymbol{b}_2 = (4\pi/3a_0)\hat{x}$. The reciprocal lattice for graphene is therefore also a honeycomb, but rotated by 90° relative to the real-space lattice. The first Brillouin zone is a hexagon with corners at $\boldsymbol{k}_{1,2} = (2\pi/3a_0)(\hat{x} \pm \hat{y}/\sqrt{3})$. These two points are known as the K and K' points of the Brillouin zone, respectively. All other Brillouin zone corners can be mapped to one of these two points by a reciprocal lattice vector and hence are equivalent to either K or K'. No reciprocal lattice vector connects K to K', however, so these two points in momentum space represent distinct electronic wave vectors. Quasiparticles occupying states near the K (K') points are said to occupy the K (K') valley. The Brillouin zone boundary is shown in red in Fig. 2.2.

2.1.2 Tight-binding model for electronic band structure

Each carbon atom in the graphene lattice has six electrons. Two electrons fill a closed $1s$ shell, while three of the remaining electrons form three sp^2 covalent bonds with neighboring carbon atoms. A single p_z orbital remains occupied at each lattice site. The two p_z orbitals on neighboring carbon atoms hybridize to form bonding (π) and anti-bonding (π^*) states. The lattice periodicity causes these orbitals to merge into a valence and conduction band of electronic states. Each carbon atom in the lattice contributes one electron that is free to fill these bands. As a result, intrinsic graphene possesses a completely filled valence band and a completely empty conduction band [2, 3].

The electronic band structure of graphene was first calculated by Wallace in 1947 [30]. It can be easily obtained using the tight binding method [29] by considering the p_z orbitals ϕ_{p_z} at each carbon site. One constructs a tight binding wavefunction of the following form:

$$\psi_{\boldsymbol{k}} = \frac{1}{\sqrt{N}} \sum_{i,\alpha} c_\alpha \phi_{p_z}(\boldsymbol{r} - \boldsymbol{r}_{i,\alpha}) e^{i\boldsymbol{k}\cdot\boldsymbol{r}_{i,\alpha}} \equiv \sum_\alpha c_\alpha \chi^\alpha_{\boldsymbol{k}}(\boldsymbol{r}), \tag{2.1}$$

where N is the number of lattice sites, $\boldsymbol{r}_{i,\alpha} = \boldsymbol{r}_i + \boldsymbol{\tau}_\alpha$ are the vectors connecting different lattice sites, $\{c_\alpha\}$ are undetermined coefficients, and we have defined $\chi^\alpha_{\boldsymbol{k}}(\boldsymbol{r}) = \frac{1}{\sqrt{N}} \sum_i \phi_{p_z}(\boldsymbol{r} - \boldsymbol{r}_{i,\alpha}) e^{i\boldsymbol{k}\cdot\boldsymbol{r}_{i,\alpha}}$. To obtain the tight-binding Hamiltonian and wave functions, we insert this trial wavefunction into the Schrodinger equation $\mathcal{H}\,|\psi\rangle = \varepsilon\,|\psi\rangle$ and multiply on the left by $\langle\chi^\alpha_{\boldsymbol{k}}|$ to yield the eigenvalue equation

$$\langle\chi^\alpha_{\boldsymbol{k}}|\,\mathcal{H}\,|\psi\rangle = c_\alpha \varepsilon, \tag{2.2}$$

where we have used the fact that $\langle\chi^\alpha_{\boldsymbol{k}}|\psi\rangle = c_\alpha$. To solve Eq. (2.2), we need to calculate the matrix elements

$$\langle\chi^\alpha_{\boldsymbol{k}}|\,\mathcal{H}\,|\psi\rangle = \frac{1}{N} \sum_{i,j} \sum_{\alpha'} c_{\alpha'} e^{i\boldsymbol{k}\cdot(\boldsymbol{r}_{j,\alpha'} - \boldsymbol{r}_{i,\alpha})} \int d\boldsymbol{r}\, \phi^*_{p_z}(\boldsymbol{r} - \boldsymbol{r}_{i,\alpha}) \mathcal{H} \phi_{p_z}(\boldsymbol{r} - \boldsymbol{r}_{j,\alpha'}). \tag{2.3}$$

If we set the on-site energy to zero such that $\langle\phi_{p_z}|\mathcal{H}|\phi_{p_z}\rangle = 0$ and restrict our calculation to nearest-neighbor interactions, the right hand side vanishes unless $\alpha \neq \alpha'$. We define the hopping parameter $t \equiv \int d\boldsymbol{r}\phi^*_{p_z}(\boldsymbol{r}-\boldsymbol{r}_{i,\alpha})\mathcal{H}\phi_{p_z}(\boldsymbol{r}-\boldsymbol{r}_{j,\alpha'})$ for $\alpha \neq \alpha'$ and note that nearest neighbors are located at $\pm(\boldsymbol{\tau}_2 - \boldsymbol{r}_j)$. Then, performing the sum over i in Eq. (2.3), we obtain

$$\langle\chi^\alpha_{\boldsymbol{k}}|\,\mathcal{H}\,|\psi\rangle = t\sum_j e^{i(-1)^\alpha \boldsymbol{k}\cdot(\boldsymbol{\tau}_2-\boldsymbol{r}_j)}\sum_{\alpha'\neq\alpha} c_{\alpha'}. \tag{2.4}$$

Using this matrix element, Eq. (2.2) can be rewritten in matrix form as

$$\begin{pmatrix} 0 & t\sum_j e^{-i\boldsymbol{k}\cdot(\boldsymbol{a}_j-\boldsymbol{\tau}_2)} \\ t\sum_j e^{i\boldsymbol{k}\cdot(\boldsymbol{a}_j-\boldsymbol{\tau}_2)} & 0 \end{pmatrix}\begin{pmatrix} c_1 \\ c_2 \end{pmatrix} = \varepsilon(\boldsymbol{k})\begin{pmatrix} c_1 \\ c_2 \end{pmatrix} \tag{2.5}$$

where $\boldsymbol{a}_j = \{0,\, \boldsymbol{a}_1,\, \boldsymbol{a}_2\}$. Diagonalizing the matrix on the left-hand side yields the dispersion relations for the valence and conduction bands,

$$\varepsilon(\boldsymbol{k}) = \pm t\sqrt{3 + 2\cos(k_y a_0\sqrt{3}) + 4\cos(3k_x a_0/2)\cos(k_y a_0\sqrt{3}/2)}. \tag{2.6}$$

A plot of the resulting band structure is shown in Fig. 2.2.

The simple band structure described by Eq. (2.6) features extraordinary properties. The valence and conduction bands are degenerate at the K and K' points with $\varepsilon = 0$. Away from these points in $\boldsymbol{k}-$space, known as the Dirac points (DP), the dispersion is linear, *e.g.*, $\varepsilon(\boldsymbol{k}) = \frac{3}{2}a_0 t|\boldsymbol{k}-\boldsymbol{K}|$ for the K valley. This is analogous to the dispersion relation for massless relativistic particles, $\varepsilon(\boldsymbol{k}) = \hbar c|\boldsymbol{k}|$, where $c = 3\times10^8$ m/s is the speed of light. Indeed, one can write down a low-energy Dirac approximation to the tight-binding Hamiltonian around the K and K' valleys in the form

$$\mathcal{H}_{\rm D} = \hbar v_{\rm F}\boldsymbol{k}\cdot\boldsymbol{\sigma} = \hbar v_{\rm F}\begin{pmatrix} 0 & k_x - ik_y \\ k_x + ik_y & 0 \end{pmatrix}, \tag{2.7}$$

where $\boldsymbol{\sigma}$ is a vector of Pauli matrices and $v_{\rm F} = \frac{3}{2}a_0 t/\hbar$. For graphene, $t \approx$2.5 eV, so $v_{\rm F} \approx c/300$ [2, 3]. The effective Dirac Hamiltonian $\mathcal{H}_{\rm D}$ is easily diagonalized to obtain the

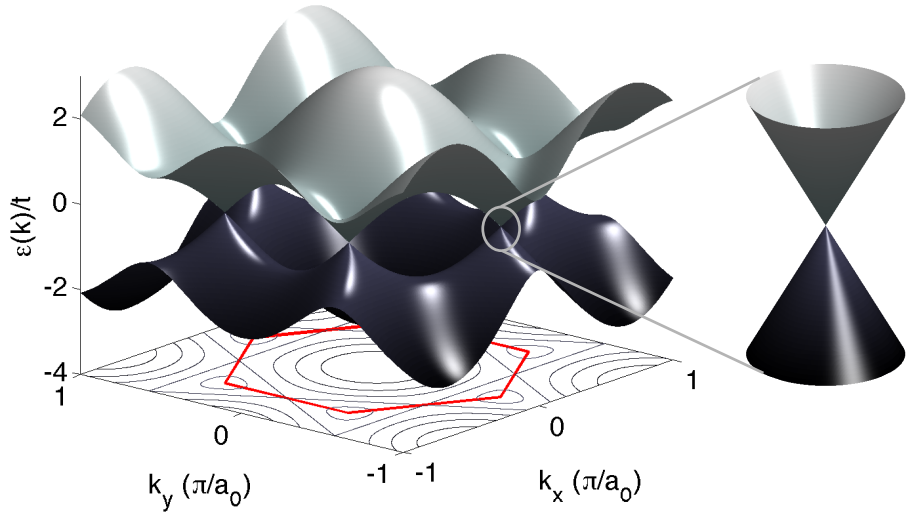

Figure 2.2: Graphene tight binding bands. The boundary of the first Brillouin zone is shown in red. The valence and conduction bands meet at zero energy at the corners of the Brillouin zone. Around these points, the dispersion is approximately linear and conical.

eigenvalues $\varepsilon(\boldsymbol{k}) = \pm\hbar v_{\mathrm{F}}|\boldsymbol{k}|$. The eigenstates are two component spinors [2, 3, 31]

$$|\psi\rangle = \frac{1}{\sqrt{2}} \begin{pmatrix} 1 \\ \pm e^{i\theta_k} \end{pmatrix} e^{i\boldsymbol{k}\cdot\boldsymbol{r}}, \tag{2.8}$$

where $\theta_k = \tan^{-1}(k_y/k_x)$ and the upper (lower) component corresponds to the probability amplitude to find the electron on the A (B) sublattice [2, 3]. The Dirac approximation is valid for energies $|\varepsilon| \lesssim 0.4t \approx 1$ eV and therefore provides an excellent framework to describe transport and optical phenomenon in graphene [2,3]. The linear dispersion relation also results in a density of states that depends linearly on energy, $g(\varepsilon) = 2|\varepsilon|/\pi(\hbar v_{\mathrm{F}})^2$, which has many important implications for physics in graphene. The eigenstates [Eq. (2.8)] can be used to calculate transport and optical properties of graphene, including its interband optical conductivity and the coupling of electrons to phonons.

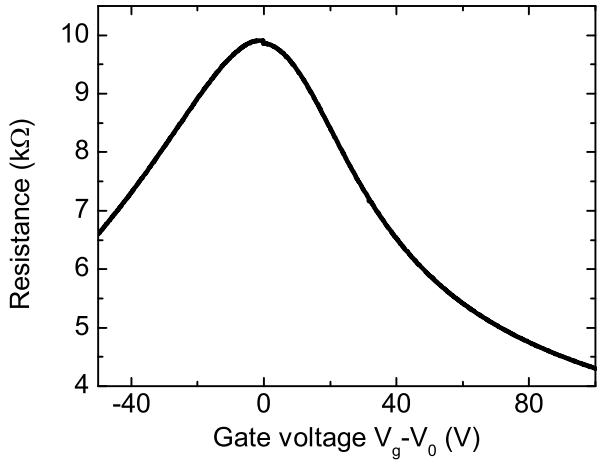

Figure 2.3: Ambipolar resistance modulation in a graphene device. The resistance $R(V_g)$ was measured in a two-terminal geometry. The peak at $V_g - V_0 = 0$ corresponds to the charge neutrality point (CNP), where $\varepsilon_F = n = 0$. As electrons ($V_g > 0$) or holes ($V_g < 0$) are added to the graphene sheet, the resistance decreases from its maximum value.

2.1.3 Transport properties

The electronic structure described above, along with the strict confinement of carrier motion to two dimensions, leads to several unique and remarkable electronic properties. A graphene sheet is straightforwardly incorporated into a field-effect transistor geometry, after which the carrier density in the sample can be easily tuned by application of a gate voltage [1,32]. The zero-gap band structure allows the ability to easily tune between electron and hole carriers, in contrast to gapped conventional two-dimensional electron gases (2DEGs) [3]. This allows one to measure sample properties as a function of carrier type and density. Ambipolar resistance modulation, in which the resistance peaks when the gate voltage minimizes the carrier density, but decreases when either electrons ($V_g > 0$) or holes ($V_g < 0$) are introduced to the system, allows calibration of the absolute carrier density. Fig. 2.3 shows an example of ambipolar resistance modulation measured on a device in our lab. The minimum carrier density [known as the charge neutrality point (CNP)] occurs at $V_g - V_0 = 0$.

Electron-phonon interaction contributes to both momentum and energy relaxation

in graphene [33–38]. Acoustic phonons are likely the dominant scattering mechanism in ultra-clean graphene [34, 39, 40], and contribute a small amount to scattering in normal graphene samples at room temperature [41, 42]. Optical phonon scattering is largely suppressed at room temperature because the phonon energies are extremely high, around 200 meV [2, 3]. At elevated electronic temperatures, however, two subsets of optical phonons (one with energy ∼190 meV at Γ, the other with energy ∼150 meV at K) couple strongly to quasiparticles [33, 36, 43, 44]. These effects have been observed in nonlinear transport experiments [45–47] and in ultrafast pump-probe measurements [33, 44]. In ultrafast optical measurements, quasiparticles in graphene can reach extremely high temperatures after photoexcitation, which allows them to couple efficiently to optical phonons. This has been observed in graphene and graphite both by elevated scattering rates [33, 48] and elevated nonequilibrium phonon populations after photoexcitation [49–51].

As we will discuss below in connection with intraband conductivity of solids (§2.2.1), the dc conductivity at low temperature is given by

$$\sigma_{\mathrm{dc}} = \frac{e^2 v_{\mathrm{F}}^2}{2} g(\varepsilon_{\mathrm{F}}) \tau(\varepsilon_{\mathrm{F}}), \tag{2.9}$$

where $g(\varepsilon_{\mathrm{F}})$ and $\tau(\varepsilon_{\mathrm{F}})$ are the density of states and the transport scattering time at the Fermi level, respectively [3]. Most experimental measurements of graphene's dc conductivity observe $\sigma_{\mathrm{dc}} \propto n$, where n is the gate-controlled carrier density in the sample [2,3,32,52] (except in exceptionally clean devices [39,40]). This, combined with the fact that $g(\varepsilon_{\mathrm{F}}) \propto \varepsilon_{\mathrm{F}} \propto \sqrt{n}$, suggests that $\tau(\varepsilon_{\mathrm{F}}) \propto \varepsilon_{\mathrm{F}}$. Such a density-dependent scattering time is consistent with charged impurity-dominated momentum relaxation in most devices [3, 52–54]. In contrast to semiconductor 2DEGs, where optical phonon scattering dominates at room temperature, charged impurity scattering limits mobility in most graphene samples even at room temperature [3].

2.2 Electrodynamics of solids

Optical measurements provide a powerful tool for investigating the electronic properties of solids. For example, they are invaluable in studying band structure through interband absorption [55], as well as electronic transport properties and interactions [56]. In this section, we describe features of optical properties of graphene in the infrared range of the electromagnetic spectrum and discuss their relevance to the work presented in this dissertation.

2.2.1 Drude model for free carrier electrodynamics

The Drude model for the electrodynamic response of free charge carriers is widely successful in describing the low-energy electrodynamics of metals and doped semiconductors, despite initially being derived from a purely classical model [55–57]. In Drude's original formulation, he considered electrons in a solid as point particles free to move in a lattice of stationary ions. The ions were also treated as point particles [29, 58]. He assumed that the electrons collided with the ions, with an average time interval τ between collisions. Further, each collision randomly oriented the direction of the electrons' velocity. The speed of an electron after a collision was set by the Maxwell distribution.

In the presence of a spatially homogeneous, time-dependent external electric field $\mathbf{E}(t) = E(t)\hat{x} = E_0 e^{-i\omega t}\hat{x}$, the classical equation of motion for the electron momentum p in the x coordinate is

$$\dot{p} = -\Gamma p - eE(t), \tag{2.10}$$

where $\Gamma = 1/\tau$ is the damping rate introduced by collisions with the static ions. This differential equation can be easily solved by Fourier transformation,

$$-i\omega p(\omega) = -\Gamma p(\omega) - eE_0. \tag{2.11}$$

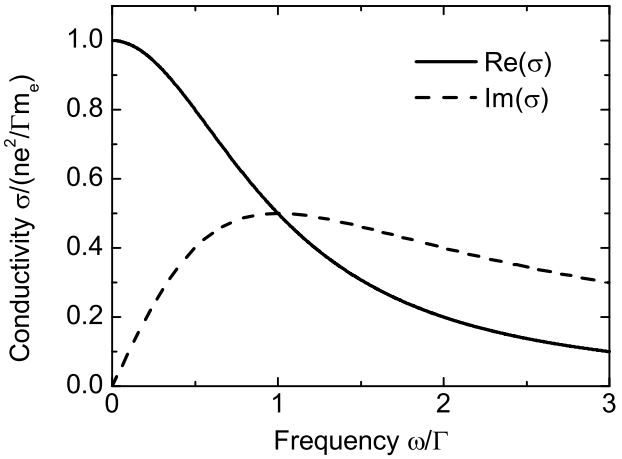

Figure 2.4: Real (solid) and imaginary (dashed) parts of the Drude conductivity. The real part is a Lorentzian function centered at $\omega = 0$. The real and imaginary parts are equal at $\omega = \Gamma$, and the area under the real part for $\omega > 0$ is $(\pi/2)(ne^2/m_e)$.

Solving for p, we find

$$p(\omega) = \frac{-eE_0}{\Gamma - i\omega}. \tag{2.12}$$

To relate this expression for momentum to the conductivity, we first note that the classical momentum of an electron is related to its velocity v by $p = m_e v$ (m_e is the bare electron mass). Additionally, the charge current is given by $j(\omega) = -nev = -nep(\omega)/m_e \equiv \sigma(\omega)E_0$, where n is the density of electrons in the material. Combining these relations with Eq. (2.12), we arrive at an expression for the ac conductivity of the electron system:

$$\tilde{\sigma}(\omega) = \sigma_1(\omega) + i\sigma_2(\omega) = \frac{ne^2}{m_e}\frac{1}{\Gamma - i\omega}. \tag{2.13}$$

This function describes a complex Lorentzian centered at zero frequency, shown in Fig. 2.4. The half-width at half-maximum of the real part of the Lorentzian is equal to the scattering rate Γ. When $\omega = \Gamma$, $\sigma_1 = \sigma_2 = \max[\sigma_2(\omega)]$. Additionally, the area under $\sigma_1(\omega)$ is equal to $(\pi/2)(ne^2/m_e)$. This will be discussed in more detail later in the context of sum rules and conservation of spectral weight (§2.2.3).

While originally derived classically, the Drude form for $\tilde{\sigma}(\omega)$ also arises as a limiting

case of the semiclassical Boltzmann expression for conductivity, as well as from the fully quantum Kubo formula. We sketch the derivations here. The Boltzmann expression for conductivity in 3 dimensions within the relaxation-time approximation is given by [29,59,60]

$$\tilde{\sigma}(\omega) = Ne^2 \int \frac{d^3k}{(2\pi)^3} \frac{v^2(\boldsymbol{k})}{3} \frac{1}{\Gamma(\varepsilon(\boldsymbol{k})) - i\omega} \left(-\frac{\partial f^0}{\partial \varepsilon}\right) \tag{2.14}$$

where N is the degeneracy, $\boldsymbol{v}(\boldsymbol{k}) = \hbar^{-1}\partial\varepsilon/\partial\boldsymbol{k}$ is the carrier band velocity, $\Gamma(\varepsilon(\boldsymbol{k})) = 1/\tau(\varepsilon(\boldsymbol{k}))$ is the energy-dependent relaxation rate, f^0 is the Fermi distribution, and we have considered an isotropic system so that $\left\langle v^\alpha(\boldsymbol{k}) v^\beta(\boldsymbol{k})\right\rangle = v(\boldsymbol{k})^2/3$. For a Fermi system with parabolic dispersion, $v^2(\boldsymbol{k}) = 2\varepsilon/m^*$, with $(m^*)^{-1} = \hbar^{-2}\partial^2\varepsilon(\boldsymbol{k})/\partial\boldsymbol{k}^2$ the effective mass of the charge carriers. A change of variables from $\boldsymbol{k}$ to ε yields

$$\tilde{\sigma}(\omega) = \frac{2e^2}{3m^*} \int d\varepsilon g(\varepsilon)\varepsilon \frac{1}{\Gamma(\varepsilon) - i\omega} \left(-\frac{\partial f^0}{\partial \varepsilon}\right), \tag{2.15}$$

where the density of states $g(\varepsilon)$ is defined by

$$g(\varepsilon) = N \int \frac{d^3k}{(2\pi)^3} \delta(\varepsilon - \varepsilon(\boldsymbol{k})). \tag{2.16}$$

When the temperature is low relative to the Fermi energy, the Fermi function is approximately a step function, and $\left(-\partial f^0/\partial\varepsilon\right) \approx \delta(\varepsilon - \varepsilon_{\mathrm{F}})$. In many metals, $\varepsilon_{\mathrm{F}} \sim$ 1-10 eV, so the condition that $k_{\mathrm{B}}T \ll \varepsilon_{\mathrm{F}}$ is easily satisfied at most experimentally relevant temperatures. This allows us to evaluate the integral and reveals that the physics is determined by the Fermi surface properties. For fermions with ballistic dispersion and twofold spin degeneracy, $g(\varepsilon) = (3/2)n/\varepsilon_{\mathrm{F}}$ [60], so we recover the Drude form

$$\tilde{\sigma}(\omega) = \frac{ne^2}{m^*} \frac{1}{\Gamma(\varepsilon_{\mathrm{F}}) - i\omega}. \tag{2.17}$$

Here the free electron mass of the original Drude model has been replaced by the band mass of quasiparticles in the solid and the scattering rate is the scattering rate at the Fermi energy. Taking the $\omega \to 0$ limit recovers the formula for the dc conductivity in Eq. (2.9).

The Boltzmann result is notably different for the 2D massless Dirac fermions in graphene. For these quasiparticles, $\varepsilon(\boldsymbol{k}) = \hbar v_{\mathrm{F}}|\boldsymbol{k}|$, $\boldsymbol{v}(\boldsymbol{k}) = v_{\mathrm{F}}\hat{\boldsymbol{k}}$, and $g(\varepsilon) = 2|\varepsilon|/\pi(\hbar v_{\mathrm{F}})^2$, as we noted above in §2.1.2. Additionally, it is important to consider the finite temperature case because graphene can easily be tuned between the $\varepsilon_{\mathrm{F}} \gg k_{\mathrm{B}}T$ and $\varepsilon_{\mathrm{F}} \ll k_{\mathrm{B}}T$ regimes with an electrostatic back gate. We therefore cannot simply approximate the derivate of the Fermi function as a delta function. In this case we begin with Eq. (2.14) modified for a 2D massless Dirac system, which takes the form

$$\tilde{\sigma}(\omega) = \frac{Ne^2v_{\mathrm{F}}^2}{2}\int \frac{d^2k}{(2\pi)^2}\frac{1}{\Gamma(\varepsilon(\boldsymbol{k})) - i\omega}\left(-\frac{\partial f^0}{\partial \varepsilon}\right). \tag{2.18}$$

We can use the identity $(-\partial f^0/\partial\varepsilon) = f^0(\varepsilon)[1 - f^0(\varepsilon)]/k_{\mathrm{B}}T$ and the assumption that Γ is independent of energy to evaluate the integral, resulting in

$$\tilde{\sigma}(\omega) = \frac{2e^2}{\pi\hbar^2}k_{\mathrm{B}}T\ln\left[2\cosh\left(\frac{\mu(T)}{2k_{\mathrm{B}}T}\right)\right]\frac{1}{\Gamma - i\omega} \equiv \frac{D}{\pi}\frac{1}{\Gamma - i\omega}, \tag{2.19}$$

where D is known as the Drudge weight [11]. When the density is nonzero and the temperature is low compared to the chemical potential $\mu(T)$, then $D \approx (e^2/\hbar^2)\mu(T)$. This differs from the normal metallic case, where $\sigma \propto n$, independent of temperature [Eq. 2.17]. In contrast, for Dirac fermions, the conductivity explicitly depends on temperature, and $\sigma \propto \mu \propto \sqrt{n}$. In the limit of vanishing density ($\mu \to 0$), $D \propto k_{\mathrm{B}}T$. Wallace calculated that $n \propto T^2$ for undoped graphene [30], so here too $D \propto \sqrt{n}$. A plot of D as a function of temperature at different carrier densities is shown in Fig. 2.5. A more detailed calculation of D for graphene and comparison with conventional materials is presented in §6.2.2. It is also important to note that, while Eq. (2.19) predicts $\sigma_{\mathrm{dc}} = 0$ for $\varepsilon_{\mathrm{F}} = 0$ and $T = 0$, several theoretical studies predict a nonzero "minimal conductivity" even at zero temperature and density [3]. The controversy surrounding the minimal conductivity in graphene does not play a role in the analysis of our experiments, which were all performed at room temperature or above. We also note that, for graphene, the scattering rate $\Gamma/2\pi$ typically lies in the

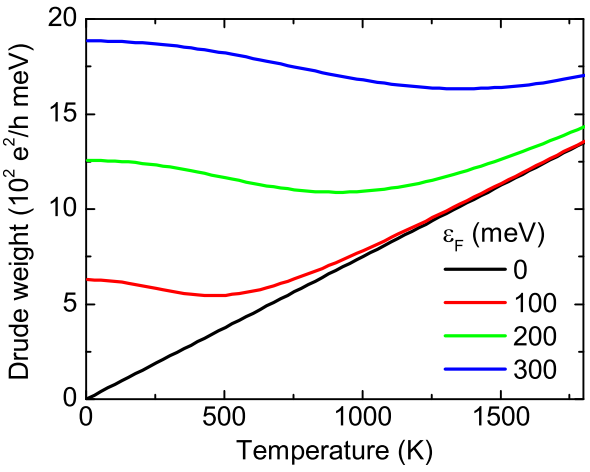

Figure 2.5: Drude weight D for pristine graphene as a function of temperature at different values of the Fermi energy ε_F, calculated using Eq. (2.19). For completely undoped graphene, D increases linearly with temperature. At very high densities ($\varepsilon_F \gg k_B T$), D decreases quadratically with temperature. When $\varepsilon_F \sim k_B T$, however, D depends non-monotonically on temperature.

terahertz frequency range (∼10 meV) [11–14, 61].

Finally, the Drude form for intraband conductivity can be obtained in a fully quantum treatment. The Kubo formula relates the conductivity response function to current fluctuations in the system in thermal equilibrium, and can be easily derived using Fermi's Golden Rule [55, 57, 62]. For a zero-temperature Fermi system interacting with an electromagnetic field, the transition rate is

$$W = \frac{2\pi}{\hbar} \sum_n |\langle n| \mathcal{H}_{\text{int}} |0\rangle|^2 \delta(\hbar\omega - \varepsilon_n + \varepsilon_0) \tag{2.20}$$

where $\{|n\rangle\}$ are the excited states of the system, $|0\rangle$ is the ground state (Fermi sea), $\mathcal{H}_{\text{int}} = -\int d\boldsymbol{r}\mathbf{J}(\boldsymbol{r})\cdot\mathbf{A}(\boldsymbol{r})$ describes the interaction between the system and the electromagnetic field, and ε_n and ε_0 are the energies of the excited states and ground state, respectively. Here, the electric field is given by $\mathbf{E}(\boldsymbol{r},t) = -\partial\mathbf{A}(\boldsymbol{r},t)/\partial t$, where $\mathbf{A}(\boldsymbol{r},t)$ is the vector potential in the Coulomb gauge ($\nabla\cdot\mathbf{A} = 0$), and $\mathbf{J}(\boldsymbol{r}) = -(e/2)\sum_i[\boldsymbol{v}_i\delta(\boldsymbol{r}-\boldsymbol{r}_i) + \delta(\boldsymbol{r}-\boldsymbol{r}_i)\boldsymbol{v}_i]$ is the current operator [62].

For a monochromatic plane wave, $\mathbf{A}(\boldsymbol{r},t) = (i/\omega)\mathbf{E}(\boldsymbol{r},t) = (i/\omega)\mathbf{E}_0 \exp[i(\boldsymbol{q}\cdot\boldsymbol{r}-\omega t)]$ and $\mathcal{H}_{\rm int} = -(i/\omega)e^{-i\omega t}\tilde{\mathbf{J}}^*_{\boldsymbol{q}}\cdot\mathbf{E}_0$. Here $\tilde{\mathbf{J}}_{\boldsymbol{q}} = \int d\boldsymbol{r}\mathbf{J}(\boldsymbol{r})\exp(-i\boldsymbol{q}\cdot\boldsymbol{r})$ is the Fourier transform of the current operator. The transition rate then becomes

$$W = \frac{2\pi}{\hbar^2\omega}E_0^2\sum_n \frac{|\langle n|\,\tilde{J}^*_{\boldsymbol{q}}\,|0\rangle|^2}{\omega_n-\omega_0}\delta(\omega-\omega_n+\omega_0) \tag{2.21}$$

where $\omega_i = \varepsilon_i/\hbar$ and we have restricted our attention to the case where the current is parallel to the applied field. Anticipating the result, we have also written $(1/\omega^2)$ from the matrix element as $1/[\omega(\omega_n-\omega_0)]$, since the δ-function requires that $\omega = \omega_n - \omega_0$. We next use the identity $\delta(\omega-\omega_n+\omega_0) = (1/2\pi)\int dt\exp[i(\omega-\omega_n+\omega_0)t]$ to write

$$W = \frac{1}{\hbar^2\omega}E_0^2\sum_n\int dt\frac{\langle 0|\,e^{i\mathcal{H}_0 t/\hbar}\tilde{J}_{\boldsymbol{q}}e^{-i\mathcal{H}_0 t/\hbar}\,|n\rangle\,\langle n|\,\tilde{J}^*_{\boldsymbol{q}}\,|0\rangle}{\omega_n-\omega_0}e^{i\omega t}. \tag{2.22}$$

Since $e^{i\mathcal{H}_0 t/\hbar}\tilde{J}_{\boldsymbol{q}}e^{-i\mathcal{H}_0 t/\hbar} = \tilde{J}_{\boldsymbol{q}}(t)$ in the interaction picture, we can rewrite the numerator as $\langle 0|\,\tilde{J}_{\boldsymbol{q}}(t)\,|n\rangle\,\langle n|\,\tilde{J}^*_{\boldsymbol{q}}\,|0\rangle$.

We can relate this transition rate to the optical conductivity by appealing to the relation $\mathcal{P} = \sigma_1(\omega)E_0^2 = \hbar\omega W/\mathcal{V}$, where $\mathcal{P}$ is the power absorbed by the sample per unit volume $\mathcal{V}$ [57]. Utilizing the dipole approximation $\boldsymbol{q}\approx 0$, we can immediately read off from Eq. (2.22),

$$\sigma_1(\omega) = \frac{1}{\hbar}\sum_n\int dt\frac{\langle 0|\,\tilde{J}_0(t)\,|n\rangle\,\langle n|\,\tilde{J}^*_0\,|0\rangle}{\omega_n-\omega_0}e^{i\omega t}, \tag{2.23}$$

which, remembering that $\omega = \omega_n - \omega_0$, can be written in the more familiar form

$$\sigma_1(\omega) = \frac{1}{\hbar\omega}\int dt|\,\langle 0|\,\tilde{J}_0(t)\tilde{J}^*_0\,|0\rangle\,|^2 e^{i\omega t}. \tag{2.24}$$

This is the Kubo formula, which is an example of the fluctuation-dissipation theorem relating current fluctuations to dissipation by absorption of optical radiation. The Drude form is recovered when one assumes that correlations in current fluctuations decay exponentially in time, *i.e.*, $\tilde{J}_0(t) = \tilde{J}_0(0)\exp(-\Gamma|t|)$ [55]. This assumption is just the relaxation time

approximation, which was used above in the calculation of the conductivity within the Boltzmann formalism. Inserting this into Eq. (2.23)

$$\sigma_1(\omega) = \frac{1}{\hbar}\sum_n \frac{|\langle n|\tilde{J}_0|0\rangle|^2}{\omega_n - \omega_0}\int dt e^{i\omega t - \Gamma|t|} = \frac{\Gamma}{\Gamma^2+\omega^2}\sum_n \frac{2}{\hbar}\frac{|\langle n|\tilde{J}_0|0\rangle|^2}{\omega_n-\omega_0}, \tag{2.25}$$

which we already recognize has Lorentzian frequency dependence of the real part of the Drude conductivity.

It can be shown [55, 57] that the sum in Eq. (2.25) is equal to $ne^2m^*/2$ for quasiparticles with parabolic dispersion. For $\boldsymbol{q} = 0$, $\tilde{J} = \int d\boldsymbol{r} J(\boldsymbol{r}) = -(e/m^*)\sum_i p_i$. Using this equality, Eq. (2.25) becomes

$$\sigma_1(\omega) = \frac{e^2}{m^*}\frac{\Gamma}{\Gamma^2+\omega^2}\sum_n \frac{2}{m^*}\frac{|\langle n|\sum_i p_i|0\rangle|^2}{\hbar(\omega_n-\omega_0)}. \tag{2.26}$$

In single particle quantum mechanics, the summand $2|\langle n|p|0\rangle|^2/[m^*\hbar(\omega_n-\omega_0)]$ is known as the oscillator strength $f_{n,0}$ and obeys the sum rule $\sum_n f_{n,0} = 1$ [63]. For quasiparticles in a solid, the sum in Eq. (2.26) is equal to the density, and we recover the Drude form of Eq. (2.13) [55, 57].

2.2.2 Interband absorption in graphene

Interband conductivity in graphene can also be calculated using Fermi's Golden Rule for the transition rate at finite temperature (accounting for both absorption and emission processes) [55, 57],

$$W_{v\to c} = \frac{2\pi}{\hbar}\sum_{i,f}|\langle f|V|i\rangle|^2\,\delta(\hbar\omega - \varepsilon_f + \varepsilon_i)\left[f(\varepsilon_i) - f(\varepsilon_f)\right], \tag{2.27}$$

where V is the part of the Hamiltonian that describes the interaction with the electromagnetic field and $f(\varepsilon) = (1+\exp[(\varepsilon-\mu)/k_{\mathrm{B}}T])^{-1}$ is the Fermi-Dirac distribution function. Here $|i\rangle$ and $|f\rangle$ are electron states in the valence and conduction band, respectively. Eq. (2.27) can be evaluated within the massless Dirac approximation of Eq. (2.7) by making the

substitution $\boldsymbol{p} = \hbar\boldsymbol{k} \to \boldsymbol{p} - (e/c)\mathbf{A}$, where $\mathbf{A}$ is the vector potential of the electromagnetic wave. The Hamiltonian is then $\mathcal{H} = \mathcal{H}_0 + V = v_\mathrm{F}(\boldsymbol{p} - (e/c)\mathbf{A}) \cdot \boldsymbol{\sigma}$. Within the dipole approximation for a linearly polarized light wave, where $\mathbf{A} = (cE_0/\omega)e^{-i\omega t}\hat{x}$,

$$V = \frac{ev_\mathrm{F}}{\omega} \begin{pmatrix} 0 & 1 \\ 1 & 0 \end{pmatrix} E_0. \tag{2.28}$$

Using this and Eq. (2.8) for the wavefunction, we find $|\langle f|V|i\rangle|^2 = (e^2 v_\mathrm{F}^2 E_0^2/\omega^2)\sin^2(\theta_{\boldsymbol{k}_i})\delta_{\boldsymbol{k}_f,\boldsymbol{k}_i}$. When we insert this into Eq. (2.27), the $\delta_{\boldsymbol{k}_f,\boldsymbol{k}_i}$ kills the sum over final states. We convert the sum over initial states to an integral over momentum $\sum_{\boldsymbol{k}_i} \to \mathcal{A}\int d^2k/(2\pi)^2$ (with $\mathcal{A}$ the area of the sample) and integrate to obtain

$$W_{v\to c} = \frac{e^2 E_0^2 \mathcal{A}}{16\hbar^2\omega}\left[f\left(-\frac{\hbar\omega}{2}\right) - f\left(\frac{\hbar\omega}{2}\right)\right]. \tag{2.29}$$

To obtain the optical conductivity from this expression, we again use the relation for power absorbed per unit area [57], $\mathcal{P} = \sigma_1(\omega)E_0^2 = \hbar\omega W_{v\to c}/\mathcal{A}$, and multiply by 4 to account for the spin and valley degeneracy, so that the final result is

$$\sigma_1(\omega) = \frac{\pi e^2}{2h}\left[f\left(-\frac{\hbar\omega}{2}\right) - f\left(\frac{\hbar\omega}{2}\right)\right]. \tag{2.30}$$

For undoped graphene at zero temperature, this reduces to the frequency-independent "universal" ac conductivity of graphene [64–66], $\sigma_1(\omega) = \sigma_0 = \pi e^2/2h$. At finite carrier density and zero temperature, Eq. (2.30) becomes $\sigma_1(\omega) = \sigma_0\theta(\hbar\omega - 2\varepsilon_\mathrm{F})$, where $\theta(x)$ is the step function. This describes the phenomenon of Pauli blocking, in which transitions for photon energies below $\hbar\omega = 2\varepsilon_\mathrm{F}$ are prohibited either due to the absence of electrons in the valence band (hole doped regime) or the presence of electrons in the conduction band (electron doped regime) [65, 67, 68]. A plot of the conductivity described by Eq. (2.30) at various temperatures and with Fermi energy set to 125 meV is shown in Fig. 2.6. Note that the temperature dependence of the chemical potential was included, so that the absorption onset at $\hbar\omega = 2|\mu|$ decreases with increasing temperature.

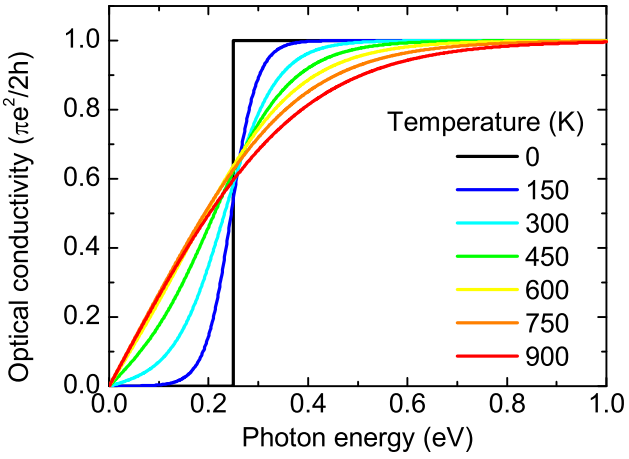

Figure 2.6: Interband conductivity of massless Dirac fermions at various temperatures with the Fermi energy set to $\varepsilon_F = 125$ meV, plotted using Eq. (2.30).

2.2.3 Sum rules and conservation of spectral weight

In §2.2.1, we encountered the f-sum rule when deriving the Drude conductivity from the Kubo formula. There exist several other sum rules which relate the optical constants of a material (permittivity, conductivity, etc.) to the number of particles in the system [56]. The f-sum rule for solids requires that

$$\int_0^\infty \sigma_1(\omega) d\omega = \frac{\pi n e^2}{2m_e}, \tag{2.31}$$

where $\sigma_1(\omega)$ is the real (dissipative) part of the optical conductivity, n is the total density of electrons in the material (including all valence and ion core electrons), and m_e is the free electron mass. This relation is required by causality and can be derived from the Kramers-Kronig relations [69, 70]. The quantity on the right hand side, $\pi n e^2/2m_e$, is known as the spectral weight SW, and the sum rule implies that the spectral weight is constant for a given material, regardless of any changes in temperature, pressure, or other external parameters.

Eq. 2.31 is not very useful in practice because it requires knowledge of $\sigma_1(\omega)$ for all ω, but it entails other, more useful relations. Specifically, one can define partial

sum rules relating to different dissipation mechanisms, such as a sum rule associated with intraband Drude absorption [56]. Measuring changes in spectral weight can be useful for understanding physical processes in solids. The spectral weight due to Drude absorption can be easily calculated by direct integration:

$$(\mathrm{SW})_{\mathrm{intra}} = \int_0^\infty \sigma_{\mathrm{intra},1}(\omega)d\omega = \int_0^\infty \frac{\Gamma D}{\pi(\Gamma^2+\omega^2)}d\omega = \frac{D}{2}. \tag{2.32}$$

For graphene at zero temperature, $(\mathrm{SW})_{\mathrm{intra}} = (e^2/\hbar^2)\varepsilon_{\mathrm{F}}/2$. Note that it is independent of the scattering rate, regardless of the form of D.

It is not as straightforward to calculate the spectral weight due to the interband absorption $(\mathrm{SW})_{\mathrm{inter}}$ in graphene within the Dirac approximation because the universal conductivity is constant and extends to infinite frequency. In practice, a cutoff frequency ω_{co} around which the Dirac approximation fails must be introduced. Then the spectral weight due to universal conductivity (at $T = 0$) is given by

$$(\mathrm{SW})_{\mathrm{inter}} = \int_0^{\omega_{\mathrm{co}}} \sigma_{\mathrm{inter}}(\omega)d\omega = \int_0^{\omega_{\mathrm{co}}} \frac{\pi e^2}{2h}\theta(\hbar\omega - 2\varepsilon_{\mathrm{F}})d\omega = \frac{e^2}{4\hbar^2}(\hbar\omega_{\mathrm{co}} - 2\varepsilon_{\mathrm{F}}). \tag{2.33}$$

When the graphene is intrinsic ($\varepsilon_{\mathrm{F}} = 0$), then the spectral weight is just the universal conductivity times the cutoff frequency. The difference in spectral weight between the intrinsic case and the finite-density case is $(\Delta\mathrm{SW})_{\mathrm{inter}} = -(e^2/\hbar^2)\varepsilon_{\mathrm{F}}/2$, which precisely cancels the increase in intraband spectral weight [Eq. (2.32)]. Spectral weight is conserved: $\mathrm{SW} = (\mathrm{SW})_{\mathrm{intra}} + (\mathrm{SW})_{\mathrm{inter}} = (e^2/4\hbar^2)\hbar\omega_{\mathrm{co}}$. Any changes in interband spectral weight must be accompanied by changes in intraband spectral weight. While Eqs. (2.32) and (2.33) were presented for $T = 0$, the spectral weight is conserved even at finite temperature, provided (ε_{F}, $k_{\mathrm{B}}T$) are smaller than $\hbar\omega_{\mathrm{co}}$ [65, 71]. Indeed, changing T or changing ε_{F} with an external gate results in transfer of spectral weight between $(\mathrm{SW})_{\mathrm{intra}}$ and $(\mathrm{SW})_{\mathrm{inter}}$. Electric field control of spectral weight transfer has been experimentally observed in infrared spectroscopic measurements of backgated graphene devices [11, 12]. Temperature-dependence

of the spectral weight distribution has been observed in graphite [72]. In both cases, while the distribution of spectral weight between $(\mathrm{SW})_{\mathrm{intra}}$ and $(\mathrm{SW})_{\mathrm{inter}}$ changed due to external perturbations, the total spectral weight was conserved. Consequences of spectral weight conservation on the photoconductive response of graphene will be discussed later in chapter 6.

Chapter 3

Coherent terahertz spectroscopy

There exist numerous techniques to probe the optical conductivity of solids over a wide range of photon energies ranging from μeV to eV [55,57]. As discussed in chapter 2, the relevant energy scales for free-carrier electrodynamics in graphene lie in the terahertz (THz) range. Historically, the THz range of the electromagnetic spectrum, usually considered as 0.1 – 10 THz, has been difficult to access experimentally [26,27]. In this chapter, we discuss time-domain terahertz spectroscopy, an optical technique based on ultrafast lasers that is able to access the THz gap. It has the additional advantage that it can be incorporated into pump-probe measurements to investigate the properties of a system after photoexcitation with ultrafast time resolution [25,28].

3.1 Time-domain terahertz spectroscopy

Time-domain terahertz spectroscopy (TDTS) is a powerful technique that allows access to the electrodynamic response of solids at energy scales relevant for many physical processes [26,27]. In contrast to conventional optical spectroscopies such as Fourier transform infrared spectroscopy, in which optical intensities are measured in the frequency domain, TDTS utilizes coherent generation and detection of THz radiation in the time domain. This leads to

distinct advantages over frequency-domain spectroscopies in the form of enhanced dynamic range and phase sensitivity [26]. Specifically, as discussed below, the phase sensitivity allows direct extraction of complex material optical constants in the measured frequency range. This contrasts with other spectroscopies which require Kramers-Kronig analysis of optical spectra measured over broad frequency ranges and are susceptible to errors induced by incorrect high- and low-frequency extrapolations [70].

3.1.1 THz generation and detection – nonlinear optics

For the measurements presented in this dissertation, we utilized nonlinear optics to generate and detect THz radiation. Pulses were generated by frequency conversion of an ultrashort ($\sim$100 fs) near infrared optical pulse using a second-order nonlinear effect called optical rectification. Detection occured by the inverse process, known as the Pockels effect, using free-space electro-optic sampling.

Optical rectification

A simplified description of optical rectification is useful to develop intuition for the THz generation process. In optics, the polarization P of a dielectric medium is often written as a power series in the electric field: $P(E) = \epsilon_0(\chi^{(1)}E + \chi^{(2)}E^2 + \chi^{(3)}E^3 + \cdots)$. In basic electromagnetic theory, one typically only considers the first-order contribution [69, 73]. When strong electric fields are present, however, higher-order terms can become important [74]. Optical rectification is a second-order nonlinear optical effect in which an electromagnetic wave at frequency ω induces a polarization in a nonlinear material that depends on the first two powers of $E(t)$, *e.g.*, $P(t) = \epsilon_0\left[\chi^{(1)}E_0\cos(\omega t) + \chi^{(2)}E_0^2\cos^2(\omega t)\right]$ for a monochromatic wave $E(t) = E_0\cos(\omega t)$. The part of the polarization that depends on the second power of the incident electromagnetic wave can be rewritten using a trigonometric identity

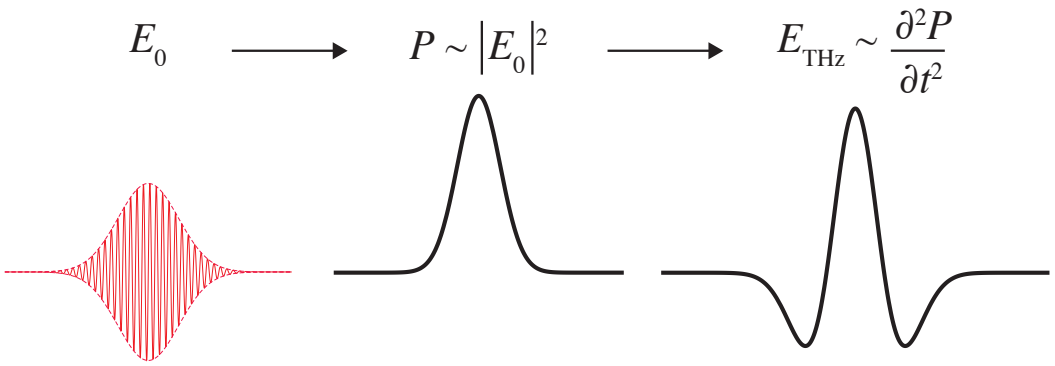

Figure 3.1: Illustration of THz generation by optical rectification. As an optical pulse propagating along the z-axis with electric field $E_0 \propto \exp[i\omega(t - z/c)] \exp[-(t - z/c)^2/2\tau^2]$ and passes through a nonlinear medium, it generates a nonlinear polarization $P(t) \propto |E_0(t)|^2$ which also passes through the medium. At each point in the medium, this time-dependent polarization radiates according to Maxwell's equations. The radiated field $E_{\mathrm{THz}} \propto (\partial^2 P/\partial t^2)$.

as $P_{\mathrm{NL}}(t) = \epsilon_0 \chi^{(2)} E_0^2 [1 + (1/2)\cos(2\omega t)]$. The first term in this expression represents a dc polarization P_{OR} induced by an oscillating electric field and is termed optical rectification. The second term represents second harmonic generation, and will not be considered further.

Terahertz generation through optical rectification occurs when a nonlinear material is illuminated by a strong optical light pulse (the generation pulse) [27]. The process can be described by a wave equation with a source,

$$\frac{\partial^2 E_{\mathrm{THz}}}{\partial z^2} - \frac{n^2}{c^2}\frac{\partial^2 E_{\mathrm{THz}}}{\partial t^2} = \frac{1}{\epsilon_0 c^2}\frac{\partial^2 P_{\mathrm{OR}}}{\partial t^2}, \tag{3.1}$$

where z is the propagation direction and n is the linear refractive index at THz frequencies [27, 74]. In linear optics, the term on the right-hand side is usually an external current, but here it is due to the nonlinear interaction of the generation pulse with the material, with $P_{\mathrm{OR}} = \epsilon_0 \chi^{(2)} |E_0|^2$, where $E_0(t) \propto \exp(-t^2/2\tau^2)\exp(-i\omega t)$ is the electric field of the generation pulse. The "dc" polarization $P_{\mathrm{OR}} \propto \exp(-t^2/\tau^2)$ then acts as a time-dependent dipole, which basic electrodynamics dictates will result in a radiated electromagnetic field

[69, 73],

$$E_{\mathrm{THz}}(t) \propto \frac{\partial^2}{\partial t^2} \exp(-t^2/\tau^2) = \frac{4}{\tau^4} \left(t^2 - \tau^2/2\right) \exp(-t^2/\tau^2). \tag{3.2}$$

This process is depicted in Fig. 3.1. To see that the frequency of the radiated field indeed lies in the terahertz range, we can compute the Fourier transform,

$$E_{\mathrm{THz}}(\omega) \propto (\omega^2 \tau) e^{-\omega^2 \tau^2/4}. \tag{3.3}$$

For a typical generation pulse duration $\tau \sim 100$ fs, this function contains frequencies from 0–8 THz and peaks at $\omega/2\pi \approx 3$ THz.

It is important to emphasize that this is an overly simplified description of optical rectification in real materials [27, 74]. A more sophisticated analysis would take into account effects of propagation of both the generation pulse $E_0(t)$ and the THz pulse $E_{\mathrm{THz}}(t)$ through the nonlinear medium, frequency-dependent material susceptibilities, and other complications [27, 74]. These effects limit the useable frequency range of $E_{\mathrm{THz}}(\omega)$ to around 0.2–3 THz. Additionally, the amplitude and polarization of the generated THz electric field depend strongly on the orientation of the crystal axes of the nonlinear medium relative to the polarization and wavevector of the generation pulse electric field $\mathbf{E}_0$. For example, zinc telluride (ZnTe) is a zincblende crystal with a large second-order nonlinear susceptibility that is often used for optical rectification [27]. In this material, THz emission is maximum when the generation pulse propagates along the [110] axis with $\mathbf{E}_0$ at an angle of $\theta = \sin^{-1}(\sqrt{2/3}) \approx 54.7°$ from the [001] axis (towards the [$\bar{1}$10] axis) [27]. When this is the case, $\mathbf{E}_{\mathrm{THz}} \parallel \mathbf{E}_0$ and the THz pulse propagates collinearly with the generation pulse.

Free-space electro-optic sampling

Coherent terahertz pulses are detected using a technique known as free-space electro-optic sampling [27]. This method relies on the Pockels effect (or linear electro-optic effect), another

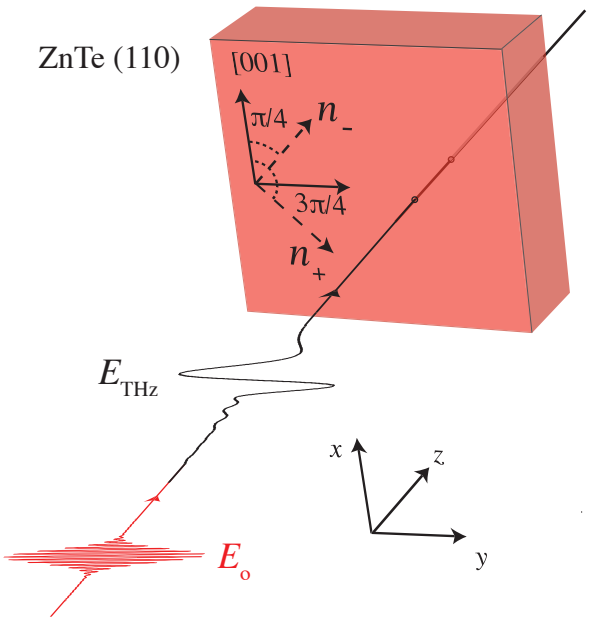

Figure 3.2: Schematic of electro-optic sampling. A THz pulse and optical pulse co-propagate through a ZnTe crystal. The presence of the THz field induces birefringence in the crystal which changes the polarization of the optical pulse. Note that the pulse durations are not to scale in this figure.

second-order nonlinear optical effect that results from the same nonlinear susceptibility as optical rectification [27, 74]. In contrast to optical rectification, no simple intuitive description of the Pockels effect in terms of basic electromagnetism exists. Phenomenologically, the effect can be described as electric field-induced birefringence. Initially, the refractive index for propagation of an optical pulse $\mathbf{E}_{\mathrm{o}}$ through a nonlinear crystal does not depend on the orientation of the light polarization relative to the crystal axes. Through a second-order interaction with the crystal, the presence of $\mathbf{E}_{\mathrm{THz}}$ changes the optical refractive index for different polarizations as the pulse propagates along certain crystal axes.

The induced birefringence depends sensitively on the relative polarizations of the THz and optical light fields, as well as their alignment relative to crystal axes of the electro-optic (EO) material. The general case is quite complicated, and the reader is referred to

Refs. [74, 75] for a rigorous discussion. Here, we consider the specific relevant case of a linearly-polarized optical pulse propagating perpendicular to the (110) face of ZnTe, with the [001] crystal axis parallel to the $\hat{x}$ axis in the laboratory frame (Fig. 3.2). The EO sampling signal is maximized when $\mathbf{E}_{\mathrm{THz}} \perp \hat{x}$ (*i.e.*, $\mathbf{E}_{\mathrm{THz}} \perp [001]$) [75]. Then the refractive index for $\mathbf{E}_{\mathrm{o}}$ parallel to $(\hat{x} + \hat{y})$ becomes $n_- \approx n_{\mathrm{o}} - (1/2)n_{\mathrm{o}}^3 r_{41} E_{\mathrm{THz}}$, while the refractive index for $\mathbf{E}_{\mathrm{o}}$ parallel to $(\hat{x} - \hat{y})$ becomes $n_+ \approx n_{\mathrm{o}} + (1/2)n_{\mathrm{o}}^3 r_{41} E_{\mathrm{THz}}$ [27, 74, 75]. Here n_{o} is the refractive index of the ZnTe at the optical pulse frequency and r_{41} is the EO coefficient for the ZnTe crystal.

When $\mathbf{E}_{\mathrm{THz}} \perp \hat{x}$, the EO sampling signal can be maximized by setting $\mathbf{E}_{\mathrm{o}} \parallel \mathbf{E}_{\mathrm{THz}}$ or $\mathbf{E}_{\mathrm{o}} \perp \mathbf{E}_{\mathrm{THz}}$ [75]. We consider the former situation: $\mathbf{E}_{\mathrm{o}} = E_{\mathrm{o}}\hat{y}$. The ZnTe detection crystal is oriented such that the fast axis (*i.e.*, axis along which the optical pulse experiences index $n_- < n_{\mathrm{o}}$) is parallel to $(\hat{x} + \hat{y})$ and the slow axis is parallel to $(\hat{x} - \hat{y})$ (Fig. 3.2). It is most convenient to rotate the lab frame by $\pi/4$ into a frame in which the x' and y' axes are parallel to the fast and slow axes of the ZnTe, respectively. In this frame, the optical electric field is

$$\mathbf{E}'_{\mathrm{o}} = \frac{E_{\mathrm{o}}}{\sqrt{2}} \begin{pmatrix} 1 \\ 1 \end{pmatrix}. \tag{3.4}$$

The Jones matrix [76] for propagation through the crystal with different indices of refraction is

$$P = \begin{pmatrix} e^{in_-\omega L/c} & 0 \\ 0 & e^{in_+\omega L/c} \end{pmatrix} \tag{3.5}$$

where ω is the probe pulse frequency, L is the EO crystal thickness, and c is the speed of light in vacuum. The optical electric field after the ZnTe can be found by taking $\mathbf{E}'_{\mathrm{o}} \rightarrow P\mathbf{E}'_{\mathrm{o}}$:

$$\mathbf{E}'_{\mathrm{o}} = \frac{E_{\mathrm{o}}}{\sqrt{2}} \begin{pmatrix} e^{in_-\omega L/c} \\ e^{in_+\omega L/c} \end{pmatrix} = e^{in_-\omega L/c} \frac{E_{\mathrm{o}}}{\sqrt{2}} \begin{pmatrix} 1 \\ e^{i(2\delta n)\omega L/c} \end{pmatrix}, \tag{3.6}$$

where $\delta n = (1/2) n_{\rm o}^3 r_{41} E_{\rm THz}$. For convenience, we define $\varphi \equiv (2\delta n)\omega L/c$. From Eq. (3.6), we see that propagation through the EO crystal has introduced a phase shift φ between the x' and y' components of $\mathbf{E}'_{\rm o}$.

To measure this phase shift, the optical pulse is propagated through a quarter-wave ($\lambda/4$) plate and a polarizing beam splitter (Wollaston prism) before being sent to a pair of photodiodes. The $\lambda/4$ plate introduces an additional $\pi/2$ phase shift, so

$$\mathbf{E}'_{\rm o} = e^{in_- \omega L/c} \frac{E_{\rm o}}{\sqrt{2}} \begin{pmatrix} 1 \\ e^{i(\varphi+\pi/2)} \end{pmatrix}. \tag{3.7}$$

Rotating back to the original lab frame,

$$\mathbf{E}_{\rm o} = e^{in_- \omega L/c} \frac{E_{\rm o}}{2} \begin{pmatrix} 1 + e^{i(\varphi+\pi/2)} \\ 1 - e^{i(\varphi+\pi/2)} \end{pmatrix}. \tag{3.8}$$

Next, the Wollaston prism splits the beam so that the x-polarized component of $\mathbf{E}_{\rm o}$ is sent to one photodiode and the y-polarized component to a second photodiode. The intensity incident upon each photodiode is given by the magnitude of the Poynting vector, $\mathbf{S} = (1/2)\sqrt{\epsilon_0/\mu_0}\,(\mathbf{E}_{\rm o} \cdot \mathbf{E}_{\rm o}^*)\,\hat{z}$ [69]. From Eq. (3.8), we find

$$\mathbf{S}_{x(y)} = \frac{I_0}{2}\,(1 \pm \sin\varphi)\,\hat{z} \approx \frac{I_0}{2}\,(1 \pm \varphi)\,\hat{z}, \tag{3.9}$$

where $I_0 = (E_{\rm o}^2/2)\sqrt{\frac{\epsilon_0}{\mu_0}}$ [73]. The difference in intensities on the two photodiodes is then $\Delta I = |\mathbf{S}_x| - |\mathbf{S}_y| = I_0 \varphi$. From above, $\varphi = \frac{\omega L}{c} n_{\rm o}^3 r_{41} E_{\rm THz}$, so

$$\Delta I / I_0 = \frac{\omega L}{c} n_{\rm o}^3 r_{41} E_{\rm THz}. \tag{3.10}$$

Eq. (3.10) is accurate as long as $\left[(\omega L/c) n_{\rm o}^3 r_{41} E_{\rm THz}\right] \ll 1$, which is satisfied for most EO sampling measurements made for spectroscopic purposes. With $r_{41} = 3.9$ pm/V and $n_{\rm o} \approx 3$ at 800 nm [27, 75], $\Delta I/I_0 \approx 5\%$ for $E_{\rm THz} = 0.6$ kV/cm.

To measure the time dependence of $E_{\rm THz}(t)$ using free space EO sampling, one first splits an optical pulse from an ultrafast laser into two paths (Fig. 3.3). One part

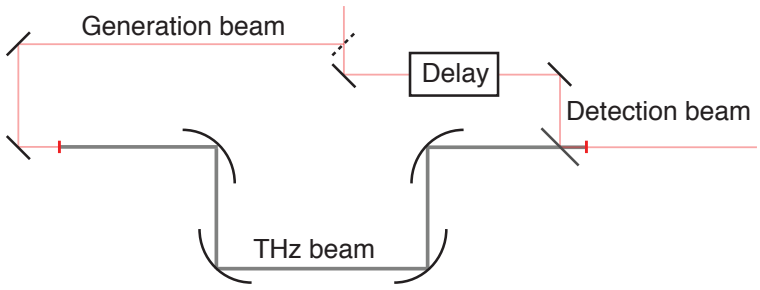

Figure 3.3: Schematic of THz setup. The beam from the laser is split into a generation beam and a detection beam. The THz pulse and detection pulse co-propagate through a ZnTe EO crystal. By varying the time overlap of the THz and detection pulses, the time dependence of E_{THz} is measured.

of the pulse is used to generate a THz pulse by optical rectification in a ZnTe crystal (as described in the previous subsection). The second part of the pulse is combined with the generated THz pulse using a thin-film beam splitter, after which they co-propagate through a second ZnTe crystal. Since the optical pulse is much shorter than the THz pulse, it only experiences the field strength $E_{\mathrm{THz}}(t)$ at the time at which they are overlapped. To map out the full t-dependence, one simply changes the relative path lengths using a mechanical delay ("Delay" in Fig. 3.3). In the example data of Fig. 3.5, negative times correspond to the situation in which the optical probe pulse reaches the ZnTe crystal before the THz pulse, *i.e.*, the detection pulse path is shorter than the generation pulse path + THz pulse path. As a result, no EO signal is measured. One then uses the mechanical delay to increase the detection pulse path length so that the pulse arrives at the ZnTe at the same time as the leading edge of the THz pulse. Increasing the detection path further changes the measured EO signal by an amount proportional to the strength of $E_{\mathrm{THz}}(t)$ at the time of overlap and eventually results in the THz pulse propagating through the detection crystal before the detection pulse arrives.

3.1.2 Measuring optical constants using time-domain spectroscopy

In time-domain spectroscopy, one measures the electric field waveform $E(t)$ of a coherent light pulse. The recorded signal contains both amplitude and phase information. By Fourier transforming the time-domain data, the amplitude $|E(\omega)|$ and phase $\phi_E(\omega)$ of the electric field as a function of frequency are obtained. TDTS is most often performed in a transmission geometry (Fig. 3.4). In order to use this technique to extract the optical properties of a material, the measured light transmitted through the sample needs to be compared to the light incident on the sample. To accomplish this, one measures both a pulse transmitted through the sample of interest, as well as a pulse transmitted through a known reference. For optically thick samples, an empty aperture or vacuum is often used as the reference. For a thin film sample on a substrate, the reference is often a bare substrate identical to the one on which the sample is deposited.

To extract the material properties from the measured waveforms, one uses the Fresnel equations (not the Frenzel equations!), which describe the transmission and reflection of electromagnetic waves from interfaces [69, 73]. The Jones matrix formalism is useful for analyzing the effects of multiple interfaces on an incident electromagnetic wave [76]. In this formalism, the electric field of the light wave is represented by a two-component vector, $\mathbf{E} = (E_x, E_y)$. A 2×2 matrix M is assigned to each optical element or interface encountered by the wave as it propagates through an optical system. The electric field after propagating through the optical system, $\mathbf{E}_f$, is found by sequentially multiplying the initial electric field $\mathbf{E}_i$ by the matrix representing each optical element: $\mathbf{E}_f = M_N \cdot M_{N-1} \cdots M_2 \cdot M_1 \cdot \mathbf{E}_i$. In the case relevant for TDTS without any polarization-altering optics, we can choose the electric field to be polarized along, say, the $\hat{x}$ axis so that we only consider the x component of $\mathbf{E}$, and the matrices all become constants. This allows us to extract the material properties of a given sample if the incident electric field is known, as outlined below. Note that this

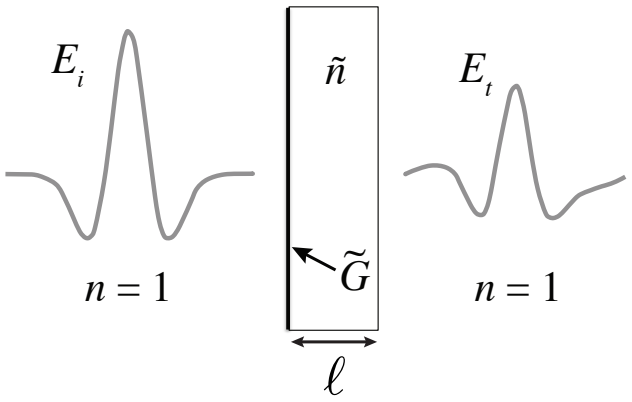

Figure 3.4: Geometry for TDTS measurements. Interaction of the incident pulse E_i with the material results in an attenuated and distorted transmitted pulse E_t, which can be either the sample pulse $E_{\rm sam}$ or reference pulse $E_{\rm ref}$ (see text for details). Reflected pulse E_r is not shown.

analysis must be performed in the frequency domain for polychromatic waves.

For a thin film sample and bare substrate reference (Fig. 3.4), the analysis proceeds as follows. The frequency-domain electric fields transmitted through the sample and reference are given by $\tilde{E}_{\rm sam} = t_{01}^{G} P(\tilde{n}_s, \ell_{\rm sam}) t_{10} \tilde{E}_i$ and $\tilde{E}_{\rm ref} = t_{01}^{0} P(\tilde{n}_s, \ell_{\rm ref}) t_{10} \tilde{E}_i$, respectively. Here $\tilde{E}_i$ is the incident field and $P(\tilde{n}_s, \ell_{\rm sam(ref)}) = \exp(i\tilde{n}_s \omega \ell_{\rm sam(ref)}/c)$ is the coefficient for propagation through the sample (reference) substrate with complex refractive index $\tilde{n}_s = n_s + ik_s$ and thickness $\ell_{\rm sam(ref)}$, and

$$\begin{aligned} t_{01}^{G} &= \frac{2}{1 + \tilde{n}_s + \tilde{G} Z_0}; \\ t_{10} &= \frac{2\tilde{n}_s}{1 + \tilde{n}_s} \end{aligned} \tag{3.11}$$

are the transmission coefficients for the front face and back face of the sample or reference. Here $\tilde{G} = G_1 + iG_2$ is the complex conductance of the thin film sample and $Z_0 = 376.6\ \Omega = 2\alpha(h/e^2)$ is the impedance of free space (with $\alpha = 1/137$ the fine structure constant). Taking the ratio $\tilde{E}_{\rm sam}/\tilde{E}_{\rm ref}$ yields

$$\tilde{t} \equiv \frac{\tilde{E}_{\rm sam}}{\tilde{E}_{\rm ref}} = \frac{t_{01}^{G} P(\ell_{\rm sam})}{t_{01}^{0} P(\ell_{\rm ref})} = \frac{e^{i\tilde{n}_s \omega \Delta\ell/c}}{1 + \frac{Z_0 \tilde{G}}{\tilde{n}_s + 1}}, \tag{3.12}$$

where $\Delta\ell = \ell_{\text{sam}} - \ell_{\text{ref}}$ is the difference in thickness between the sample and reference substrates. This expression can be directly inverted to obtain the complex sheet conductance of the sample:

$$\tilde{G} = \frac{\tilde{n}_s + 1}{Z_0}\left(\frac{e^{i\tilde{n}_s\omega\Delta\ell/c}}{\tilde{t}} - 1\right). \tag{3.13}$$

For samples of different dimension D, the sheet conductance is related to the conductivity $\tilde{\sigma}$ by the relation $\tilde{G} = \tilde{\sigma}d^{D-2}$, where d is the thickness of the thin film sample. Graphene can be considered to be two-dimensional, in which case the conductance and conductivity are equal: $\tilde{G} = \tilde{\sigma}$. We will therefore use "conductance" and "conductivity" interchangeably.

In order to reliably extract the conductivity of a thin film sample using the above procedure, the complex refractive index of the substrate must be known. To obtain this information, one measures the electric field pulse transmitted through a bare substrate, $\tilde{E}_{\text{subs}} = t_{01}^0 P(\tilde{n}_s, \ell_{\text{subs}}) t_{10}\tilde{E}_i$, and a pulse transmitted through a vacuum reference, $\tilde{E}_{\text{ref}} = P(1, \ell_{\text{subs}})\tilde{E}_i$, where $P(1, \ell_{\text{subs}}) = \exp(i\omega\ell_{\text{subs}}/c)$ describes propagation of the electromagnetic wave through a slab of vacuum with the same thickness as the substrate. Taking the ratio $\tilde{E}_{\text{subs}}/\tilde{E}_{\text{ref}}$, we find for the transmission coefficient:

$$\tilde{t} = \frac{4\tilde{n}_s}{(1+\tilde{n}_s)^2} e^{i(\tilde{n}_s - 1)\omega\ell_{\text{subs}}/c}. \tag{3.14}$$

This is a transcendental equation for $\tilde{n}_s$ that cannot be solved analytically. Several approaches exist to numerically solve for $\tilde{n}_s$, but for the measurements presented in this dissertation we chose to use the method developed by Duvillaret *et al.* (Ref. [77]). This approach is robust and straightforward to implement. It has the added advantage that it can be extended to extract the substrate thickness ℓ_{subs} in addition to the optical constants [78], which helps to remove systematic error associated with $\Delta\ell$ [Eq. (3.13)].

An example of typical TDTS data is shown in Fig. 3.5. The top panels show the time- and frequency-domain signals measured after transmission through a 1 mm-thick

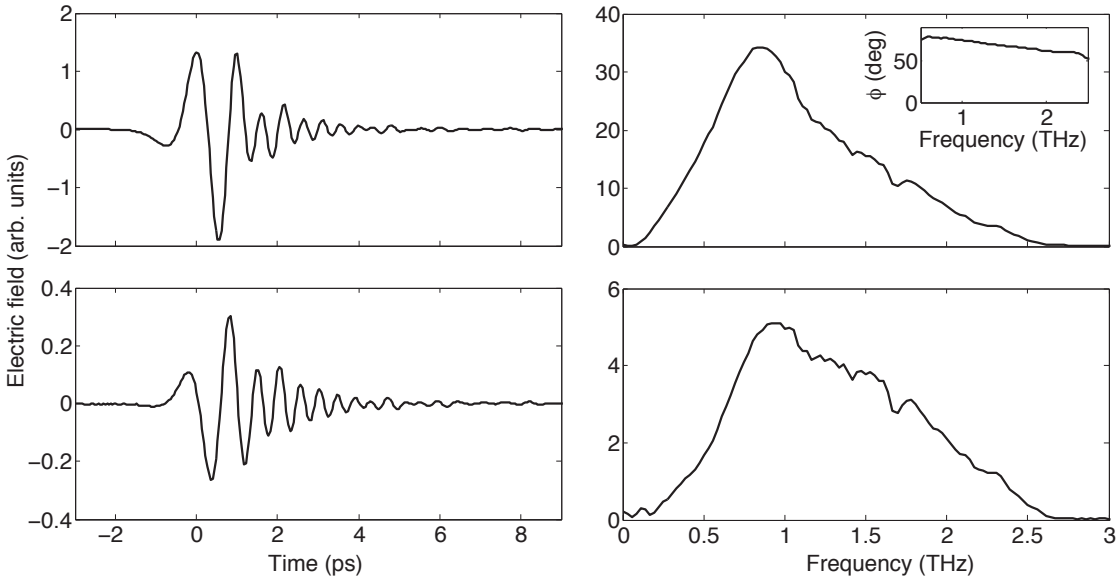

Figure 3.5: Example of TDTS data. Top panels display the electric field of the pulse transmitted through a reference, in this case a bare $LaSrAlO_4$ substrate. Bottom panels display the pulse transmitted through the sample, a thin film of the cuprate superconductor $La_{2-x}Sr_xCuO_4$ ($x = 0.16$) on a $LaSrAlO_4$ substrate.

$LaSrAlO_4$ substrate. Only the absolute value of frequency-domain signal is presented in the right panel, *i.e.*, it does not include the phase. The bottom panels show the time- and frequency-domain electric fields transmitted through a 52 nm thin film of the cuprate superconductor $La_{2-x}Sr_xCuO_4$ ($x = 0.16$) on a 1 mm $LaSrAlO_4$ substrate at $T = 4$ K. Compared to the top panels, it is apparent that the pulse transmitted through the superconducting sample is strongly reduced in amplitude and phase shifted. Indeed, the phase shift, shown in the inset of the top-right panel, is in the range $\pi/4 < \phi < \pi/2$ for all measured frequencies. From the measured attenuation and phase shift, the optical conductivity can be extracted using Eq. (3.13). The large phase shift reflects the large imaginary conductivity characteristic of superconductors. Further discussion of the static and time-resolved terahertz properties of $La_{2-x}Sr_xCuO_4$ is presented in the appendix.

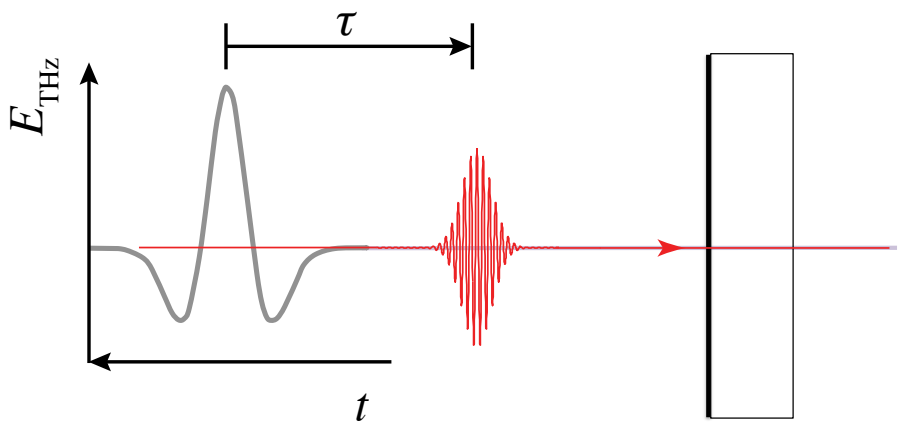

Figure 3.6: Schematic of time-resolved optical pump-terahertz probe spectroscopy experiment. The "local" probe pulse time is denoted by t, while the pump-probe delay is denoted by τ.

3.2 Time-resolved optical pump-terahertz probe spectroscopy

The terahertz spectroscopic measurements described in §3.1.2, enabled by the nonlinear optical techniques discussed in §3.1.1, have proven extremely useful for characterizing materials in equilibrium conditions. Time-resolved optical pump-terahertz probe spectroscopy (or time-resolved terahertz spectroscopy, TRTS) extends the utility of TDTS by allowing characterization of low-energy electrodynamics in samples out of equilibrium [24, 28, 56]. In this technique, a sample is first photoexcited by a strong optical pulse. Then at some time delay τ after photoexcitation, which can be adjusted, the electrodynamic response is probed by a THz pulse. There are two characteristic time scales involved in these experiments (Fig. 3.6). First is the time t at which the THz pulse is sampled, the "local" time. Second is the time delay between optical pump and THz probe pulses, denoted as τ. Measuring the THz properties of the sample under study as a function of pump-probe delay yields information about the nonequilibrium state induced by photoexcitation and the dynamical return to the equilibrium state. Different information can be obtained by varying one of the time scales,

t or τ, with the other held fixed. In certain cases, one must obtain a full array of data as a function of both t and τ in order to properly interpret the results [79]. The different cases are discussed in the following sections.

3.2.1 1D probe scans

The 1D probe scan is a straightforward nonequilibrium extension of the static THz spectroscopy described in §3.1.2. In this experimental protocol, the pump-probe delay τ is held fixed at some value while t is varied to measure the THz waveform transmitted through the photoexcited sample [79]. This method is valuable for cases in which the nonequilibrium sample response changes slowly over the timescale of the THz pulse, and it cannot be reliably applied to very early time dynamics ($\lesssim 1$ ps) [80]. It can be used to extract nonequilibrium transport properties of a sample, such as time-dependent carrier densities $n(\tau)$ and scattering rates $\Gamma(\tau)$ in GaAs or Si semiconductors [24, 79, 81], or superfluid densities $\rho_s(\tau)$ in superconductors [28, 56, 82–84] (see also appendix A).

Typically one measures the photoinduced change to the field transmitted through the sample at given pump-probe delay τ, termed the "differential field" $\Delta E_\tau(t)$, rather than measuring the full field after photoexcitation. This allows the ability to detect smaller photoinduced changes to the sample's optical properties. The differential field can be related to the photoinduced change to the optical properties of the sample if a reference is collected by measuring the THz pulse transmitted through the sample in the absence of photoexcitation, the "equilibrium field" $E_0(t)$. For a thin film on a transparent ($\tilde{n}_s = n_s + 0i$) substrate, the differential conductivity $\Delta\tilde{\sigma}_\tau(\omega)$ can be related to the measured signal by [26, 85, 86]

$$\Delta\tilde{\sigma}_\tau(\omega) \approx -\frac{n_s + 1}{Z_0}\frac{\Delta\tilde{E}_\tau(\omega)}{\tilde{E}_0(\omega)} \tag{3.15}$$

where $\Delta\tilde{E}_\tau(\omega)$ and $\tilde{E}_0(\omega)$ are the complex Fourier transforms of $\Delta E_\tau(t)$ and $E_0(t)$, respectively. This relation can be derived from the Fresnel equations for the transmission

coefficient [Eqs. (3.11)] as follows. If we denote the equilibrium film conductivity $\tilde{\sigma}_0$ and the nonequilibrium conductivity at pump-probe delay τ by $\tilde{\sigma}_\tau$, then

$$\frac{\Delta\tilde{T}_\tau}{\tilde{T}_0} = \frac{-Z_0(\tilde{\sigma}_\tau - \tilde{\sigma}_0)}{1 + n_s + \tilde{\sigma}_\tau Z_0} \approx -\frac{Z_0 \Delta\tilde{\sigma}_\tau}{1 + n_s} \tag{3.16}$$

where $\Delta\tilde{T}_\tau = \tilde{T}_\tau - \tilde{T}_0$, $\tilde{T}_\tau = t_{01}^{\sigma_\tau}$ from Eqs. 3.11, and in the last step we have assumed that $\tilde{\sigma}_\tau Z_0/(n_s+1) \ll 1$. For graphene on quartz, with $\tilde{\sigma}_\tau \approx \sigma_{\tau,1} \sim 10e^2/h$ and $n_s = 2.1$ [87], the error introduced by this approximation is a few percent. Solving for $\Delta\tilde{\sigma}_\tau$, and multiplying $\Delta\tilde{T}_\tau$ and $\tilde{T}_0$ by $\tilde{E}_i(\omega)$ (where $\tilde{E}_i(\omega)$ is the THz field incident on the sample), one recovers Eq. (3.15).

The simplest method to collect a 1D probe scan data set is to fix the pump-probe delay τ and measure the THz probe pulse by adjusting the detection beam path length, as discussed above in §3.1.1. When this method is used, however, different time points of the THz probe pulse (*i.e.*, different values of t) experience different pump-probe delays. To see why this is the case, it is helpful to consider the experimental technique used to vary t and τ. Consider the case when the pump pulse path length is chosen such that the pump pulse arrives at the sample at the same time as the main peak of the THz pulse ($\tau = 0$ in Fig. 3.6). The leading edge of the THz pulse then arrived at the sample before the pump pulse arrived, and so transmitted through a sample still in equilibrium. The peak of the THz pulse propagates through the sample just as it interacts with the pump pulse, and therefore experiences the largest pump-induced modulation. Finally, the trailing edge of the THz pulse passes through the sample as the response has already begun to relax to equilibrium. By measuring $\Delta E_\tau(t)$ solely through changing the detection pulse path, one measures a THz pulse with this complicated history. If the sample response changes on timescales much longer than the THz pulse duration, then this is not an issue. For graphene, however, the characteristic relaxation timescale for photoconductivity is around 1–2 ps, so

the sample changes significantly as the pulse propagates through.

If one is interested in measuring the sample properties at a time delay τ after photoexcitation, then one must obtain a measurement of $\Delta E_\tau(t)$ in which all values of t experience the same pump-probe delay τ. There are multiple methods to accomplish this [79]. The simplest is to record the data as described above at all relevant t and τ, then numerically extract the desired data. Alternatively, one can simultaneously adjust the pump and detection beam path lengths to accomplish the same effect. To understand this, recall that earlier local times (smaller t) correspond to shorter detection path lengths. In contrast, earlier pump-probe delays (smaller τ) correspond to *later* arrival times of the pump pulse to the sample (THz pulse reaches the sample before the pump pulse) and therefore *longer* pump pulse path lengths. For concreteness, consider Fig. 3.6 with the scale of t set such that $t = 0$ corresponds to the peak of the THz pulse. To measure $\Delta E_\tau(t < 0)$, the pump pulse path length must be made shorter (increasing τ) so that the pump pulse arrives at the sample earlier relative to the THz peak. Similarly, for $\Delta E_\tau(t > 0)$, the pump pulse path must be made longer (decreasing τ). If the pump pulse path length is adjusted for each value of t in this way, then the measured $\Delta E_\tau(t)$ will have the same pump-probe delay for each t. Often, this is sufficient to allow one to analyze the data as described in §3.2.1 for 1D probe scans. This method was used for all 1D probe scans presented in this dissertation.

An example of 1D probe scan data is shown in Fig. 3.7. The left panel shows $E_0(t)$ (black solid curve) and $\Delta E_\tau(t)$ (red dashed curve) obtained a few picoseconds after photoexciting semi-insulating gallium arsenide with a 1.55 eV pump pulse. $\Delta E_\tau(t)$ is everywhere opposite in sign to $E_0(t)$, *i.e.*, $\Delta E_\tau/E_0$ is negative for all times t. From Eq. (3.15), we see that this corresponds to positive photoconductivity (*i.e.*, $\Delta\sigma_\tau > 0$). This is shown in the right panel, where we have plotted $\Delta\tilde{\sigma}_\tau(\omega)$ calculated directly from Eq. (3.15) (red dots), assuming that the photoexcited carriers are confined to a thin conducting film of

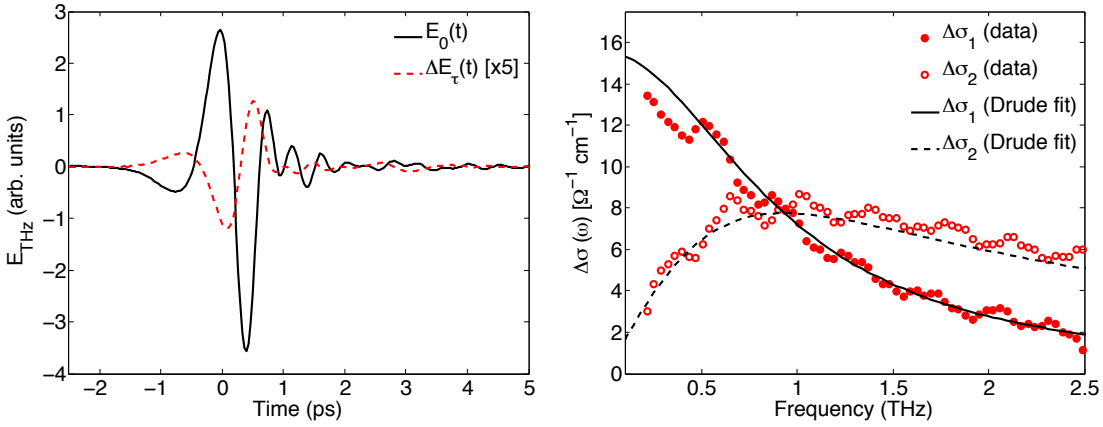

Figure 3.7: Transient conductivity of GaAs measured by 1D probe scans a few picoseconds after photoexcitation. The left panel shows the electric field $E_0(t)$ of the THz pulse transmitted through the sample in equilibrium (black line) and the photoinduced change $\Delta E_\tau(t)$. The right panel shows the complex differential conductivity extracted using Eq. (3.15) (red dots), setting the thickness of the conducting layer to $d = 0.9$ μm, the penetration depth at the pump photon energy [79]. A fit to the Drude model is also shown (black lines). The scattering rate $\Gamma/2\pi$ of the photoexcited carriers is almost exactly 1 THz.

thickness equal to the penetration depth at 1.55 eV. The experimental data can be fit by the Drude model to extract a photocarrier scattering rate $\Gamma/2\pi \sim 1$ THz. Further analysis of photoconductivity in GaAs is presented in Ref. [24] and references therein.

3.2.2 1D pump scans

If one is interested in the temporal dynamics of photoexcited carriers rather than their transport properties at a single time delay, one performs a 1D pump scan. In this experiment, the pump-probe delay τ is varied while the local THz time t is held fixed, usually at the peak of the waveform $t = t_{\text{peak}}$ [79]. This technique provides access to the time-dependence of the material properties after photoexcitation averaged over frequency. It is most useful when the differential conductivity is only weakly frequency dependent and mostly real, *i.e.*, $\Delta\tilde{\sigma}_\tau(\omega) \approx \Delta\sigma_{\tau,1} \approx$ const. In this case, photoexcitation primarily changes the amplitude of the THz field transmitted through the sample, and $\Delta\tilde{\sigma}_\tau$ can be directly related to $\Delta E_\tau/E_0$.

To justify this claim, we consider the Fourier representation of the electric field transmitted through the sample as a function of time,

$$E_0(t) = \int \frac{d\omega}{2\pi} T_0(\omega)\tilde{E}_i(\omega)e^{-i\omega t}, \tag{3.17}$$

where $\tilde{E}_i(\omega)$ is the Fourier transform of the incident THz pulse. After photoexcitation, this expression becomes

$$E_\tau(t) = \int \frac{d\omega}{2\pi} T_\tau(\omega)\tilde{E}_i(\omega)e^{-i\omega t}, \tag{3.18}$$

where τ is the time delay between pump and probe pulses. Then we have

$$\Delta E_\tau(0) = E_\tau(0) - E_0(0) = \int \frac{d\omega}{2\pi} \Delta T_\tau(\omega)\tilde{E}_i(\omega), \tag{3.19}$$

where $\Delta T_\tau(\omega) = T_\tau(\omega) - T_0(\omega)$ and we have set $t = t_{\text{peak}} = 0$. Therefore,

$$\frac{\Delta E_\tau}{E_0} = \frac{\int \frac{d\omega}{2\pi} \Delta T_\tau(\omega)\tilde{E}_i(\omega)}{\int \frac{d\omega}{2\pi} T_0(\omega)\tilde{E}_i(\omega)}. \tag{3.20}$$

For a real and weakly ω-dependent transmission coefficient before and after photoexcitation, ΔT and T_0 can be taken outside the integrals, which then cancel, leaving

$$\frac{\Delta E_\tau}{E_0} = \frac{\Delta T_\tau}{T_0} = -\frac{\Delta\sigma_{\tau,1} Z_0}{n_s + 1}. \tag{3.21}$$

Note that the condition that the transmission coefficients are approximately real and frequency-independent also requires the substrate to be transparent to THz light, $\tilde{n}_s \approx n_s + i0$.

One can see from Eq. (3.20) that the quantity $\Delta E_\tau/E_0$ is much more difficult to interpret when T_τ and T_0 depend on frequency. This is because the imaginary part of the transmission coefficient affects the phase of the transmitted pulse. If photoexcitation changes the material properties in a complex, frequency dependent way, there is no straightforward method to separate contributions to $\Delta E_\tau/E_0$ from changing the amplitude and changing the phase of the transmitted pulse. One must therefore exercise caution when interpreting $\Delta E_\tau/E_0$ in materials with high mobility [88].

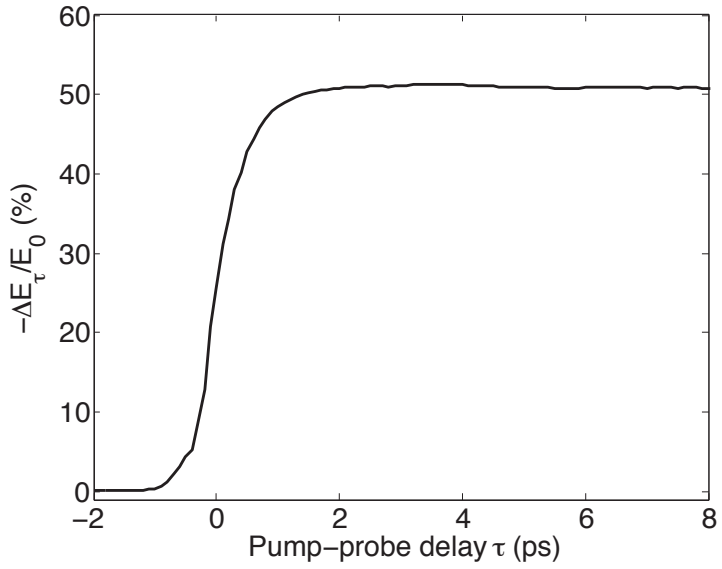

Figure 3.8: Transient conductivity of Si measured by 1D pump scan. Photoexcitation at $\tau = 0$ drastically increases the conductivity of the sample by introducing free photocarriers, reducing the amplitude of the transmitted signal by 50%.

A typical 1D pump scan is shown in Fig. 3.8. This figure shows the pump-induced change to the transmission through high-resistivity silicon of the THz peak as a function of pump-probe delay τ. For $\tau < 0$, the probe pulse transmitted through the sample before the arrival of the pump pulse, so the differential field is zero. Around $\tau = 0$, the conductivity increased sharply (recall, $\Delta\sigma \propto -\Delta E_\tau / E_0$). This is nearly identical to the behavior observed in GaAs (Fig. 3.7). The long-lived photoconductivity signal reflects the long lifetime of photocarriers in Si, which results from the indirect band gap in this material. Further discussion of the nonequilibrium THz properties of Si is presented in Ref. [89] and references therein.

3.2.3 2D time-resolved spectroscopy

Simply performing isolated 1D probe scans is insufficient when one is interested in very early time dynamics, and 1D pump scans can be subject to artifacts when the sample response

depends strongly on frequency [79, 80, 90]. In these cases, one must collect a 2D data set consisting of $\Delta E_\tau(t)$ as a function of both τ and t. This is because the finite bandwidth of the electro-optic detection system can distort the measured pulses and introduce artifacts to the extracted material properties. The detector response function must then be included in the data analysis either by deconvolving the measured signal [79, 80] or by simulation using finite-difference time-domain methods [91, 92].

Detector response

If one is interested in extracting rapidly-varying sample properties at pump-probe delays $<$1 ps after photoexcitation, the procedure described in §3.2.1 is not sufficient to remove experimental artifacts from the data [79]. This is because the EO detector response function has a finite bandwidth which limits the measurement's time resolution and can introduce frequency-domain artifacts to the data [27, 80, 93–95]. The detector response function takes into account imperfect phase matching between the THz pulse and detection pulse, frequency-dependence of the nonlinear susceptibility, THz absorption, and finite detection pulse duration. Of these, imperfect phase matching (*i.e.*, different phase velocities for $\mathbf{E}_\mathrm{o}$ and $\mathbf{E}_\mathrm{THz}$) has the largest limiting effect on the bandwidth [94]. It is important to note that the detector response depends strongly on the EO crystal thickness, with thinner crystals causing less pulse distortion than thicker crystals [27].

To take these effects into account, one approach is to record data in the simple way (hold pump stage fixed for each τ and measure $\Delta E_\tau(t)$ by sweeping detection stage), then deconvolve the signal along the t axis from the detector response, then project onto the appropriate time axis [79, 80]. Alternatively, one can simulate the data using finite-difference time-domain analysis, and take the detector response into account before comparison with data [91, 92]. This is the preferred approach taken in this dissertation.

Finite-difference time domain analysis

The finite-difference time-domain (FDTD) method is a numerical approach to solving Maxwell's equations [96, 97]. Because solutions are computed in the time-domain, it is ideally suited for analyzing time-resolved terahertz spectroscopy experiments [91, 92]. The process starts with Maxwell's equations in dielectric media in the absence of sources, reproduced here (in SI units) for completeness [69]

$$\begin{aligned} \nabla \cdot \mathbf{D} = 0, \qquad & \nabla \cdot \mathbf{B} = 0 \\ \nabla \times \mathbf{E} + \frac{\partial \mathbf{B}}{\partial t} = 0, \qquad & \nabla \times \mathbf{H} - \frac{\partial \mathbf{D}}{\partial t} = 0. \end{aligned} \tag{3.22}$$

Along with the constitutive relations $\mathbf{D}(t) = \epsilon(t) * \mathbf{E}(t)$ and $\mathbf{B}(t) = \mu(t) * \mathbf{H}(t)$, these provide a complete description of electrodynamics in materials (here '$*$' represents a convolution). For the purposes of this section, these equations can be greatly simplified. First, we are only interested in linear, isotropic, nonmagnetic media, so the directions of the fields do not change and $\mu(t) = \mu_0$. Additionally, we are only concerned with propagation in one spatial dimension, so we can choose $\mathbf{E} = E\hat{x}$ and $\mathbf{H} = H\hat{y}$ so that the curls become partial derivates in the $\hat{z}$ direction. Finally, we will rescale H by $Z_0 = \sqrt{\mu_0/\epsilon_0}$ so that the equations become

$$\begin{aligned} \frac{\partial D}{\partial x} = 0, \qquad & \frac{\partial H}{\partial y} = 0 \\ \frac{\partial E}{\partial z} + \frac{1}{c}\frac{\partial H}{\partial t} = 0, \qquad & \frac{\partial H}{\partial z} - \frac{1}{c}\frac{\partial D}{\partial t} = 0. \end{aligned} \tag{3.23}$$

To solve these equations numerically, we need to convert them into a set of discrete equations. The standard method of accomplishing this was introduced by Yee in 1966 [96]. He imagined that the electric and magnetic fields within a numerical cell were offset from each other by half a step Δz. Additionally, they were evaluated at time steps also offset by half a time step Δt. Then $D(z,t) \to D(k\Delta z, m\Delta t) \equiv D_k^m$ and $H(z,t) \to H[(k+\frac{1}{2})\Delta z, (m+\frac{1}{2})\Delta t] \equiv H_{k+\frac{1}{2}}^{m+\frac{1}{2}}$, where m and k are integers. Using this scheme, we can discretize the time

derivatives using finite-difference approximations [98], obtaining

$$\frac{\partial H}{\partial t} \approx \left[\frac{H_{k+\frac{1}{2}}^{m+\frac{1}{2}} - H_{k+\frac{1}{2}}^{m-\frac{1}{2}}}{\Delta t}\right]$$
$$\frac{\partial D}{\partial t} \approx \left[\frac{D_k^{m+1} - D_k^m}{\Delta t}\right]. \tag{3.24}$$

We next approximate the spatial derivatives in the same manner,

$$\frac{\partial H}{\partial z} \approx \left[\frac{H_{k+\frac{1}{2}}^m - H_{k-\frac{1}{2}}^m}{\Delta z}\right]$$
$$\frac{\partial E(t)}{\partial z} \approx \left[\frac{E_{k+1}^m - E_k^m}{\Delta z}\right]. \tag{3.25}$$

We can now insert these approximations into Maxwell's equations and solve for the fields at the most recent time step to obtain

$$H_{k+\frac{1}{2}}^{m+\frac{1}{2}} = H_{k+\frac{1}{2}}^{m-\frac{1}{2}} + \frac{c\Delta t}{\Delta z}\left[E_{k+1}^m - E_k^m\right] \tag{3.26}$$
$$D_k^{m+1} = D_k^m + \frac{c\Delta t}{\Delta z}\left[H_{k+\frac{1}{2}}^{m+\frac{1}{2}} - H_{k-\frac{1}{2}}^{m+\frac{1}{2}}\right]. \tag{3.27}$$

These equations are known as the update equations for FDTD in one dimension. For nondispersive media, D is related to E by simple multiplication: $D(t) = \epsilon E(t)$. It is then trivial to obtain E_m^k once D_m^k has been updated in Eq. (3.27).

In order to propagate a wave through the numerical grid, sources must be introduced. For the time dependence of the source field, we used a measured time-domain THz pulse. We first deconvolved it from the detector response using the method of Larsen *et al.* [92]. To introduce the source to the grid, we used the total field / scattered field method, which allows the introduction of a source which only propagates in one direction [99,100]. In addition to introduction of the source, proper boundary conditions must be implemented. If appropriate boundary conditions are not used, spurious reflections will occur at the boundary of the grid due to the fact that E_{N+1}^m and $H_{-\frac{1}{2}}^m$ are not defined at the edges of the

$N-$point grid. In 2D and 3D FDTD, the perfectly-matched layer is often used. While this method can also be used in 1D FDTD, we implemented a simpler solution known as the "perfect 1D boundary condition" [99].

To simulate materials with dispersive susceptibilities, simple division relating E_m^k and D_m^k is no longer possible. We used the auxiliary differential equation method [92,97,100, 101]. We first recall that in the frequency domain $D(\omega) = E(\omega)+P(\omega) = \epsilon_0[\epsilon_\infty+\chi(\omega)]E(\omega)$ where $P(\omega)$ is the material polarization, ϵ_∞ is the dielectric constant due to higher-lying optical resonances, and $\chi(\omega)$ is the electric susceptibility [69,73]. For a Lorentzian resonance, of which the Drude conductivity is a special case, $\chi(\omega) = \omega_p^2/(\omega_0^2 - \omega^2 + i\gamma\omega)$, so $P(\omega) = \epsilon_0[\omega_p^2/(\omega_0^2 - \omega^2 + i\gamma\omega)]E(\omega)$. The time-dependent polarization associated with this must therefore satisfy the differential equation

$$\frac{\partial^2 P}{\partial t^2} + \gamma\frac{\partial P}{\partial t} + \omega_0^2 P(t) = \epsilon_0\omega_p^2 E(t). \tag{3.28}$$

To avoid working with second-order derivatives, we define the time-dependent current function $J(t) \equiv \partial P(t)/\partial t$ [99]. Inserting this into Eq. (3.28) and applying the same finite-difference approximations as before, we obtain update equations for J and P:

$$\begin{aligned} J_k^{m+\frac{1}{2}} &= \left[\frac{2\epsilon_0\omega_p^2\Delta t}{2+\gamma\Delta t}\right] E_k^m + \left[\frac{2-\gamma\Delta t}{2+\gamma\Delta t}\right] J_k^{m-\frac{1}{2}} - \left[\frac{2\omega_0^2\Delta t}{2+\gamma\Delta t}\right] P_k^m \\ P_k^{m+1} &= P_k^m + \Delta t J_k^{m+\frac{1}{2}}. \end{aligned} \tag{3.29}$$

After obtaining P_k^{m+1}, we can find $E_k^{m+1} = (1/\epsilon_0)[D_k^{m+1} - P_k^{m+1}]$. Note that P and J occupy the same grid sites as E and D. The update procedure is then as follows:

1. update H using Eq. (3.26),
2. update J and P using Eqs. (3.29),
3. update D using Eq. (3.27),

4. update E by subtracting P from D.

In this way, the fields at future time $t + \Delta t$ can be calculated if the fields at time t are known, and the evolution of the fields in dispersive media can be simulated.

With these results in hand, it is straightforward to extend FDTD to simulate TRTS experiments. One simply makes the material parameters ω_p^2, γ, and ω_0^2 in Eq. (3.29) depend on timestep. In this way, one can simulate the propagation of a THz pulse through a material whose properties are changing during the propagation [91, 92]. By repeating the calculation at a variety of time delays τ, one can mimic realistic experimental conditions. Finally, the resulting FDTD data can be convolved with the detector response to compare with experiment.

3.2.4 Other frequency-domain artifacts

Another frequency-dependent artifact can arise when the pump spot size is smaller than THz probe spot [79]. This occurs because the THz spot size is often different for different frequencies, with higher frequencies (shorter wavelengths) being focused more tightly than lower frequencies (longer wavelengths). If the pump beam is smaller than the average THz spot size, then it may influence higher frequencies more than lower frequencies, which can skew the frequency dependence of the measured photoconductivity [79]. For this reason, we always kept the spot size of the pump beam around twice the size of the estimated THz spot size. The spot sizes of the 800 nm pump beam and the THz probe beam on the sample were typically $\sim$7 mm and $\sim$4 mm, respectively, to ensure approximately homogeneous photoexcitation of the probed sample area.

Chapter 4

Experimental techniques

A significant portion of this dissertation work involved building and improving the optical systems used to perform TRTS measurements in our lab. In this chapter, we outline several of these changes and describe techniques that were implemented to expand the capabilities of the experimental system.

4.1 Laser source

We used a Spectra-Physics Spitfire Pro titanium-doped sapphire (Ti:sapph) ultrafast amplifier as our laser source. The amplifier was seeded by a Tsunami Ti:sapph oscillator and pumped by an Empower 30 Q-switched Nd:YLF laser operating at 527 nm. The Tsunami was pumped by a Millennia Nd:YAG laser operating at 532 nm. The amplifier produced laser pulses with center wavelength 800 nm (photon energy $\hbar\omega = 1.55$ eV), full-width at half maximum (FWHM) time duration <100 fs, and energy around 800 μJ at a repetition rate of $f = 5$ kHz (average power ∼4 W). The pulses were first split by an 80/20 beam splitter, where 80% of the pulse was transmitted to be used for optical pump excitation. The remaining 20% was reflected and used for THz generation and detection. We used a pellicle beam splitter (nominally a 92%T/8%R beam splitter) to further split the laser pulses

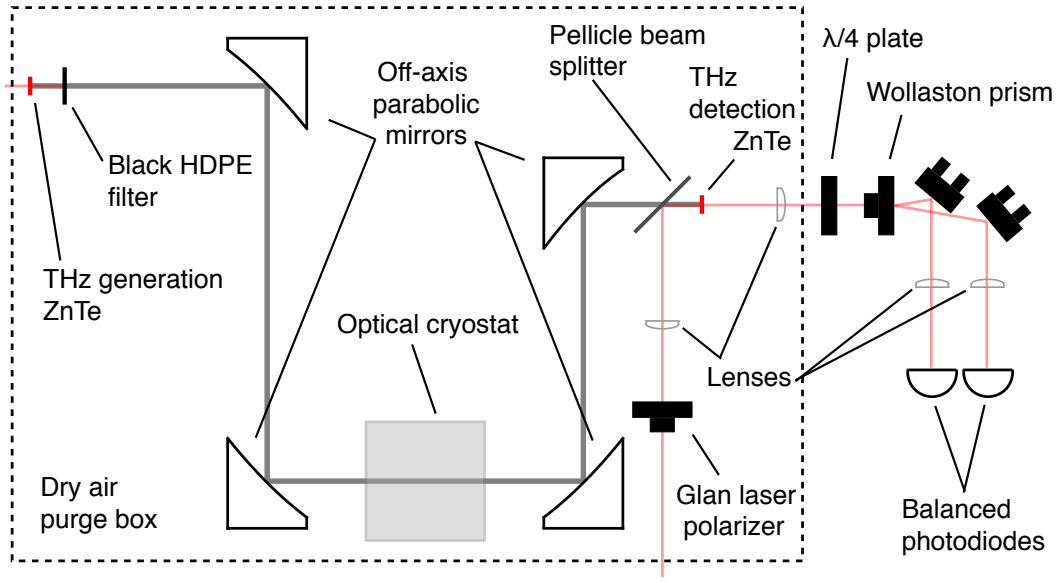

Figure 4.1: Schematic of terahertz spectroscopy setup in the Gedik Lab at MIT.

into the THz generation and THz detection paths. A schematic of our THz generation and detection setup is shown in Fig. 4.1. Details of THz generation and detection are discussed in the following sections.

4.2 Terahertz generation and manipulation

The THz probe pulses were generated by optical rectification of the 1.55 eV laser pulses in a 1 mm thick ZnTe crystal and detected by electro-optic sampling in a second ZnTe crystal (see next section for detection system details). We used a thin piece of black high-density polyethylene (HDPE) to block the residual generation beam. We chose HDPE because it is opaque to the 1.55 eV laser pulses and is highly transparent in the THz frequency range [27]. We used a set of four 90° off-axis parabolic mirrors (OAPMs) in a confocal geometry to collect the THz beam, focus it onto the sample, recollect it, and finally focus it onto the ZnTe detection crystal. Many groups use two pairs of identical OAPMs, but we have found

that using a shorter focal length for the final OAPM increased the dynamic range of the measurement. The longer focal length of the first OAPM set the desired magnification, while the short focal length of the final OAPM resulted in a smaller THz spot size on the detection crystal, which increased the field strength E_{THz} and hence the EO sampling signal $\Delta I/I_0$. The effective focal lengths of the OAPMS in our setup are 6", 4" ($\times$ 2), and 3" for mirrors 1–4, respectively.

To further improve the dynamic range of our measurements, we adjusted the power and spot size of the generation beam on the ZnTe generation crystal. The size of the beam was chosen to optimize the balance between diffraction losses associated with a small THz generation spot and minimizing the THz spot size at the sample. Assuming that the THz beam could be treated as a Gaussian beam expanding from a waist at the generation crystal, the spot size at the sample was set by the spot size on the crystal multiplied by the magnification ratio of the OAPMs (M=4"/6" = 0.67). We found that a generation beam radius ($1/e$ in intensity) of around 1 mm was optimum, *i.e.*, resulted in a small enough spot size at the sample but also allowed collection of sufficient low-frequency light. The power was controlled by a thin-film polarizer (Newport 11B00UP.26) and half-wave ($\lambda/2$) plate combination. We found that ∼220 mW of average power (pulse energy u = 44 μJ; fluence $\mathcal{F}$ = 700 μJ/cm^2) directed to the crystal was the maximum we could apply before the crystal began to glow white in the center, indicating higher-order or non-perturbative optical processes, which can cause long-term damage.

To improve the stability of the measured THz signal, we constructed an enclosure for the entire optical system. The enclosure was built from black anodized aluminum extrusions and black HDPE side panels with removable clear acrylic lids (80/20, Inc.). The generation beam path, from the laser output to the generation crystal, was therefore protected from fluctuations induced by air currents and, to some extent, local temperature

fluctuations. Additionally, the entire THz beam path was enclosed in a custom box that was constantly purged with dry air to reduce absorption lines caused by water vapor [102]. The relative humidity was kept below 0.1% during measurements. The dry air source was a commercial regenerative air dryer (DelTech WM-13N) which sourced the air from the building lines, filtered it, and dehumidified it with desiccant. The self-regenerative design of the air dryer allowed continuous operation with minimal service interventions (*e.g.*, desiccant replacement). This method was more cost-effective and convenient than purging with nitrogen gas. Since the air supply was essentially limitless, the flow rate could be made as high as necessary to purge the box. It was important, however, to set the flow to the minimum value necessary to achieve 0.1% relative humidity because high flow rates could introduce noise to the signal.

4.3 Detection system

In all measurements presented in this dissertation, the THz probe pulses were detected by EO sampling of the 800 nm laser pulses in a ZnTe crystal. As mentioned above, the thickness of the detection crystal influences the detector response function, which can cause error in the spectrum of the detected pulse if the sample properties change at a rate comparable to or greater than the bandwidth of the detector. For all static measurements, we used a 1 mm thick detection crystal to maximize the signal to noise ratio, since the detected signal is approximately linearly proportional to the crystal thickness [Eq. (3.10)]. For frequency-resolved ultrafast measurements, we used a thin detection crystal to minimize the errors associated with the detector response function [80]. Instead of simply using a thinner crystal, we used a hybrid crystal in which a 100 μm-thick layer of (110)-cut ZnTe was optically epoxied to a 1 mm-thick ZnTe with a different cut. The thick region did not

contribute to the EO sampling signal, but prevented the presence of multiple reflections (etalons) in the signal.

For the measurements presented in chapter 5, we measured the EO signal using the standard lock-in implementation. We used a pair of ThorLabs DET36A reverse biased photodiodes terminated with 110 kΩ resistors as our detectors. The output signals from the photodiodes were sent directly to the A and B inputs of a lock-in amplifier (Stanford Research Systems SR830). The amplifier was phase-locked to a mechanical chopper (New Focus 3501) and set to "$A-B$" mode to detect the difference between the A and B inputs. For equilibrium measurements, the chopper modulated the THz generation beam at a frequency asynchronous with the laser repetition rate. We typically used frequencies around 500 Hz. For time-resolved nonequilibrium measurements, the pump beam was chopped to allow detection of the small differential changes in the signal induced by the pump pulses. The lock-in signal was sent to a computer via a GPIB connection.

For the measurements presented in chapter 6, we collected the data with a data acquisition (DAQ) card as described by Werley *et al.* [103] instead of the conventional lock-in detection scheme. For equilibrium measurements, we chopped the THz generation beam at half of the laser repetition rate, $f/2 = 2.5$ kHz, so that every other generation pulse was blocked. As a result, the THz pulse was present for every other detection pulse that passed through the ZnTe detection crystal. For every two pulses emitted by the laser, four signals were measured: A_1, A_2, B_1, and B_2, corresponding to the peak intensities of the first and second pulses on diode A and diode B, respectively. From these signals, we extracted the EO sampling signal by calculating $\Delta I/I_0 \propto E_{\mathrm{THz}}$ as follows. We set the phase of the chopper such that the THz field was present for the first pulse but not the second. In that case,

$$\frac{1}{2}\left(\frac{A_1}{A_2} - \frac{B_1}{B_2}\right) = \frac{1}{2}\left(\frac{I_0 + \Delta I}{I_0} - \frac{I_0 - \Delta I}{I_0}\right) = \frac{\Delta I}{I_0}. \tag{4.1}$$

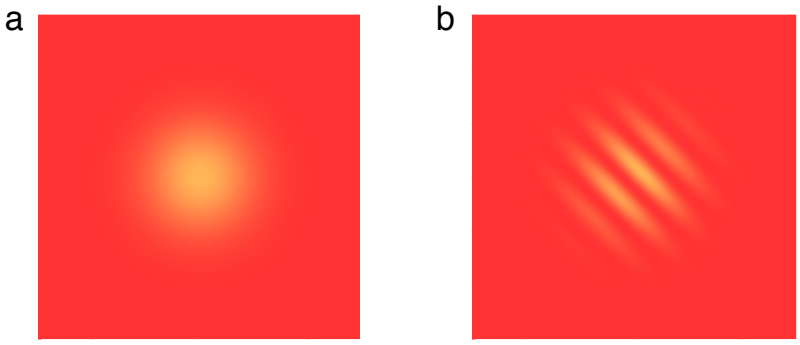

Figure 4.2: Depiction of method to set proper phase on generation beam chopper. (a) Generation beam spot on ZnTe when the chopper phase is set correctly. (b) Generation beam spot on ZnTe when the chopper phase is 90° away from the correct phase.

This method has the advantage that the recorded signal is directly proportional to the THz field, and the proportionality constants are known [Eq. (3.10)] (Refs. [27, 103]). One can therefore calculate the THz electric field strength directly. This is not necessary when simply performing spectroscopic measurements, but can be useful when using high-field THz pulses as the source of photoexcitation [104].

To implement the DAQ detection method, the optical chopper with a 60-slot wheel installed was used to modulate the THz generation beam. It was phase locked to a trigger signal provided by the laser system after having the timing adjusted by a digital delay generator (DDG, Stanford Research Systems DG535). The correct phase between laser trigger and chopper was chosen by looking at the laser spot on the ZnTe generation crystal after it passed through the chopper. To set the correct phase, we first adjusted the phase on the chopper controller until a notable interference fringe appeared across the center of the laser spot on the ZnTe generation crystal [Fig. 4.2(b)]. We then increased or decreased the phase by 90° to ensure that the entire generation beam spot was transmitted (pulse 1) or blocked (pulse 2) by the chopper blade [Fig. 4.2(a)]. The output from the chopper was sent to the DAQ card (National Instruments PCI-6143) to trigger the pulse sequence acquisition.

The sampling rate was set by a signal sent directly from the DDG to the DAQ card. The timing on the DDG was chosen so that the DAQ would sample the peak of the photodiode signal for each pulse [103].

For both detection methods, it was important to focus the detection beam at appropriate points along the beam path. Focusing the detection beam onto the ZnTe detection crystal greatly enhanced the THz signal because it ensured that essentially the entire detection spot was located at the center of the THz spot, where the THz electric field was strongest. This then increased the EO sampling signal since $\Delta I/I_0 \propto \max(E_{\mathrm{THz}})$. Without focusing, the EO signal would be proportional to the THz field strength averaged over the spot size, which could be around a factor of two smaller than $\max(E_{\mathrm{THz}})$. In our setup, we used a 2-to-1 telescope to focus onto the detection crystal with a 200 mm focal length plano-convex lens to focus and a 100 mm focal length plano-convex lens to re-collimate the beam. Beyond focusing onto the detection crystal, the 2-to-1 telescope had the added advantage that the beam was smaller after the telescope so that it was easier to guide through the $\lambda/4$ plate and Wollaston prism to the balanced photodiodes. It was also important to focus the detection beam onto the photodiodes. This ensured that the entire laser spot was within the active area of the diode and therefore reduced noise associated with pointing instability, which can cause a large beam to walk off the active diode area.

Minimizing the amount of scattered laser light that reached the diodes was also crucial to minimize noise. This was especially important for the lock-in detection method, since light scattered by the optical chopper was modulated at the same frequency as the actual THz signal. We implemented two methods to prevent scattered light from reaching the diodes. First, we placed the lenses that focused the detection beam onto the diodes inside long lens tubes mounted directly to the diode housing. This effectively reduced the numerical aperture by preventing light incident at large angles from reaching the detectors.

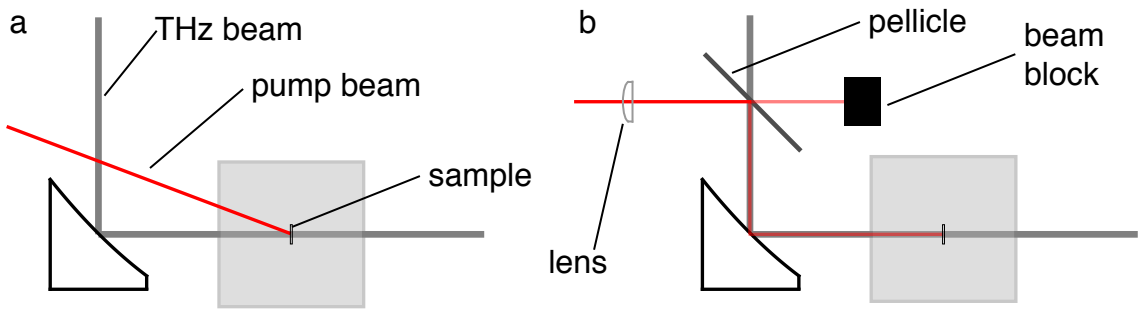

Figure 4.3: Schematic of different pump beam delivery methods. (a) Pump beam incident upon the sample at oblique incidence, appropriate for measurements with slow sample timescales. (b) Pump beam incident upon sample at normal incidence, useful when sample dynamics are fast. A pellicle beam splitter sends part of the pump beam to an off-axis parabolic mirror, which collimates and reflects the pump to the sample. The residual pump beam transmitted through the pellicle is blocked with a beam block.

Additionally, we used blackout materials to build an enclosure around the detection optics, which further prevented scattered laser light, as well as ambient room light, to reach the diodes. These two measures greatly improved the sensitivity of our TRTS system.

4.4 Optical pump-THz probe experiments

4.4.1 Pump beam delivery

We routed the pump beam to the sample two different ways, shown in Fig. 4.3. The first, and simplest, was to simply send the beam directly to the sample at an oblique angle [Fig. 4.3(a)]. This method worked well for samples which exhibited dynamics slow compared to the pulse widths, but degraded the time resolution when the dynamics were fast. This is because the THz spot size on the sample was large, typically a few mm across. The pump waist had to be even larger to ensure homogeneous photoexcitation, so the obliquely-incident pump pulse front did not reach the sample at the same time at each point of the sample surface, as depicted in Fig. 4.4. From this figure, it is apparent that the time smearing, defined as the difference in arrival time of the two edges of the pump pulse front,

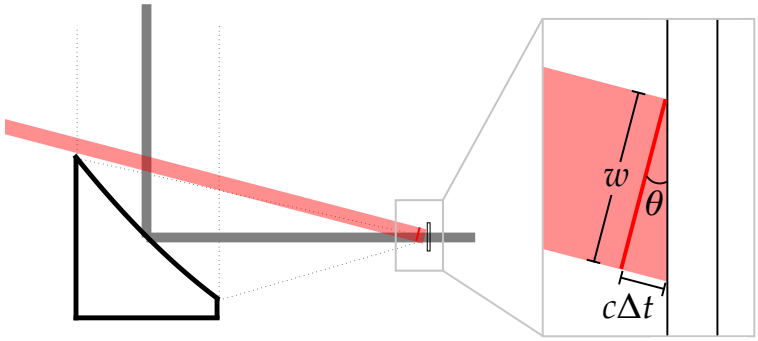

Figure 4.4: Diagram depicting the cause of temporal smearing when the pump beam is incident upon the sample at oblique incidence. Here w is the width of the pump beam, θ is the angle of incidence, and $\Delta t = w \tan\theta / c$ is the temporal smearing.

is $\Delta t = w \tan\theta / c$, where w is pump beam width, θ is the angle of incidence, and c is the speed of light. For a beam with width $w = 3$ mm incident at $\theta = 15°$, the time smearing is $\Delta t \approx 2.5$ ps. For samples such as conventional semiconductors and superconductors, decay times are typically tens of picoseconds, so this smearing does not adversely affect the measurements. In graphene, however, decay times are on the order of a few picoseconds, so the smearing introduced by an obliquely-incident pump beam can drastically affect the measured sample response.

The second pump beam routing method solved this problem by sending the pump beam to the sample at normal incidence, co-propagating with the THz probe beam [Fig. 4.3(b)]. To accomplish this, we inserted a large pellicle beam splitter coated for 50/50 reflection/transmission at 633 nm (Edmund Optics) into the THz beam path between the first two OAPMs. A lens was used to focus the pump beam before the pellicle. As the beam expanded, it was partially reflected by the pellicle. The reflected portion impinged upon the second OAPM, which collimated it and reflected it to the sample. Since the pump beam and probe beam then propagated collinearly, the time resolution was only limited by the pulse widths or detector response. Additionally, all photoexcited regions of the sample

experienced the same pump-probe delay, so no frequency or time dependent artifacts were introduced.

4.4.2 Detection for pump-probe measurements

The DAQ detection method described above has the additional advantage that it can easily be extended to nonequilibrium pump-probe measurements. For these experiments, we chopped the THz generation beam at frequency $f/2 = 2.5$ kHz and the pump beam at frequency $f/4 = 1.25$ kHz. During each period of the pump chopper, we measured the intensity of the four laser pulses that passed through the ZnTe EO detection crystal and reached the balanced photodiodes (A_i and B_i, with $i = 1 - 4$). In a typical sequence, the THz pulse was present in the ZnTe while the first and third pulses passed through, but not during the second and fourth (Fig. 4.5). For the first pulse, the THz had interacted with the sample in the presence of pump excitation, whereas for the third pulse, the THz had interacted with the sample without pump excitation. By comparing the pulses with and without THz (third and fourth), we extracted the THz field strength $E_0(t)$ using Eq. (4.1). By comparing the two pulses with that passed through the ZnTe crystal with THz, one with and one without the pump beam (first and third), we extracted the pump-induced change to the THz field, $\Delta E_\tau(t)$ as follows. We denote the intensities of the pulses that reach the diodes $I_0 \pm \Delta I$ when the THz was present without the pump and $I_0 \pm (\Delta I + \delta I)$ when both pump and THz were present. Then

$$\begin{aligned} \frac{1}{2}\left(\frac{A_1}{A_3} - \frac{B_1}{B_3}\right) &= \frac{1}{2}\left(\frac{I_0 + (\Delta I + \delta I)}{I_0 + \Delta I} - \frac{I_0 - (\Delta I + \delta I)}{I_0 - \Delta I}\right) \\ &= \frac{1}{2}\left(\frac{\delta I}{I_0 + \Delta I} + \frac{\delta I}{I_0 - \Delta I}\right) \\ &= \frac{\delta I}{I_0}\left(\frac{1}{1 - (\Delta I/I_0)^2}\right). \end{aligned} \tag{4.2}$$

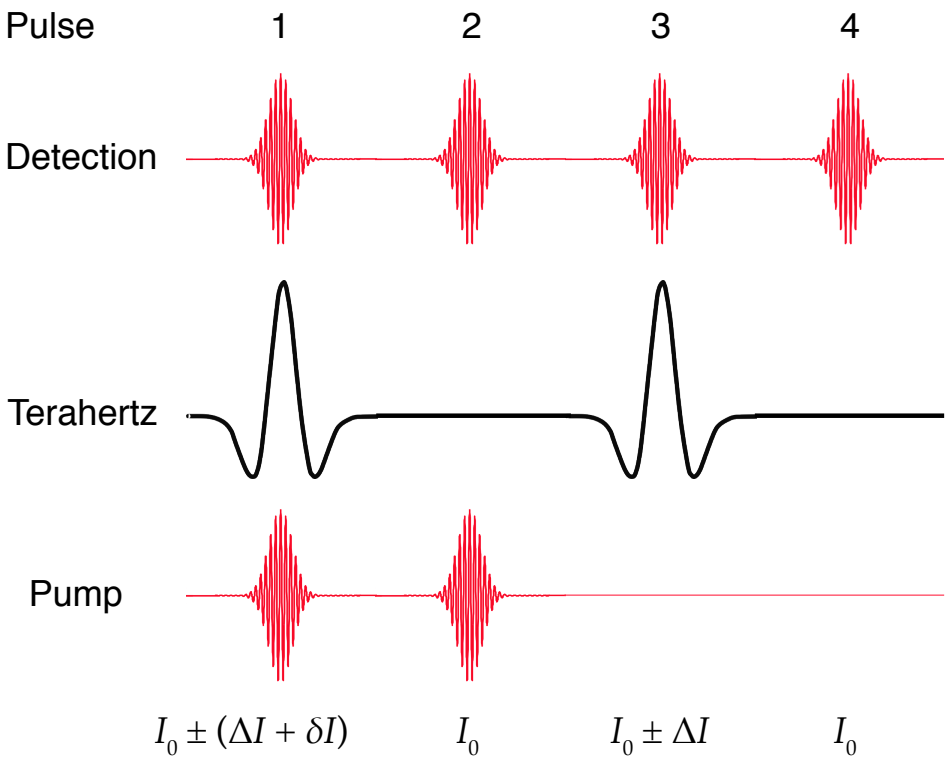

Figure 4.5: Pulse sequence for double modulation DAQ detection in optical pump-THz probe measurements. After passing through the ZnTe detection crystal, each of the four detection pulses passed through a quarter-wave plate and was split by a Wollaston prism. The cross-polarized pulses were then sent to a pair of balanced photodiodes A and B. The bottom row labels the intensity of the each detection pulse that reached the photodiodes ("+" sign is for diode A and "−" sign is for diode B). Refer to the text for further details.

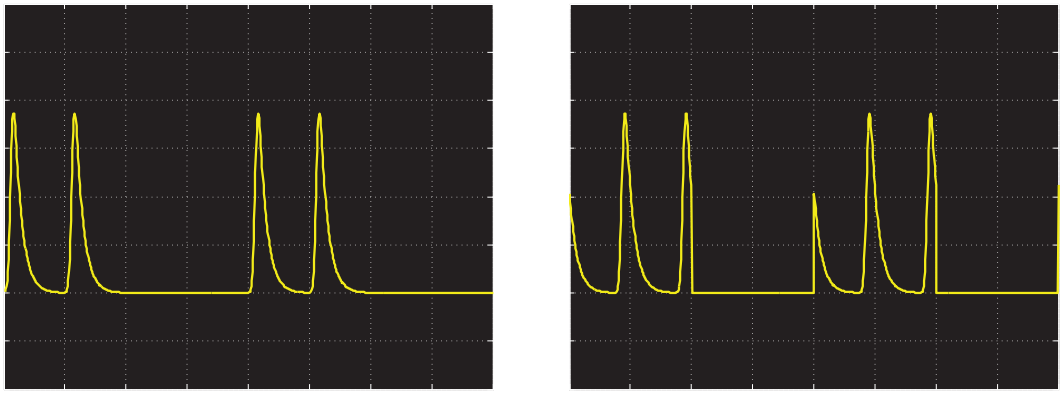

Figure 4.6: Simulated oscilloscope signal used to set the phase of the pump beam chopper. Left panel shows what the signal should look like when the phase is set correctly. Right panel shows that the phase is incorrect because the chopper blade is not fully blocking one of the pump beam pulses.

Since $\Delta I/I_0$ was at most $\sim$12% in our measurements (and typically $\sim$2.5%), the quantity in parentheses was always $\lesssim 1.01$ and neglecting it therefore introduced at most a 1% error. Importantly, it was always the same for a given equilibrium field $E_0(t = t_0)$, and so did not depend on pump-probe delay τ. It therefore could not introduce spurious signals (*e.g.,* a sign change) into a measurement of $\Delta E_\tau(t = t_0)/E_0(t = t_0)$.

To implement this scheme, we used a ThorLabs MC2000 chopper controller with MC1F60 chopper blade installed to modulate the pump beam at one-fourth the laser repetition rate. The blade rotation was triggered by the output of the New Focus optical chopper that chopped the generation beam. To set the correct phase of the pump beam chopper, we used a photodiode to detect scattered light from the pump beam after passing the chopper. The diode signal was sent to an oscilloscope and triggered on the chopper output. When the chopper phase was set correctly, the pulse train comprised pairs of pulses separated by 400 µs [Fig. 4.6, left panel]. Signs of more than two pulses indicated that the phase was not set correctly [Fig. 4.6, right panel]. Once the phase was set correctly, the trigger signal from the

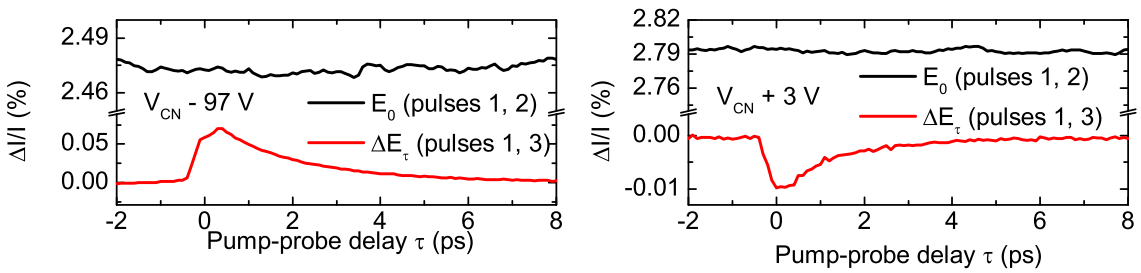

Figure 4.7: Raw data from 1D pump scans on graphene recorded using differential chopping and DAQ card detection at two different applied gate voltages. Black lines show the equilibrium field $E_0(t)$, while red lines show the pump-induced change to the field, $\Delta E_\tau(t)$. Simultaneous acquisition of $E_0(t)$ and $\Delta E_\tau(t)$ reduces systematic error due to drift of the laser system.

ThorLabs MC2000 was sent to the DAQ card to trigger the pulse sequence acquisition. The signal from the photodiodes was then collected at a sampling rate set by the laser trigger from the DDG.

Examples of raw data collected using this scheme are shown in Fig. 4.7. These plots show $E_0(t)$ (black lines) and $\Delta E_\tau(t)$ (red lines) collected by photoexciting a graphene sample at high electron doping (left panel) and near the charge neutrality point (right panel). Because this method allowed simultaneous measurement of $E_0(t)$ and $\Delta E_\tau(t)$, it reduced systematic errors associated with drift of the laser system [103, 105]. We confirmed that our measurement yielded the correct sign of the photoconductivity by comparing to the photoconductivity measured on a reference Si or GaAs sample. Further discussion of the data in this figure is presented in chapter 6.

Chapter 5

Observation of negative terahertz photoconductivity in doped graphene

Optical pump excitation has been shown to effectively modulate the THz response of graphene. In particular, previous studies reported enhanced absorption of THz radiation in optically pumped graphite and graphene [33,106–108]. In these works, the observation was understood by considering Drude absorption with a fixed (energy-independent) scattering rate, which typically increased with the population of photoexcited carriers. However, the small Fermi energy of charge carriers in graphene suggests that non-Drude behavior is likely to occur at the high transient temperatures encountered in pump-probe experiments, and the coupling of carriers to hot phonons may alter their scattering rates.

In this chapter,[1] we present optical pump-THz probe [24, 25] measurements of the ultrafast far-infrared response of large-area monolayer graphene grown by chemical vapor deposition (CVD). We observed a transient decrease of THz absorption in graphene subject to pulsed optical excitation, a result in contrast with the increased absorption reported previously for epitaxial graphene [106–108]. In addition, the differential THz conductivity

[1]Most of this chapter is reproduced with permission from A. J. Frenzel, C. H. Lui, W. Fang, N. L. Nair, P. K. Herring, P. Jarillo-Herrero, J. Kong, N. Gedik, Observation of Suppressed Terahertz Absorption in Photoexcited Graphene, *Applied Phyiscs Letters* **102**, 113111. Copyright (2013) by the American Institute of Physics.

spectrum deviated significantly from the Drude form. We propose that the observed anomalous THz bleaching arises from additional scattering of electrons with optical phonons in graphene and on the substrate, as well as thermal broadening of the electron distribution under non-equilibrium conditions.

5.1 Sample description and characterization

Monolayer graphene samples were grown by CVD [109] on copper foils and subsequently transferred to different THz-transparent substrates, including sapphire, z-cut crystalline quartz, and borosilicate glass. The monolayer thickness and sample quality of the CVD graphene were characterized by Raman spectroscopy (inset of Fig. 5.1). The narrow, symmetric Lorentzian peak at $\sim$2700 cm^{-1} indicates that the sample is monolayer graphene. The absence of a significant feature at $\sim$1350 cm^{-1} suggests that the sample has low structural disorder [110]. We measured the THz absorption spectrum of the CVD samples without optical excitation and extracted the complex optical conductivity of graphene using the method described in §3.1.2. Fig. 5.1 displays the conductivity spectrum of a graphene sample on a quartz substrate at room temperature. The data can be fit well by the Drude formula

$$\tilde{\sigma}(\omega) = \frac{D}{\pi(\Gamma - i\omega)} \approx \frac{2e^2}{h}\left(\frac{\varepsilon_\mathrm{F}}{\hbar\Gamma - i\hbar\omega}\right) \tag{5.1}$$

with a Fermi energy $\varepsilon_\mathrm{F} \sim 300$ meV and scattering rate $\Gamma \sim 12$ meV (3 THz), corresponding to a carrier density $n \sim 6 \times 10^{12}$ cm^{-2} and mobility $\mu = ev_\mathrm{F}^2/\Gamma\varepsilon_\mathrm{F} = 2000$ cm^2/V·s. These parameters are typical for doped CVD graphene on a substrate [11, 12, 14, 111]. The approximation $D \approx (e^2/\hbar^2)\varepsilon_\mathrm{F}$ is valid because $\varepsilon_\mathrm{F} \gg k_\mathrm{B}T$, as discussed in §2.2.1.

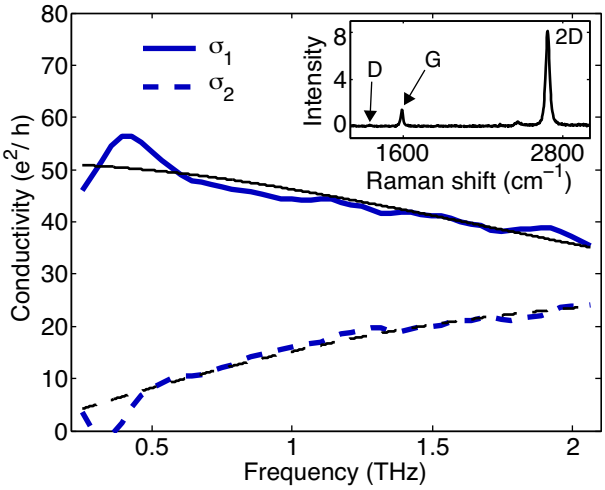

Figure 5.1: Complex optical sheet conductivity of graphene from 0.21 to 2.1 THz in units of e^2/h. The measurement was performed at room temperature on monolayer CVD graphene on a quartz substrate (without optical excitation). A bare quartz substrate was used as a reference. The blue solid and dashed lines are the real (σ_1) and imaginary (σ_2) part of the conductivity, respectively. The data can be fit by the Drude model (thin black lines) with carrier scattering rate $\Gamma/2\pi = 3$ THz. The inset shows a typical Raman spectrum of our CVD graphene (excitation wavelength 532 nm). The narrow Lorentzian line shape of the 2D mode confirms the monolayer thickness of the samples. The small D-mode signal indicates the high crystalline quality of the samples.

5.2 Experimental results

Measurements presented here were performed in the low fluence regime (incident pump fluence $\sim$10 μJ/cm^2) at room temperature and in high vacuum (pressure $< 10^{-5}$ Torr). Using the two-temperature model of Ref [44], we estimate that under our experimental conditions, the maximum transient electronic temperature was $\lesssim$ 1000 K and equilibrium heating of the lattice was negligible. When we pumped the graphene/quartz sample with 800 nm pulses, we observed a significant change in the transmitted THz probe pulses [Fig. 5.2(a)]. Strikingly, the THz transmission was found to increase following pulsed excitation. For a thin film deposited on a transparent substrate, the differential transmitted electric field ΔE_τ, normalized to the equilibrium transmitted field E_0, is related to the differential optical conductivity $\Delta\sigma_\tau$ as (§3.2.2)

$$\frac{\Delta E_\tau}{E_0} = -\left(\frac{Z_0}{n_s+1}\right)\Delta\sigma_\tau \tag{5.2}$$

where n_s is the substrate refractive index and $Z_0 = 2\alpha(h/e^2)$ the impedance of free space. Our observation of positive ΔE_τ therefore corresponds to negative differential conductivity, or reduced absorption, in graphene.

Fig. 5.2(b) displays the temporal dynamics of the pump-induced modulation of the THz transmission, which are well described by an exponential decay with time constant $1/\gamma = 1.7$ ps (Fig. 5.2(b) inset). These data were collected by synchronously adjusting the detection and pump beam path lengths to ensure that all parts of the THz signal experienced the same pump-probe delay as described in §3.2.3. It is firmly established that photoexcited charge carriers in graphene thermalize rapidly and relax some of their energy to a set of strongly coupled optical phonons within a few hundred femtoseconds [33, 44, 49–51, 112]. The equilibrated subsystem of electrons and optical phonons subsequently cools within a few picoseconds through the anharmonic decay of the optical phonons. We therefore attribute

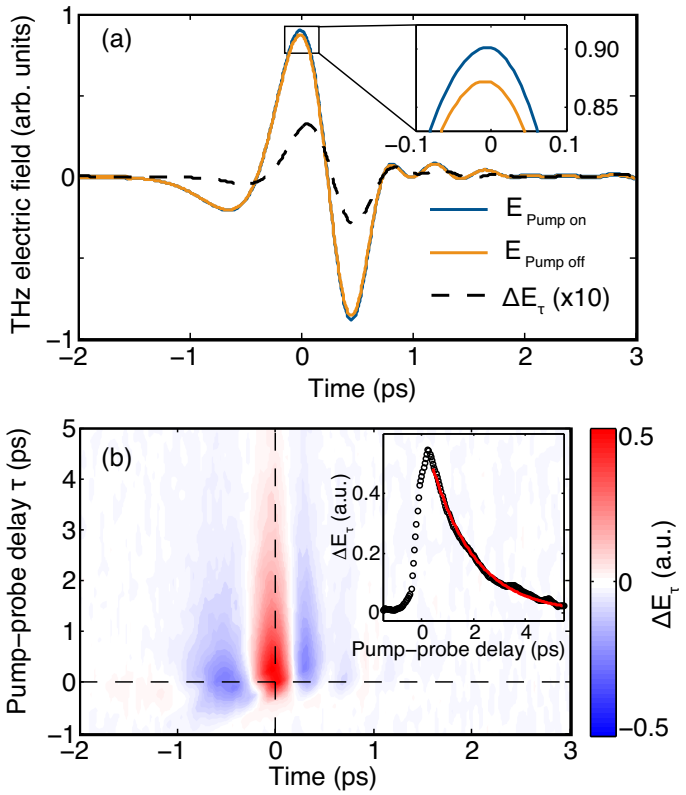

Figure 5.2: (a) Transmission of the THz electric field with (blue) and without (orange) pump excitation, measured by chopping the THz generation beam. The dashed line is the pump induced modulation of the transmitted electric field ΔE_τ, scaled by a factor of 10 for clarity. The inset shows a zoomed-in view of the peak, indicating that ΔE_τ corresponds to a pump-induced bleaching of the graphene sample. (b) Temporal dynamics of ΔE_τ following optical pump excitation, measured by chopping the pump beam. The horizontal and vertical dashed lines are, respectively, the zero pump-probe delay time and the peak position of ΔE_τ. Inset shows the temporal dynamics of the peak of ΔE_τ (vertical dashed line in main panel). The red line is a fit to $\Delta E_\tau = A \exp(-\gamma\tau)$ with time constant $1/\gamma = 1.7$ ps. The peak value of the signal corresponds to $\Delta E_\tau / E_0 \sim 5\%$.

the observed dynamics of the THz response to the cooling of the coupled electron-phonon system.

We used Eq. (5.2) to extract the complex differential conductivity spectra ($\Delta\tilde{\sigma}_\tau = \Delta\sigma_{\tau,1} + i\Delta\sigma_{\tau,2}$) from the transmission data in Fig. 5.2(b) at different pump-probe delay times [Fig. 5.3(a)]. We found that $\Delta\sigma_1$ remained negative for the whole decay process after pulsed excitation [Fig. 5.3(a)], and for the entire measured spectral range [see, for example, the spectrum at pump-probe delay 1 ps in Fig. 5.3(b)]. We note that we observed negative $\Delta\sigma_\tau$ of similar magnitude and lifetime (both with variation $< 20\%$) at temperatures ranging from 4 to 300 K. The response was also found to be similar for CVD graphene samples on different substrates (sapphire, quartz and borosilicate glass), and in both ambient and vacuum conditions. We therefore conclude that it is a general property of highly doped graphene on a substrate. The results are surprising because the intraband absorption of graphene is typically described by the Drude model with a constant scattering rate. Increasing the free carrier population by photoexcitation should lead to enhanced THz absorption, as observed in epitaxial graphene layers on SiC substrate [106–108], as well as in traditional semiconductors such as GaAs [80] and Si [89]. The explanation of our experimental data must therefore lie beyond this simple picture.

5.3 Analysis and discussion

The negative sign and non-Drude spectral shape of the measured differential THz conductivity in graphene [Fig. 5.3(b)] can be qualitatively understood by considering the increased scattering rate and broadened carrier distribution present in the transient regime, where the electron and phonon systems are driven to considerably higher temperatures than in equilibrium. After pulsed excitation, thermalization and cooling of photoexcited carriers are

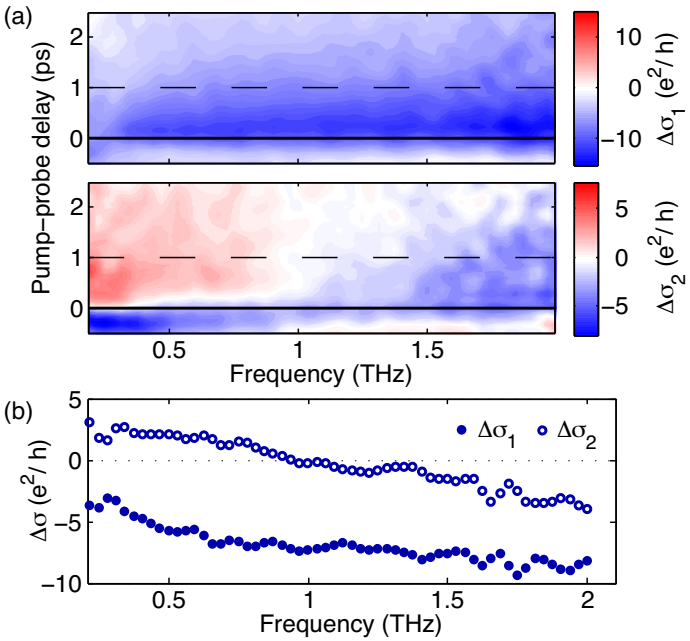

Figure 5.3: (a) Temporal dynamics of the real (upper panel) and imaginary (lower panel) parts of the differential THz conductivity of optically pumped monolayer graphene. The black solid line denotes zero pump-probe delay time. (b) Differential THz conductivity 1 ps after optical excitation (horizontal dashed lines in (a)). The filled and open circles denote the experimental real ($\Delta\sigma_1$) and imaginary ($\Delta\sigma_2$) parts of the conductivity, respectively.

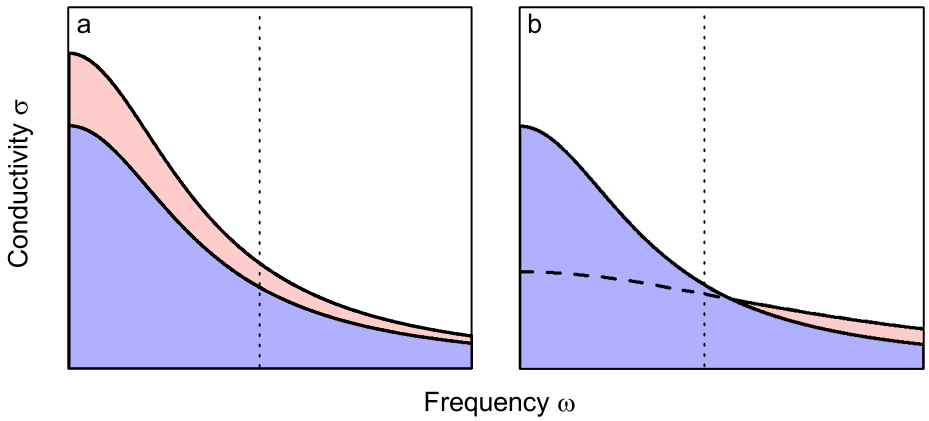

Figure 5.4: Two scenarios for photoinduced changes to Drude conductivity in graphene. (a) Photoexcitation increases Drude conductivity (red area) relative to value before photoexcitation (blue area) due to presence of photoexcited carriers. (b) Photoexcitation changes shape of Drude conductivity (red area) relative to shape before photoexcitation (blue area) due to increased scattering. In this case, the measured conductivity will be lower at frequencies below the initial scattering rate but higher at frequencies above the initial scattering rate. Our measurements were performed in the frequency range to the left of the vertical dashed lines. Hence, we observed negative photoconductivity in our doped graphene samples, corresponding to the mechanism depicted in panel (b).

expected to proceed via emission of strongly coupled optical phonons [49–51] and remote substrate phonons [38]. The enlarged phase space for scattering at higher carrier temperature, combined with the increased phonon populations, can result in significantly stronger electron-phonon scattering. Suppression of free-carrier conductivity due to electron-phonon scattering at elevated temperature has been observed in ultrafast studies of graphite [33] and dc transport studies of graphene [41]. This mechanism is also responsible for the current saturation observed in high-field transport studies of graphene devices [36, 46, 113, 114]. A recent THz pump-THz probe study also showed signatures of increased intraband scattering due to heating the electron system with an intense THz pulse [115]. We therefore expect that increased electron-phonon scattering in the transient regime will lead to the observed negative differential THz conductivity. A schematic of this mechanism is shown in Fig. 5.4.

Beyond increased electron-phonon scattering, the energy dependence of carrier scattering must be considered because of the thermally broadened distribution of the hot ($k_{\mathrm{B}}T_{\mathrm{e}} \sim \mu$) carriers [86]. This will lead to the observed non-Drude spectral shape because the Drude model assumes a constant (energy independent) scattering rate [29]. The effect of energy-dependent scattering rates on terahertz photoconductivity has recently been analyzed in more detail by Jensen *et al.* [116]. Their results are partially consistent with the picture presented in this chapter. They claim that their model, which neglects temperature-dependent electron-phonon scattering, reproduces all of their experimental results. We were unable to reproduce our results without including increased electron-phonon scattering (see chapter 6).

In summary, we observed reduced absorption of THz radiation and a non-Drude differential conductivity spectrum in graphene subject to pulsed optical excitation. Our results can be explained by additional electron-phonon scattering in conjunction with a thermally broadened carrier distribution. This work demonstrates that the THz response of graphene is strongly tunable by optical means over a broad frequency range on an ultrafast picosecond timescale.

Chapter 6

Semiconducting-to-metallic photoconductivity crossover in graphene

The intrinsic properties of Drude absorption in graphene can be revealed by studying its dynamical response to photoexcitation. In particular, optical pump-terahertz probe spectroscopy provides access to a wide transient temperature range via pulsed optical excitation, and allows measurement of the ac Drude conductivity by a time-delayed terahertz (THz) probe pulse [24]. This technique has been applied to study transient photoconductivity (PC) in graphene, but conflicting results have been reported [24,33,61,85,86,107,108,117–119]. Positive PC was observed in epitaxial graphene on SiC (Ref. [106–108]), while negative PC was seen in graphene grown by chemical vapor deposition (CVD) [61,85,86,117]. It has been argued that the opposite behavior in these samples arises from their different charge densities. Here we study graphene samples with gate tunable carrier density to resolve these issues and further reveal the unique Drude response of massless Dirac fermions.

In this chapter,[1] we present an investigation of the Drude absorption dynamics in

[1]Most of this chapter is reproduced with permission from A. J. Frenzel, C. H. Lui, Y. C. Shin, J. Kong, N. Gedik, Semiconducting-to-Metallic Photoconductivity Crossover and Temperature-Dependent Drude Weight in Graphene, *Physical Review Letters* **113**, 056602. Copyright (2014) by the American Physical Society.

graphene over a wide range of carrier density and temperature. Using optical pump-THz probe spectroscopy, we drove the carriers to high transient temperature and probed the Drude absorption of the hot carriers as they relaxed to equilibrium. By adjusting the gate voltage, pump-probe delay, and excitation fluence, we were able to observe the change of Drude absorption over a broad range of carrier density and transient temperature. Near the charge neutrality point, our samples exhibited positive (semiconducting) ultrafast PC, due to thermal excitation of electron-hole pairs after photoexcitation. At high charge density, however, the same samples exhibited negative (metallic) PC due to the decrease of both the Drude weight and the carrier scattering time at high transient temperature. The observed density-dependent PC provides a unifying framework for understanding previously reported positive PC in (undoped) epitaxial graphene and negative PC in (p-doped) CVD graphene. Additionally, at low charge density, we observed unusual fluence dependence of the THz Drude response, where the PC first decreased and then increased as the carrier temperature increased. This is consistent with the behavior expected from the non-monotonic temperature dependence of the Drude weight in graphene. By using the Drude model with an estimated temporal evolution of the hot carrier temperature, we were able to reproduce all the main features of our observations.

6.1 Sample description and characterization

A key advance in our experiment was the fabrication of large-area gated graphene devices without a THz PC response from the substrate [Fig. 6.1(a)]. This is not possible with commonly used SiO_2/Si substrates, which produce large background signal in optical pump-THz probe experiments (Fig. 3.8). We used z-cut crystalline quartz substrates and deposited 35-nm indium tin oxide (ITO) and 400-nm parylene-C thin films as the back-gate electrode

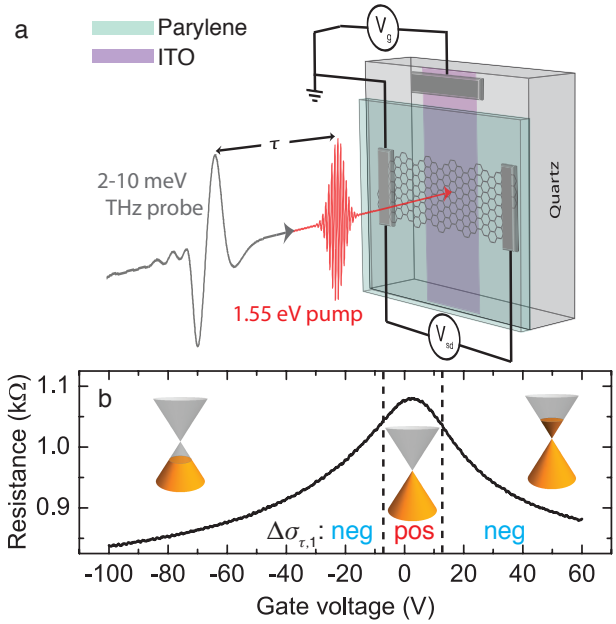

Figure 6.1: (a) Schematic of transparent graphene device geometry and experimental method described in the text. (b) Two-terminal resistance of our device as a function of back gate voltage V_g. The charge neutrality point, corresponding to maximum resistance, is at $V_g = V_{CN} = 3$ V. Voltage ranges of positive and negative photoconductivity ($\Delta\sigma_{\tau,1}$) observed in our experiment are separated by dashed vertical lines.

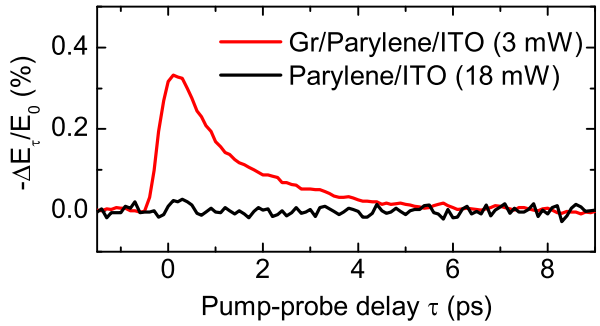

Figure 6.2: Measured temporal evolution of the negative change of the transmitted THz electric field normalized by the equilibrium THz field at $t = 0$, i.e., $\Delta E_\tau(t = 0)/E_0(t = 0)$, for a device before and after the deposition of graphene on the parylene/ITO/quartz substrates. We used higher pump power (18 mW) in the measurement without graphene than that with graphene (3 mW) to highlight the negligible photoconductivity of the substrates. Both measurements were performed at room temperature. The graphene carrier density was set to the charge neutrality point.

and dielectric, respectively. The z-cut crystalline quartz substrates have slightly higher refractive index but significantly lower absorption than commonly used fused silica substrates [27]. We experimentally confirmed that the back-gate structure had negligible pump-probe response (Fig. 6.2). This ensured that all measured pump-probe signals derived from the graphene layer. High quality, large area, monolayer CVD graphene sheets [109] were transferred onto our back-gate substrates. Graphite-paint source and drain electrodes were attached to graphene with a separation of ∼5 mm. The devices exhibit excellent bipolar gating behavior with low unintentional doping [Fig. 6.1(b); gate voltage $V_g = 3$ V $\equiv V_{CN}$ at charge neutrality, corresponding to unintentional hole doping $p = 1.7\times10^{11}$ cm^{-2}, estimated from our device capacitance].

ITO is a widely used transparent conducting oxide. Our films were deposited by radio-frequency (RF) magnetron sputtering in an Ar gas environment. Since the optical and electrical properties of ITO films depend strongly on RF power [120], oxygen partial pressure [121], and annealing conditions, we could choose the growth conditions to produce films with the desired properties (mostly transparent to THz pulses but conducting enough

to act as gate electrode). By sputtering at high RF power and no oxygen partial pressure, we obtained as-grown films with sheet resistances ∼500 Ω/□ as measured by TDTS and four-probe electrical measurements. The TDTS measurements revealed a frequency-independent conductance. The average sheet resistance of 500 Ω/□ corresponds to about 80% transmission through the film, sufficient to allow TRTS measurements with high dynamic range.

We also measured the Hall effect in the four probe van der Pauw geometry for an ITO film prepared under identical conditions to the ones in our devices. We found an electron density $n \approx 2 \times 10^{15}$ cm^{-2} and mobility $\mu \approx 6$ cm^2/V s. This density is three orders of magnitude larger than the highest gate-tuned carrier density in our experiment, while the mobility is more than two orders of magnitude smaller than that of graphene. Using the effective mass of carriers in ITO, $m^* = m_e/2$ [122], we could extract the carrier scattering rate using $\Gamma_{\mathrm{ITO}} = e/(\mu m^*)$. The extracted value of $\Gamma_{\mathrm{ITO}}/2\pi = 93$ THz is consistent with the flat frequency response we observed in TDTS measurements. We therefore do not expect any significant influence of the electrostatic gating on the properties of the ITO layer.

Parylene is a polymer which can be used to form large-area, pinhole-free coatings [123]. We deposited the parylene-C thin films using a Specialty Coating Systems Labcoter2. Using the reported room temperature dielectric constant $\epsilon_r \approx 4$ for parylene-C [124], we estimated the capacitance of our device to be $C = \epsilon_r \epsilon_0 / d \approx 8.9$ nF/cm^2. Here $\epsilon_0 = 8.85 \times 10^{-12}$ F/m is the permittivity of free space and $d = 400$ nm is the thickness of the dielectric layer (see below). We then estimated the gate-induced carrier density by the formula $n = CV/e$, yielding $n \approx 5.5 \times 10^{10} \times V$ cm^{-2}, where V is the gate voltage in units of Volt. This is comparable to standard Si/SiO_2 graphene devices, where $C \approx 13$ nF/cm^2 [3].

The thicknesses and optical constants of the parylene-C gate dielectric and ITO gate electrode were measured by spectroscopic ellipsometry (J.A. Woollam, Co., Inc. WVASE). In both cases, we deposited films on silicon wafers with ∼300 nm of thermal oxide grown

on the surface. This removed ambiguity related to the native oxide thickness on silicon, since the thickness of the thermal oxide could be quantified before film deposition and the optical constants of both Si and SiO_2 are well known [125]. The films were deposited simultaneously with the films used for devices. For both parylene and ITO films, several models were tested to best fit the measured ellipsometric parameters. The parylene data were best fit with a two-parameter Cauchy model and surface roughness incorporated using an effective-medium approximation at the air-parylene and parylene-SiO_2 interfaces. The overall extracted thickness of the film, $d \approx 400$ nm, was insensitive to varying the optical constants. Additionally, the index of refraction at 633 nm agreed with the literature value $n = 1.64$ to within 0.5%. Finally, the surface roughness agreed well with AFM data on films grown under similar conditions. The ITO data were equally well fit by a single Drude oscillator or a Drude-Lorentz model to account for interband transitions [121]. Both fits yielded a similar thickness around 35 nm and similar fit quality. The thickness also agreed with that measured by AFM in a patterned film grown under nominally identical conditions.

6.2 Tunable terahertz photoconductivity

The graphene devices, investigated at room temperature in high vacuum ($P < 10^{-5}$ Torr), were photoexcited with 100 fs laser pulses at 1.55 eV photon energy generated using a 5 kHz amplified Ti:sapph laser system. The transient PC was probed by measuring the complex transmission coefficient of time-delayed picosecond THz pulses (photon energy 2-10 meV) with controllable time delay τ [Fig. 6.1(a)]. In these measurements, the local detection time of the picosecond THz pulse was synchronized with the pump pulse such that the whole THz waveform experienced the same time delay after photoexcitation [79] (see also §3.2.1). To reduce experimental errors associated with laser drift, we simultaneously

measured the electric field waveform $E_0(t)$ of the THz pulse transmitted through the sample without the optical pump and the optical pump-induced change of the transmitted field $\Delta E_\tau(t)$ via electro-optic sampling using a data acquisition card [103, 105]. The resulting ratio $-\Delta E_\tau/E_0$ (referred to as "differential field") approximately represents the PC, $\Delta\sigma_{\tau,1}$ (Refs. [24, 33, 61, 85]).

6.2.1 Experimental results

Pump-probe measurements with incident pump fluence $\mathcal{F} = 10\,\mu\text{J/cm}^2$ and pump-probe delay $\tau = 1.5$ ps revealed that the sign of the PC could be changed from positive near charge neutrality to negative at moderate carrier density [Fig. 6.3]. The measured $\Delta E_\tau(t)$ near charge neutrality ($V_\text{g} = V_\text{CN} + 2$ V) is opposite in sign to $E_0(t)$ for all t, reflecting a photo-induced increase in absorption [Fig. 6.3(a)]. The extracted PC spectrum $\Delta\sigma_\tau(\omega) = \Delta\sigma_{\tau,1} + i\Delta\sigma_{\tau,2}$, calculated with the device geometry taken into account, shows a positive real part [Fig. 6.3(b)]. In sharp contrast, $\Delta E_\tau(t)$ has the same form and sign as $E_0(t)$ when $V_\text{g} = V_\text{CN} + 52$ V ($n \approx 3 \times 10^{12}$ cm^{-2}), indicating a photo-induced decrease in absorption [Fig. 6.3(d)]. As expected, the real part of the PC, $\Delta\sigma_{\tau,1}$, is negative in this case [Fig. 6.3(e)].

Frequency-resolved transient conductivity data were collected following the procedure first outlined by Beard *et al.* [79] and described in §3.2.3. Namely, the pump beam delay and detection beam delay were synchronously scanned to ensure that all points of the measured THz waveform experienced the same pump-probe delay. This procedure eliminated frequency-dependent artifacts in transient conductivity spectra that occur when different points of the transmitted THz pulse experience different pump-probe delays [126]. The measured signal at short pump-probe delays can be contaminated by artifacts resulting from the detector response function, due to the finite bandwidth of electro-optic detection [79].

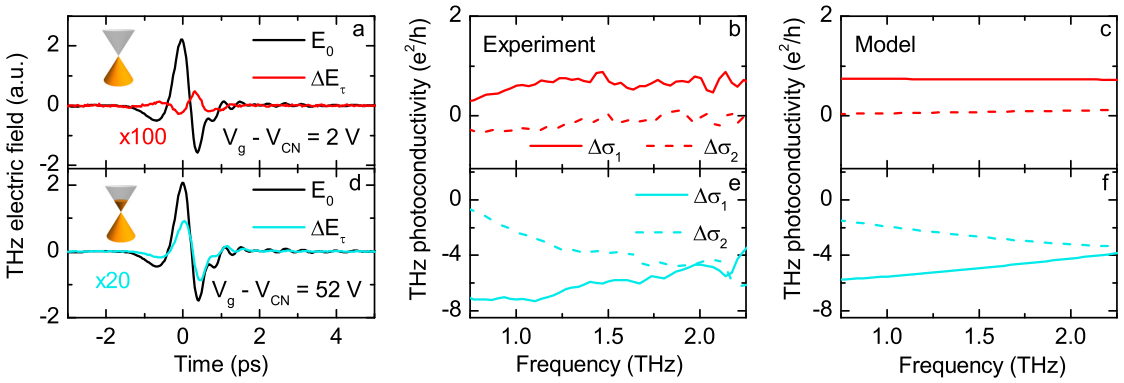

Figure 6.3: (a) Measured THz electric field waveform transmitted through the sample in equilibrium (black line) and pump-induced change in transmitted THz electric field (red line) at $\tau = 1.5$ ps. Measurements were performed at room temperature in vacuum with the carrier density set near charge neutrality ($V_g = V_{CN} + 2$ V) and incident pump fluence $\mathcal{F} = 10$ μJ/cm^2. (b) Real ($\Delta\sigma_1$, solid line) and imaginary ($\Delta\sigma_2$, dashed line) parts of the transient THz PC extracted from the data in (a). (c) Theoretical simulation of the PC spectra under the same conditions as (a-b) using the Drude model described in the text. (d-f) Experimental data and simulation as in (a-c), but at gate voltage +52 V from the charge neutrality point (electron density $n \approx 3 \times 10^{12}$ cm^{-2}).

We experimentally verified that these artifacts were not present in our data at pump-probe delay $\tau = 1.5$ ps by repeating the same measurement with ZnTe detection crystals of two different thicknesses (1 mm and 100 μm), which have significantly different frequency responses [27]. The results, shown in Fig. 6.4, reveal that the detector response does not influence the result at this time delay. The data shown in Fig. 6.3 were collected using the 1 mm crystal, which has a higher sensitivity and therefore improved signal-to-noise ratio. To determine the influence of the detector response function on the early-time dynamics of the $-\Delta E_\tau/E_0$ measurements, we have performed finite-difference time domain simulations - see §6.3.2 below.

To accurately extract the photoconductivity [Figs. 6.3(b,e)] from our experimental data [Figs. 6.3(a,d)], we used a multilayer model to calculate the transmission of the THz pulse through a graphene device. For a single interface between two dielectrics with

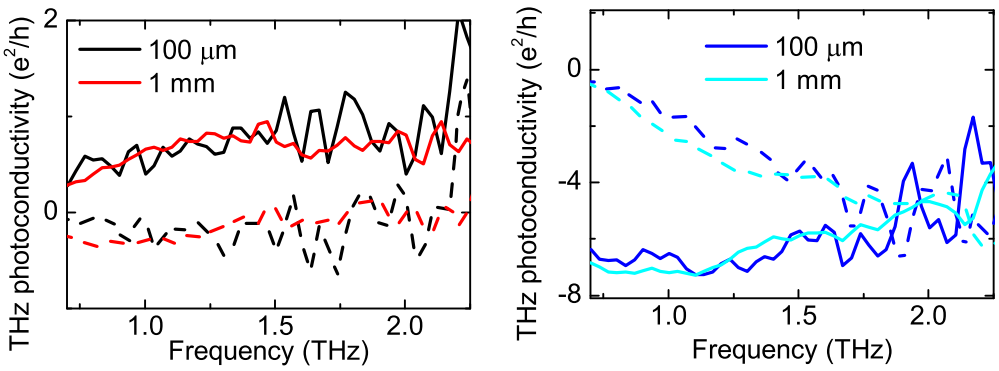

Figure 6.4: Photoconductivity at $\tau = 1.5$ ps for charge neutrality (left panel) and electron-doped regime (right panel) measured using two ZnTe detection crystals with different thicknesses (1 mm and 100 μm) and hence different frequency response functions. Solid lines are real conductivity $\Delta\sigma_1$ and dashed lines are imaginary photoconductivity $\Delta\sigma_2$. There is no discernable difference between the two measurements (aside from the noise), indicating that the detector response function does not distort the photoconductivity spectrum.

indices of refraction n_i and n_j, the reflection and transmission coefficients are given by the Fresnel formulae $\tilde{R}_{ij} = (\tilde{n}_i - \tilde{n}_j)/(\tilde{n}_i + \tilde{n}_j)$ and $\tilde{T}_{ij} = 2\tilde{n}_i/(\tilde{n}_i + \tilde{n}_j)$, respectively. For a dielectric slab with thickness $d \ll \lambda_{\mathrm{THz}}/2n_1$ (*i.e.*, the round-trip time of the pulse in the slab is much less than its duration) on a transparent substrate, multiple reflections within the slab must be taken into account [26]. The total transmission coefficient for the vacuum/dielectric/substrate system is given by [77]

$$\tilde{T} = \tilde{T}_{01}P(n_1, d)\tilde{T}_{12} \times \mathrm{FP} = \frac{4n_2 e^{in_1\omega d/c}}{(1+n_1)(n_1+n_2)}\mathrm{FP}, \tag{6.1}$$

where $n_0 = 1$ for vacuum, n_1 is the index of the dielectric, n_2 is the index of the substrate, $P(n_1, d) = \exp(in_1\omega d/c)$ accounts for propagation through the dielectric slab, and

$$\mathrm{FP} = \frac{1}{1 - \tilde{R}_{12}\tilde{R}_{10}P^2(n_1, d)} = \frac{1}{1 - \left(\frac{n_1-n_2}{n_1+n_2}\right)\left(\frac{n_1-1}{n_1+1}\right)e^{2in_1\omega d/c}}$$

is the Fabry-Perot factor, which accounts for multiple reflections within the slab. We have assumed that n_1 and n_2 are real for dielectric layers.

Our devices have a vacuum/graphene/parylene/ITO/quartz geometry, so we must

consider how the transmission coefficient is changed in this case. To account for the presence of thin graphene and ITO conductors at the interfaces between dielectrics, we change the previous Fresnel coefficients to $\tilde{T}_{i,j} = 2n_i/(n_i + n_j + \tilde{\Sigma}^{(ij)})$ and $\tilde{R}_{i,j} = (n_i - n_j - \tilde{\Sigma}^{(ij)})/(n_i + n_j + \tilde{\Sigma}^{(ij)})$, where $\tilde{\Sigma}^{(ij)} = \tilde{\sigma}^{(ij)} Z_0$ is the dimensionless conductance of the thin conducting layer between dielectrics i and j, with $Z_0 = 2\alpha(h/e^2)$ the impedance of free space [26]. The total transmission coefficient for the multilayer interface is then

$$\begin{aligned}\tilde{T} &= \frac{\tilde{T}_{01} P(n_1, d) \tilde{T}_{12}}{1 - \tilde{R}_{12}\tilde{R}_{10}p_1^2} \\ &= \frac{4n_2 e^{in_1\omega d/c}}{(1 + n_1 + \tilde{\Sigma}^{(01)})(n_1 + n_2 + \tilde{\Sigma}^{(12)})} \frac{1}{1 - \left(\frac{n_1 - n_2 - \tilde{\Sigma}^{(12)}}{n_1 + n_2 + \tilde{\Sigma}^{(12)}}\right)\left(\frac{n_1 - 1 - \tilde{\Sigma}^{(01)}}{n_1 + 1 + \tilde{\Sigma}^{(01)}}\right) e^{2in_1\omega d/c}}. \end{aligned} \tag{6.2}$$

This reduces to Eq. (6.1) when $\tilde{\Sigma} \to 0$. The approximation of infinitely thin conductors is justified in our devices because $d_{\text{graphene}} = 0.3$ nm $\ll d_{\text{ITO}} = 35$ nm $\ll d_{\text{parylene}} = 400$ nm $\ll \lambda_{\text{THz}} = 300$ μm.

To calculate the THz photoconductivity of a conductor between vacuum and a dielectric in a pump-probe experiment, assuming all other optical properties remain constant (Fig. 6.2), we write the differential transmission in terms of the conductivity of the layer before and after excitation (as in §3.2.1):

$$\frac{\Delta\tilde{T}_\tau}{\tilde{T}_0} = \frac{\tilde{T}_\tau(\tilde{\sigma}^{(01)} + \Delta\tilde{\sigma}_\tau^{(01)})}{\tilde{T}_0(\tilde{\sigma}^{(01)})} - 1,$$

then solve the resulting expression for $\Delta\tilde{\sigma}_\tau^{(01)}$. The result to first order in $\Delta\tilde{\sigma}_\tau^{(01)}$ and $\Delta\tilde{T}/\tilde{T}_0$ is

$$\Delta\tilde{\sigma}_\tau^{(01)} = -Z_0^{-1}\left(\frac{\Delta\tilde{T}}{\tilde{T}_0}\right)\frac{\mathcal{N}}{\mathcal{D}}, \tag{6.3}$$

where $\mathcal{N} = \left[(1 + n_1 + \tilde{\Sigma}^{(01)})(n_1 + n_2 + \tilde{\Sigma}^{(12)}) - (n_1 - n_2 - \tilde{\Sigma}^{(12)})(n_1 - 1 - \tilde{\Sigma}^{(01)})e^{2in_1\omega d/c}\right]$ and $\mathcal{D} = \left[(n_1 + n_2 + \tilde{\Sigma}^{(12)}) + (n_1 - n_2 - \tilde{\Sigma}^{(12)})e^{2in_1\omega d/c}\right]$.

For our graphene devices, $n_1 = n_{\text{parylene}} = 1.7$ (Ref. [127]), $n_2 = n_{\text{quartz}} = 2.1$ (Ref. [87]), $\tilde{\Sigma}^{(01)} = \tilde{\Sigma}_{\text{graphene}}$, $\tilde{\Sigma}^{(12)} = \Sigma_{\text{ITO}}$, and $d = 400$ nm. The measured sheet resistance

of the ITO film is constant in the THz frequency range and equal to 500 $\Omega/\square$, so $\tilde{\Sigma}^{(12)} = 377/500 = 0.75$. We approximated $\tilde{\Sigma}_{\text{graphene}}$ by a Drude term with scattering rate based on the temperature- and density-dependence discussed in the description of our model below. The Drude weight was set by the temperature and carrier density calculated using the capacitance of our device. We note that this model for $\tilde{\Sigma}_{\text{graphene}}$ was used for internal consistency, but any reasonable values for $\tilde{\Sigma}_{\text{graphene}}$ produce similar results and do not change our conclusions. Finally, we note that since the thickness of the parylene layer is much smaller than the wavelength of the THz pulse, $2n_{\text{parylene}}\omega d/c \approx 0.02$ and uncertainty in the value of n_{parylene} does not qualitatively affect the results.

To further investigate the mechanism driving the observed PC sign change, we measured the temporal (τ) dynamics of $\Delta\sigma_{\tau,1}$ at various carrier densities. Fig. 6.5(a) displays the ratio $-\Delta E_\tau(t)/E_0(t)$ as a function of τ at fixed $t = 0$ [Figs. 6.3(a,d)] for gate voltages between -48 V and +2 V from V_{CN} (incident fluence $\mathcal{F} = 10$ μJ/cm^2). The dynamics exhibits a relaxation time of $\sim$2 ps, with no systematic dependence on carrier density. From these dynamical data, we evaluated the differential field averaged over τ, $\langle -\Delta E_\tau/E_0 \rangle_\tau$, as a function of gate voltage [Fig. 6.5(c)]. The result demonstrates that the overall PC signal changes from positive at charge neutrality to negative at moderate charge density for both electron and hole sides, consistent with dc measurements [23].

Additional data for $\mathcal{F} = 3$ μJ/cm^2 are presented in Fig. 6.6. This figure shows our measurements and simulations of $-\Delta E_\tau/E_0$ and $\langle -\Delta E_\tau/E_0 \rangle_\tau$ using a lower incident fluence ($\mathcal{F} = 3$ μJ/cm^2) than in Fig. 6.5. The inset of Fig. 6.6(b) shows the estimated temperature profile corresponding to this fluence. The simulation, performed using the same parameters used to generate Figs. 6.5(b,d) with $\mathcal{F} = 10$ μJ/cm^2, also faithfully reproduces our observations for $\mathcal{F} = 3$ μJ/cm^2 [Fig. 6.6(b,d)].

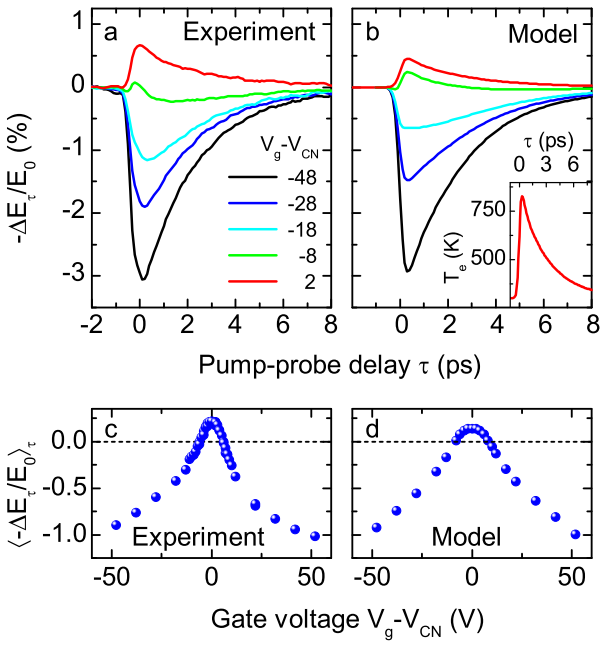

Figure 6.5: (a) Measured temporal evolution of the negative change in transmitted field (proportional to the differential conductivity), measured at the peak of the signal in Figs. 6.3(a,d), at different gate voltages. Measurements were performed at room temperature in vacuum with incident fluence $\mathcal{F} = 10$ μJ/cm^2. (b) Theoretical simulation of the THz dynamics in (a), calculated using the model described in the text. Inset shows the estimated temperature profile used to model the data. (c) Mean of $-\Delta E(t=0)_\tau / E_0(t=0)$ from $\tau =$ -1 ps to 8 ps, as a function of gate voltage. (d) Simulation of the data in (c).

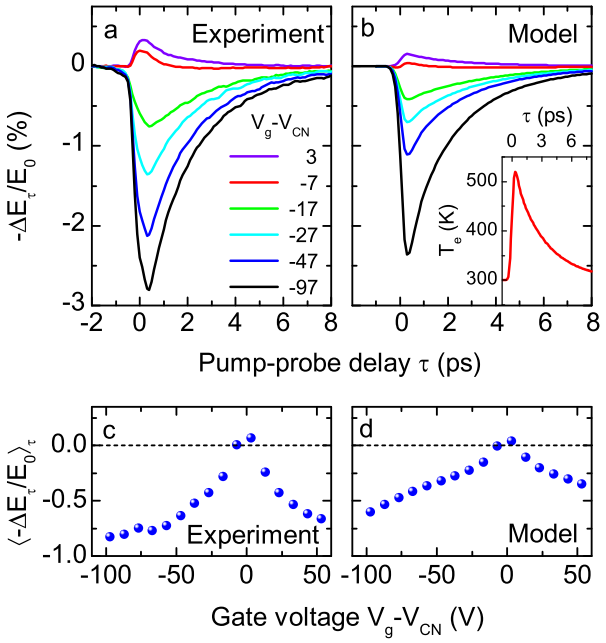

Figure 6.6: (a) Measured temporal evolution of the negative change in transmitted field (proportional to the differential conductivity), measured at the peak of the signal in Figs. 6.3(a,d), at different gate voltages. Measurements were performed at room temperature in vacuum with incident fluence $\mathcal{F} = 3$ μJ/cm^2. (b) Theoretical simulation of the THz dynamics in (a), calculated using the model described in the text. Inset shows the estimated temperature profile used to model the data. (c) Mean of $-\Delta E(t=0)_\tau/E_0(t=0)$ from $\tau =$ -1 ps to 8 ps, as a function of gate voltage. (d) Simulation of the data in (c).

6.2.2 Discussion and analysis

The above observations can be qualitatively understood by considering the interplay between photo-induced changes of carrier population and scattering rate. Photoexcited carriers in graphene are known to thermalize within a few 10s of fs [44, 128–131]. With the >100 fs resolution in our experiment, the carriers can be well described by a thermal distribution at carrier temperature T_e for all pump-probe delay times τ. For graphene near the charge neutrality point, an increase of carrier temperature promotes the free-carrier population and thus enhances absorption. This behavior mimics that observed in epitaxial graphene [107, 108] and other semiconductors [24, 79], where optically generated electron-hole pairs increase the infrared absorption. For graphene with high carrier density, laser-induced carrier heating only modifies the carrier distribution near the Fermi level, without changing the total carrier density. The carrier scattering rate, however, increases due to an enlarged phase space and the presence of hot optical phonons [48]. This causes a reduction of free-carrier absorption, a behavior analogous to that in metals and observed in p-doped CVD graphene [61, 85, 86, 117].

For a more thorough understanding of the density dependent PC dynamics, we consider the Drude model for free carrier conductivity in graphene [11, 61, 65, 85, 108],

$$\tilde{\sigma}(\omega) = \frac{D}{\pi(\Gamma - i\omega)}. \tag{6.4}$$

Here, Γ is the transport scattering rate and D is the Drude weight, which quantifies the oscillator strength of free-carrier absorption. In a metal or semiconductor with parabolic dispersion, $D = \pi n e^2/m$, independent of temperature [29]. In graphene, a 2D system with linear dispersion, however, D exhibits a distinctive carrier temperature dependence [65, 132, 133]:

$$D(T_e) = \frac{2e^2}{\hbar^2} k_B T_e \ln\left[2\cosh\left(\frac{\mu(T_e)}{2k_B T_e}\right)\right]. \tag{6.5}$$

Here we present a simple derivation of this formula. To highlight the peculiarity of graphene, we calculate the Drude weight $D = \pi\sigma_{\rm dc}/\tau$ for general quasiparticle dispersion $\varepsilon = \mathcal{A}|\boldsymbol{k}|^\alpha$ in arbitrary dimension d. From the Boltzmann expression for dc conductivity,

$$\sigma_{\rm dc} = Ne^2 \int \frac{d^dk}{d(2\pi)^d} v^2(\boldsymbol{k})\tau(\varepsilon(\boldsymbol{k})) \left(-\frac{\partial f^0}{\partial\varepsilon}\right), \tag{6.6}$$

where N is the degeneracy, $\boldsymbol{v}(\boldsymbol{k}) = \hbar^{-1}\partial\varepsilon/\partial\boldsymbol{k} = (\alpha\mathcal{A}/\hbar)k^{\alpha-1}\hat{\boldsymbol{k}}$, τ is the transport scattering time, f^0 is the Fermi distribution, and we have considered an isotropic system so that $\left\langle v^\alpha(\boldsymbol{k})v^\beta(\boldsymbol{k})\right\rangle = v(\boldsymbol{k})^2/d$. Assuming $\tau = \tau_0 =$ constant for simplicity,

$$\begin{aligned}\sigma_{\rm dc} &= \frac{\alpha^2\mathcal{A}^2}{\hbar^2}\frac{Ne^2\tau_0}{d}\int\frac{d^dk}{(2\pi)^d}k^{2\alpha-2}\left(-\frac{\partial f^0}{\partial\varepsilon}\right)\\ &= \frac{\alpha^2\mathcal{A}^2}{\hbar^2}\frac{e^2\tau_0}{d}\int d\varepsilon g(\varepsilon)k^{2\alpha-2}\left(-\frac{\partial f^0}{\partial\varepsilon}\right)\end{aligned} \tag{6.7}$$

where the density of states is $g(\varepsilon) = N\int\frac{d^dk}{(2\pi)^d}\delta(\varepsilon-\varepsilon(\boldsymbol{k})) = \gamma\varepsilon^{d/\alpha-1}$. Inverting the energy-momentum dispersion, we obtain $k = (\varepsilon/\mathcal{A})^{(1/\alpha)}$ so

$$\begin{aligned}\sigma_{\rm dc} &= \frac{\alpha^2\mathcal{A}^2}{\hbar^2}\frac{e^2\tau_0}{d}\int d\varepsilon g(\varepsilon)(\varepsilon/\mathcal{A})^{2-2/\alpha}\left(-\frac{\partial f^0}{\partial\varepsilon}\right)\\ &= \frac{\alpha^2\mathcal{A}^{2/\alpha}}{\hbar^2}\frac{e^2\tau_0}{d}\int d\varepsilon f^0(\varepsilon)\frac{\partial}{\partial\varepsilon}\left[\varepsilon^{2-2/\alpha}g(\varepsilon)\right]\\ &= \gamma\frac{\alpha^2\mathcal{A}^{2/\alpha}}{\hbar^2}\frac{e^2\tau_0}{d}\int d\varepsilon f^0(\varepsilon)\frac{\partial}{\partial\varepsilon}\left[\varepsilon^{1+(d-2)/\alpha}\right]\\ &= \frac{\alpha^2\mathcal{A}^{2/\alpha}}{\hbar^2}\frac{e^2\tau_0}{d}\left(1+\frac{d-2}{\alpha}\right)\int d\varepsilon f^0(\varepsilon)\left[\gamma\varepsilon^{(d-2)/\alpha}\right]\end{aligned} \tag{6.8}$$

If $\alpha = 2$ (parabolic dispersion), the integrand is just the occupation probability $f^0(\varepsilon)$ times the density of states, so the integral gives the total number of carriers. The Drude weight is therefore independent of temperature.

If $\alpha = 1$, however, this is not the case. Inserting $\varepsilon = \hbar v_{\rm F}k$ and $g(\varepsilon) = 2|\varepsilon|/\pi(\hbar v_{\rm F})^2$

(*i.e.*, $\mathcal{A} = \hbar v_{\rm F}$ and $\gamma = 2/\pi(\hbar v_{\rm F})^2$) into Eq. (6.7), we obtain

$$\begin{aligned}\sigma_{\rm dc} &= \frac{e^2 v_{\rm F}^2 \tau_0}{d} \int g(\varepsilon) \left(-\frac{\partial f^0}{\partial \varepsilon}\right) d\varepsilon \\ &= \frac{N\Omega_d}{d(2\pi)^d} \frac{e^2\tau_0}{k_{\rm B}T_{\rm e}\hbar^d v_{\rm F}^{d-2}} \int g(\varepsilon) f^0(\varepsilon)\left[1 - f^0(\varepsilon)\right] d\varepsilon \\ &= \frac{N\Omega_d}{d(2\pi)^d} \frac{e^2\tau_0}{\hbar^d v_{\rm F}^{d-2}} (k_{\rm B}T_{\rm e})^{d-1} \int_{-\infty}^{\infty} |x|^{d-1} \frac{e^{x-x_\mu}}{(e^{x-x_\mu}+1)^2} dx, \end{aligned} \tag{6.9}$$

where $x_\mu = \mu(T_{\rm e})/k_{\rm B}T_{\rm e}$ and $(-\partial f^0/\partial\varepsilon) = f^0(\varepsilon)[1 - f^0(\varepsilon)]/k_{\rm B}T_{\rm e}$. The integral can be easily evaluated to obtain

$$\begin{aligned} D(T_{\rm e}) &= \frac{Ne^2 v_{\rm F}}{\hbar} && (d=1) \\ &= \frac{Ne^2}{2\hbar^2} k_{\rm B}T_{\rm e} \ln\left[2\cosh\left(\frac{\mu(T_{\rm e})}{2k_{\rm B}T_{\rm e}}\right)\right] && (d=2) \\ &= \frac{Ne^2}{6\pi\hbar^3 v_{\rm F}} (k_{\rm B}T_{\rm e})^2 \left[\frac{\pi^2}{3} + \left(\frac{\mu(T_{\rm e})}{k_{\rm B}T_{\rm e}}\right)^2\right]. && (d=3) \end{aligned} \tag{6.10}$$

In our experiment, photoexcitation resulted in hot carrier temperatures close to the Fermi energy, $k_{\rm B}T_{\rm e} \sim \varepsilon_{\rm F}$. In this regime, the chemical potential is a decreasing function of temperature. The chemical potential shift can be calculated by considering the conservation of the total particle number in the system [29, 53]

$$n = \int_0^\infty g(\varepsilon) \left(\frac{1}{e^{[(\varepsilon-\mu)/k_{\rm B}T_{\rm e}]}+1} - \frac{1}{e^{[(\varepsilon+\mu)/k_{\rm B}T_{\rm e}]}+1}\right) d\varepsilon. \tag{6.11}$$

The temperature-dependent chemical potential is obtained by numerically inverting this relation. Fig. 6.7 displays the chemical potential of charge carriers in graphene as a function of temperature, along with the analytical results of the low-temperature Sommerfeld approximation for low temperatures [29] and the high-temperature limit of Eq. (6.11) (Ref. [53]). Using $\mu(T_{\rm e})$ derived from Eq. (6.11), we obtain the temperature-dependence of the Drude weight shown in Fig. 2.5 of §2.2.1. The Drude weight for linear dispersing systems in 2D or 3D depends on $\mu(T_{\rm e})$ (instead of n as in systems with parabolic dispersion), resulting in non-monotonic temperature dependence.

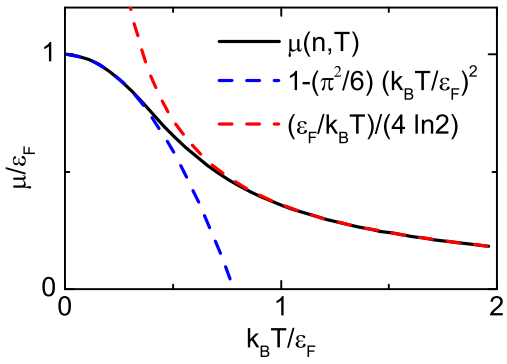

Figure 6.7: Temperature-dependent chemical potential (black line) in graphene calculated by numerically inverting Eq. (6.11). The blue dashed line shows the low-temperature Sommerfeld approximation and the red dashed line shows the analytical high-temperature limit, $\varepsilon_{\rm F}/[4\ln(2)k_{\rm B}T]$.

Expression (6.5) predicts that, in pristine graphene, $D(T_{\rm e})$ increases linearly with temperature when $k_{\rm B}T_{\rm e} \gg \varepsilon_{\rm F}$, and approaches $(e^2/\hbar^2)\mu \propto \sqrt{|n|}$ for electronic temperatures $k_{\rm B}T_{\rm e} \ll \varepsilon_{\rm F}$. For graphene samples on substrates, charge inhomogeneity and disorder smear out intrinsic behavior near the Dirac point [54]. We included these effects by using a phenomenologically broadened chemical potential $\mu \to \sqrt[4]{\mu^4 + \Delta^4}$, with $\Delta = 80$ meV, a reasonable value for our samples [134]. Here Δ^2 is proportional the RMS charge density inhomogeneity. We estimated an upper bound, $\Delta = 110$ meV, by fitting the resistance data of Fig. 6.1 following the procedure outlined in Ref. [134]. A lower bound was estimated by the value of gate voltage at the charge neutrality point, $V_{\rm g} = 3$ V, which corresponds to $p \approx 1.7 \times 10^{11}$ cm^{-2}, or $\Delta \approx 50$ meV. For our simulations, we used the average value $\Delta = 80$ meV. Other choices of Δ within the estimated range yielded qualitatively similar results.

The other parameter in the Drude model, the scattering rate Γ, depends on chemical potential μ, carrier temperature $T_{\rm e}$, phonon temperature $T_{\rm ph}$, and the specific scattering mechanisms [34, 135, 136]. In our samples, we expect charged impurities and hot optical phonons to dominate scattering [34, 36, 48]. We assumed that Γ at room temperature was dominated by Coulomb impurities [52, 54], with a transport scattering time $\tau = \alpha|\mu|$

(Refs. [54,86,137]). We estimated $\alpha = 2.75\times10^{-4}$ meV^{-2} from the scattering rate $\Gamma = 12.14$ meV ($\approx$3 THz) measured in the CVD graphene sample on quartz substrate with chemical potential $\mu = 300$ meV due to unintentional doping, described in chapter 5 [61]. We also included the temperature-dependent scattering due to the graphene optical phonons, using the T and μ dependence reported in Ref. [36], with the magnitude adjusted to match the experimental data. The total scattering rate including both contributions is given in meV by

$$\Gamma(T_{\rm e}, T_{\rm ph}) = \Gamma_{\rm C} + \Gamma_{\rm op} = \left(\frac{3642}{\mu[\text{meV}]} + \frac{0.7\mu[\text{meV}]}{e^{\hbar\omega_{\rm ph}/k_{\rm B}T_{\rm e}} - 1}\right) \times \text{meV}, \tag{6.12}$$

with $\hbar\omega_{\rm ph} = 190$ meV [36]. We neglected the unknown coupling of carriers to surface polar phonons in the parylene-C dielectric [23, 135].

We used $D(T_{\rm e})$ and $\Gamma(T_{\rm e}, T_{\rm ph})$ as estimated above to calculate the temperature- and density-dependent change in conductivity for our experimental conditions, $\Delta\sigma_1(T_{\rm e}) = \sigma_1(T_{\rm e}) - \sigma_1(300\text{ K})$, at representative frequency $\omega/2\pi = 1$ THz. The result [Fig. 6.8(c)] shows that $\Delta\sigma_1(T_{\rm e})$ is positive (red area) near charge neutrality ($V_{\rm g} < 5$ V), but becomes negative (blue area) at high carrier density ($V_{\rm g} > 15$ V), as anticipated from the qualitative discussion above.

To simulate the transient PC dynamics, we also considered the temporal (τ) evolution of the carrier temperature after photoexcitation. Such hot carrier dynamics have been discussed extensively in the literature. We therefore estimated the transient temperature profile from previous publications [44, 48, 138] and simulated the temporal PC dynamics. In particular, we assumed a biexponential decay with time constants $\tau_1 = 0.3$ ps and $\tau_2 = 3.1$ ps and a 200 fs rise time [Refs. [48,138]; see inset of Figs. 6.5(b) and 6.6(b)]. The fast time constant τ_1 accounts for thermalization and initial electron-optical phonon equilibration [138], while the slow time constant τ_2 accounts for cooling of the hot electrons [48, 138]. Since the actual carrier and phonon temperatures are inaccessible to our experimental probes, we as-

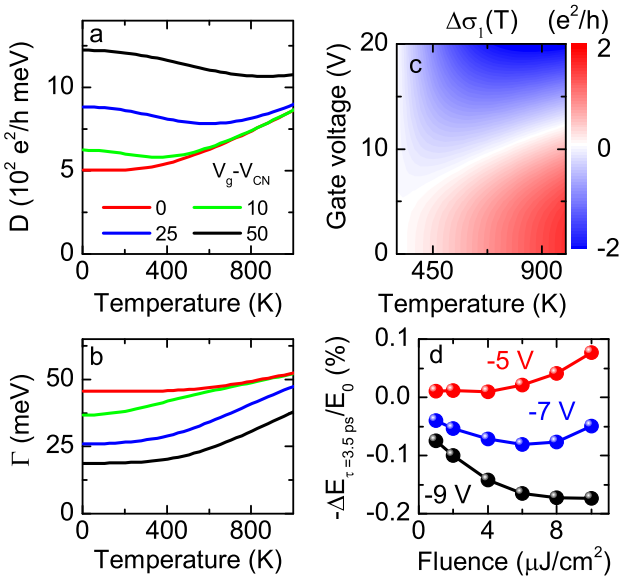

Figure 6.8: (a) Temperature-dependent Drude weight [Eq. (6.5)] at different gate voltages. Saturation at low temperature is due to charge disorder. (b) Estimated temperature dependence of the scattering rate at different gate voltages. (c) Calculated change in conductivity $\Delta\sigma_1(T)$ at $\omega/2\pi = 1$ THz, for different carrier densities and temperatures, relative to its value at $T = 300$ K. Temperature dependence of both Drude weight and scattering rate were taken into account. (d) Fluence dependence of PC at fixed pump-probe delay $\tau = 3.5$ ps showing the non-monotonic behavior expected from our model.

sumed that they were equal for simplicity [33, 44, 48]. The maximum estimated temperature was ∼800 K for 10 μJ/cm^2 incident fluence and ∼500 K for 3 μJ/cm^2 incident fluence. The magnitude of the temperature change was chosen to match the measured data for incident fluence $\mathcal{F} = 3$ μJ/cm^2. We constrained the temperature value between that calculated using the two-temperature model of Ref. [44] and the maximum value for which all deposited laser energy was retained in the electronic system. To estimate the temperature at other incident fluences, we assumed a specific heat proportional to T_e. Plots of $T_e(\tau)$ for two fluences, $\mathcal{F} = 3$ μJ/cm^2 and 10 μJ/cm^2, are shown in the insets of Figs. 6.5(b) and 6.6(b).

Based on this temperature profile, we calculated $\Delta\tilde{\sigma}_\tau(\omega)$ [Figs. 6.3(c,f)] and $-\Delta E_\tau/E_0$ [Figs. 6.5(b,d) and 6.6(b,d)]. First, we Fourier transformed an experimental THz time-domain waveform. Second, we multiplied the resulting frequency-domain spectrum by the Fresnel coefficient for our device geometry [Eq. (6.2)], using the conductivity calculated from our Drude model. Third, we inverse Fourier transformed to obtain the time-domain waveform at elevated temperature. Finally, we subtracted the original time-domain waveform at room temperature to obtain the differential change of THz field for a direct comparison with the experimental pump-probe signal. Our simulations, though based on a simple model, were found to reproduce all the main features of our observations.

6.3 Non-monotonic temperature dependence of the Drude weight

6.3.1 Experimental results

An essential aspect of our model is the distinctive Drude weight of graphene with non-monotonic temperature dependence [Eq. (6.5) and Fig. 6.8(a)]. Specifically, for finite density, $D(T_e)$ first decreases to a minimum value as T_e increases, then increases linearly with T_e for temperatures much greater than ε_F (Fig. 6.8(a); Refs. [132, 133]). In order to reveal

this unique Drude behavior of graphene more directly, we examined the fluence dependence of $-\Delta E_\tau/E_0$ in the PC crossover regime [Fig. 6.8(d)]. Since T_e increases monotonically with excitation fluence [44, 48], any non-monotonicity of $D(T_e)$ should also manifest in its fluence dependence. This phenomenon is indeed observed in our experimental data [Fig. 6.8(d)]. At a representative τ = 3.5 ps near the PC crossover (V_g = -7 V), $-\Delta E_{3.5\,ps}/E_0$ is found to first decrease and then increase with increasing fluence. This non-monotonic behavior gradually weakens as the density moved away from the crossover [see, *e.g.*, V_g = -5 V and -9 V in Fig. 6.8(d)]. This peculiar fluence dependence is observed for all τ = 1 - 8 ps.

We also observed independent evidence for the non-monotonic $D(T_e)$ in the temporal PC dynamics at the crossover, where the PC sign flips multiple times as the carriers are heated up by the pump pulse and subsequently cool. Fig. 6.9 shows the temporal dynamics of the gate- and fluence-dependent transient photoconductivity near the crossover between positive and negative photoconductivity, which further reveal the non-monotonic temperature-dependence of the Drude weight in graphene. We measured $-\Delta E_\tau/E_0$ at three gate voltages (top panels) with incident fluence $\mathcal{F}$ = 1, 2, 4, 6, 8, 10 $\mu J/cm^2$ [magenta (1 $\mu J/cm^2$) to black (10 $\mu J/cm^2$); each curve is offset by 0.2 for clarity of presentation]. The complicated temporal dynamics, characterized by multiple sign changes on a picosecond timescale, are consistent with our model (bottom panels) including the non-monotonic temperature dependence of the Drude weight. As shown in Fig. 6.8(c), $\Delta\sigma_1(T_e)$ at intermediate carrier density is initially negative, then becomes positive as temperature increases. In our pump-probe experiment, the optical pump pulse initially heated the carriers to high temperature, resulting in a rapid sign change of $\Delta\sigma_{\tau,1}$ from negative to positive. As the carriers then cooled, $\Delta\sigma_{\tau,1}$ changed sign to negative again before returning to zero at equilibrium. Our observed temporal photoconductivity dynamics (Fig. 6.9, top panels) also follow this sequence of sign changes, suggesting the importance of the non-monotonic temperature-

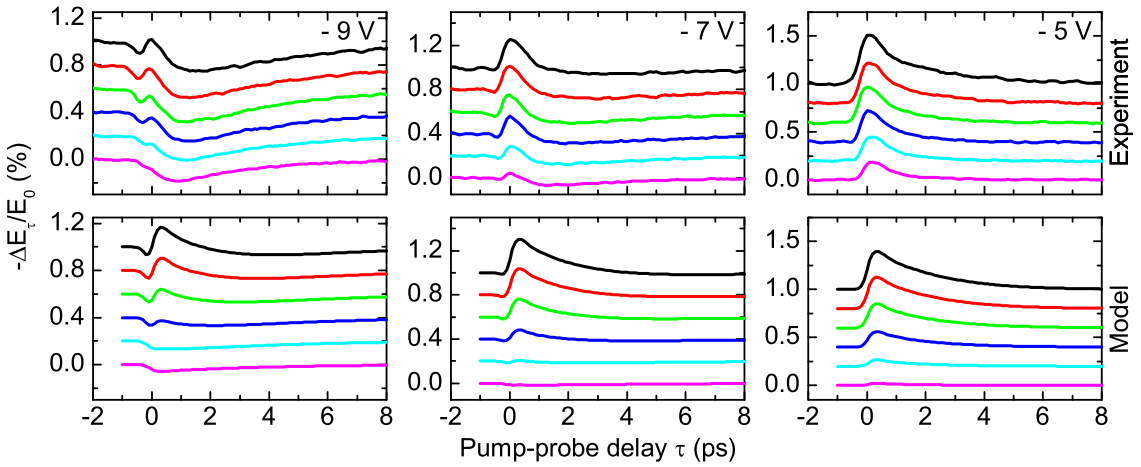

Figure 6.9: Measurement (top panels) and simulation (bottom panels) of $-\Delta E_\tau/E_0$ near the crossover between positive and negative photoconductivity, at different fluences (1, 2, 4, 6, 8, 10 μJ/cm^2, bottom to top). Curves are offset by 0.2 for clarity of presentation.

dependence of the Drude weight in graphene. Using the same parameters as before, our model reproduces this behavior (Fig. 6.9, bottom panels). We note that these temporal dynamics do not appear in our simulation if we neglect the non-monotonic temperature dependence of $D(T_\mathrm{e})$.

To further illustrate the important role of the decrease of chemical potential as the temperature rises, we performed the same simulation, but with a constant chemical potential $\mu = \varepsilon_\mathrm{F}$. The results are presented in Fig. 6.10. This model predicts that the photoconductivity should first be positive, then become negative as temperature increases (dashed line). This behavior is qualitatively different from that seen in Fig. 6.8(c), as well as from the experimental observations.

6.3.2 Additional analysis and discussion

We also carried out finite-difference time-domain (FDTD) simulations to further compare our experimental observations to our model [79, 91, 92]. For computational efficiency, we

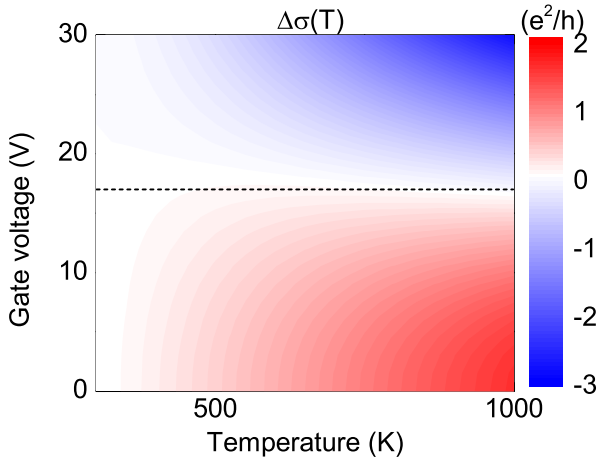

Figure 6.10: $\Delta\sigma(T)$ calculated using $\mu = \varepsilon_{\mathrm{F}}$ in Eq. (6.5) . The observed dependence on V_{g} and T is qualitatively different from that found in Fig. 6.8(c) and does not reproduce the experimental observations.

modeled our graphene sample as a suspended conducting film of thickness 2.5 μm discretized into 25 grid points of thickness $\Delta z = 0.1$ μm. This thickness was found to satisfy the thin-film limit (thickness $d \ll$ wavelength λ) for our experiment, yet still be large enough to allow reasonable computation times. The total conductance of the film was chosen to match that of our graphene sample. The time step was chosen to be $\Delta t = \Delta z/2c$, satisfying the Courant stability relation. The incident electromagnetic pulse was introduced using the total-field/scattered-field method. We used our measured THz pulse, deconvolved from the detector response, to set the spectrum of the incident electromagnetic wave. To model the dispersive conductivity of our graphene sample, we used the auxiliary differential equation method [92], allowing the Drude weight D and scattering rate Γ to vary as a function of time to simulate the pump-probe experiment. We performed the FDTD simulation at various pump-probe delays, then convolved with our detector response and projected the resulting grid onto the $t - \tau$ axis to simulate our measured signal.

We compare two representative simulation results, calculated at the crossover

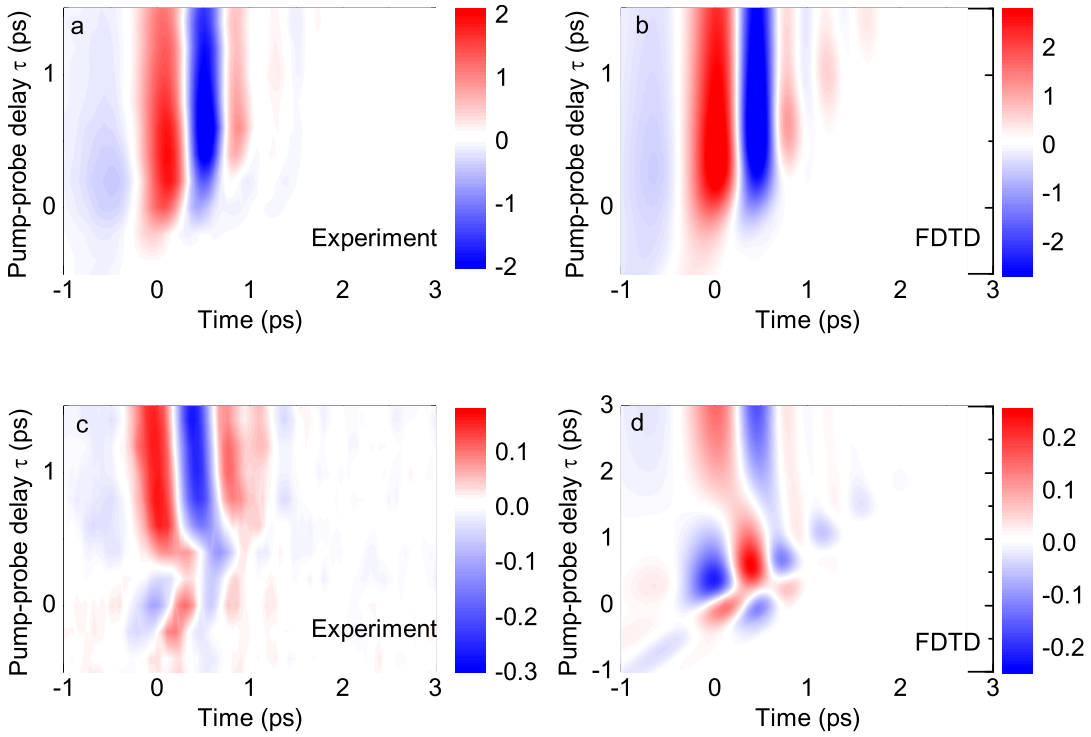

Figure 6.11: FDTD simulations of experimental results. Top row shows experimental measurement of $-\Delta E(t)_\tau / E_0(t=0)$ (left panel) and FDTD simulation (right panel) for graphene with high charge density, where the photoconductivity does not change sign. Bottom row shows experiment (left) and simulation (right) for graphene at moderate charge density, where our model predicts sign changes in the temporal photoconductivity dynamics.

regime and in the metallic photoconductivity regime, to our experiment in Fig. 6.11. Our simulations capture the main features of the experimental data. The experiment and FDTD simulation for a charge density near the crossover [panels (c,d)], where we observe multiple sign changes in the $-\Delta E(t=0)_\tau/E_0(t=0)$ traces [Fig. 6.9] (which correspond to a vertical line cut along the $t=0$ axis of the color maps in Fig. 6.11), show good qualitative agreement. This provides strong evidence that the measured THz temporal dynamics reflect the underlying graphene carrier dynamics, even when experimental complications which can distort the time-domain measurements are taken into account.

The observed non-monotonic temperature dependence of the Drude weight can be understood intuitively by considering the conservation of spectral weight of optical transitions [11, 65, 72]. Optical absorption in graphene consists of two contributions: high-energy interband absorption and low-energy intraband absorption. Interband absorption in graphene with finite charge density shows an onset at photon energy $\hbar\omega = 2|\mu|$ due to Pauli blocking [11, 64, 65]. When carriers are heated to moderate temperatures $k_\mathrm{B}T_\mathrm{e} \ll \varepsilon_\mathrm{F}$, $\mu(T_\mathrm{e})$ decreases due to particle conservation [29]. The corresponding decrease of onset energy for interband absorption increases the interband spectral weight. To conserve total spectral weight, the intraband absorption must decrease. This is depicted in Fig. 6.12. When carrier temperatures become comparable to ε_F, however, interband transitions are Pauli blocked by thermally excited carriers, reducing the spectral weight. This increases the intraband spectral weight, as has been observed in graphite [72]. This unique behavior originates from the distinctive linear dispersion of 2D massless Dirac fermions in graphene, and is absent in conventional materials with parabolic dispersion.

In conclusion, we studied the temperature- and density-dependent Drude conductivity in graphene through its dynamical response to pulsed photoexcitation. We demonstrated that the transient photoconductivity of graphene can be tuned continuously from

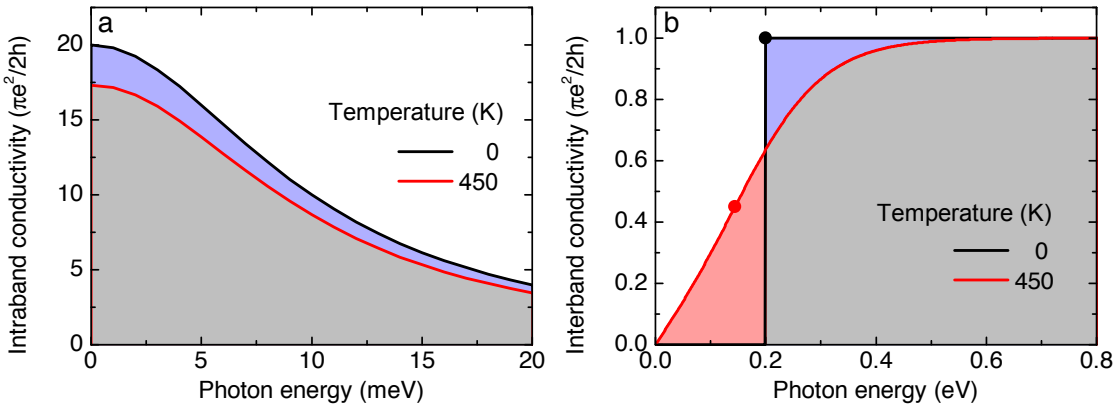

Figure 6.12: Conservation of spectral weight in graphene. (a) Intraband (Drude) conductivity with fixed scattering rate at $T_e = 0$ K and 450 K. The blue shaded area shows the decrease in spectral weight upon increasing temperature. (b) Interband conductivity at $T_e = 0$ K and 450 K. Solid dots denote the onset of interband absorption at $\hbar\omega = 2|\mu|$. The area of the red shaded area is larger than the area of the blue shaded area, corresponding to an increase in interband spectral weight. The difference between the red and blue areas in (b) is precisely equal to the blue area in panel (a).

semiconducting to metallic by varying the Fermi level from the charge neutrality point to either the electron or hole side. Our results resolve the controversy between previous experiments which observed positive photoconductivity in epitaxial graphene and negative photoconductivity in CVD graphene. By detailed simulation based on the Drude model, we found that photo-induced changes of both Drude weight and carrier scattering rate play important roles in the THz photoconductivity dynamics.

Appendix A

Application of TRTS to a high T_c superconductor

In addition to the work presented in the main text of this dissertation, I also performed studies of the high temperature cuprate superconductor $La_{2-x}Sr_xCuO_4$. Copper-based superconductors were first discovered nearly thirty years ago, and their understanding still poses a formidable challenge to condensed matter physicists [139].

Time-domain terahertz spectroscopy is ideally suited for measuring electronic properties of superconductors and has been used extensively to study the cuprates [82, 83, 140–150]. These measurements have a typical energy range of 1-10 meV and therefore only access sub-gap phenomena in cuprates, where the energy gap is typically a few 10s of meV [151]. TDTS and TRTS have previously been used to observe many fascinating phenomena, including superconducting phase fluctuations in $Bi_2Sr_2Ca_2CuO_{8+\delta}$ [152] and $La_{2-x}Sr_xCuO_4$ [147], pair-wise recombination of optically excited quasiparticles in $Bi_2Sr_2Ca_2CuO_{8+\delta}$ [83], and the destruction of the superconducting state via optical excitation in $La_{2-x}Sr_xCuO_4$ [146].

We begin by discussing low energy electrodynamics in cuprates. We focus on energy scales below twice the maximum superconducting gap energy, which is ∼20-30 meV in optimally doped $La_{2-x}Sr_xCuO_4$ [153]. Below the superconducting transition temperature

T_c, the electrodynamic response at these energies can be described by the two-fluid model, in which the optical conductivity arises due to interaction of light with both paired and unpaired quasiparticles [154],

$$\tilde{\sigma}(\omega) = \frac{\rho_n(T)}{\Gamma(T) - i\omega} + \rho_s(T)\left(\frac{\pi}{2}\delta(\omega) + \frac{i}{\omega}\right). \tag{A.1}$$

The first term is the familiar Drude response, which in a superconductor is due to unpaired electrons. Here $\rho_n(T) = n_n(T)e^2/m^*$ is termed the normal fluid density. The second term is the superfluid response, which takes the form of a δ-function at zero frequency in the real part and a $1/\omega$ term in the imaginary part. The δ-function reflects the absence of dc electrical resistance of a superconductor, and the $1/\omega$ imaginary conductivity is required by the Kramers-Kronig relations. Notably, the prefactor of the $1/\omega$ term in the imaginary conductivity is precisely $\rho_s(T)$, the superfluid density: $\sigma_2(\omega) \propto \rho_s(T)$. As electrons pair, the superfluid contribution to the imaginary part of the conductivity grows dramatically at low frequencies due to the $1/\omega$ term, while the normal fluid contribution, which is already small at low energies, decreases. Therefore, by measuring the imaginary conductivity in the superconducting state at low frequency, one has direct access to the evolution of the superfluid density with temperature or external perturbation.

Our sample was a thin film of $La_{2-x}Sr_xCuO_4$ with $x = 0.16$ (optimal doping), grown by molecular beam epitaxy on a 1 mm thick $LaSrAlO_4$ substrate [155,156]. The film thickness was $\ell = 52$ nm, and it had a superconducting transition temperature $T_c = 41$ K. The measured optical conductivity of the sample at various temperatures is displayed in Fig. A.1. The real conductivity (left panel) initially increases as temperature decreases, reflecting a decrease in quasiparticle scattering rate $\Gamma(T)$ [140]. It reaches its maximum at $T_c = 41$ K, then begins decreasing as spectral weight is transferred to the zero frequency δ-function according to the Ferrell-Glover-Tinkham sum rule [154]. As expected, the $1/\omega$ response in

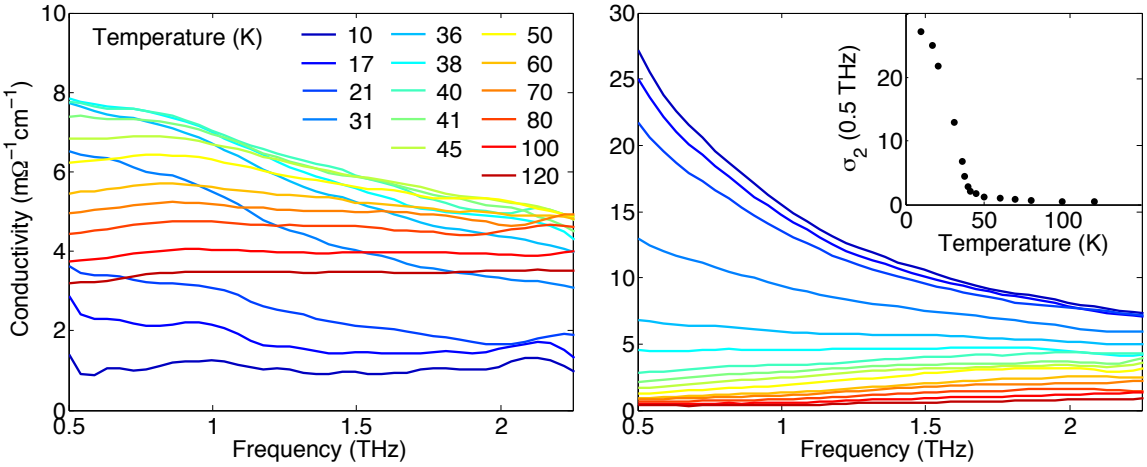

Figure A.1: Real (left) and imaginary (right) conductivity of optimally doped $La_{2-x}Sr_xCuO_4$ ($x = 0.16$). The low frequency imaginary conductivity grows rapidly below T_c (right inset) due to the increasing superfluid density.

$\sigma_2(\omega)$ rises dramatically below T_c (right panel). The inset of the right panel shows the value of the imaginary conductivity at 500 GHz as a function of temperature to emphasize the rapid increase below T_c, which is due to increasing superfluid density. A detailed analysis of similar data over a wide range of dopings is discussed in Ref. [147]. These data allow one to infer properties of the superconducting state by observing how it is perturbed as temperature is raised. We will next seek to determine what we can learn by perturbing the superconducting state with an optical excitation.

To measure the change in conductivity after photoexcitation in a simple manner, we exploited the phase sensitivity of TDTS. Instead of measuring the full electric field $E_{\text{sam}}(t)$ as a function of time at each pump-probe delay τ, we measured the change in the electric field $\Delta E_\tau(t)$ at one point in time for each pump-probe delay, as we did for graphene (chapters 5-6). Here, however, we did not measure $\Delta E_\tau(t = t_{\text{peak}})$ because the conductivity in the superconducting state is both complex and strongly frequency-dependent [Eq. (A.1); see §3.2.2]. Additionally, perturbing the superconducting state with a light

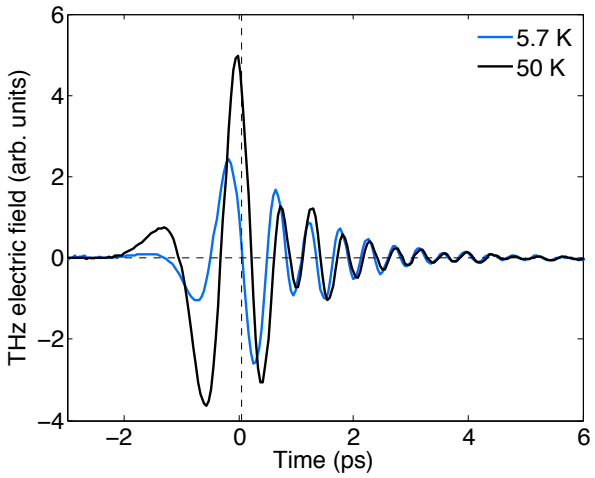

Figure A.2: Scheme for measuring pump-induced change to superfluid density. The differential field ΔE_τ at $t = t_0$ (vertical dashed line) is proportional to the photoinduced change in superfluid density $\Delta\rho_s$ [157].

pulse does not primarily change the dissipative properties of the sample, but its inductive properties, since superconductivity primarily leads to an inductive (imaginary) response in the optical conductivity [Eq. (A.1)]. Changes in the inductive response lead to changes in the phase of the transmitted pulse, so we chose a time point in the THz waveform which was maximally sensitive to this phase change.

In Fig. A.2, we display the electric field pulse transmitted through the sample $E_{\rm sam}(t)$ above T_c (50 K, black line), and below T_c (5.7 K, blue line). The phase shift between the normal state pulse and the superconducting state pulse is immediately apparent. To maximize sensitivity to changes in the phase of $E_{\rm sam}(t)$, we chose to measure $\Delta E_\tau(t = t_0)$, where t_0 is the time at which $E_{\rm sam}(t)$ at $T = 5.7$ K crosses zero, indicated by the dashed vertical line. It has been established that the photoinduced change in the electric field this time point is proportional to the photoinduced change in the imaginary part of the conductivity, and therefore to the change in the superfluid density itself [146,157]: $\Delta E_\tau(t = t_0) \propto -\Delta\rho_s(\tau)$.

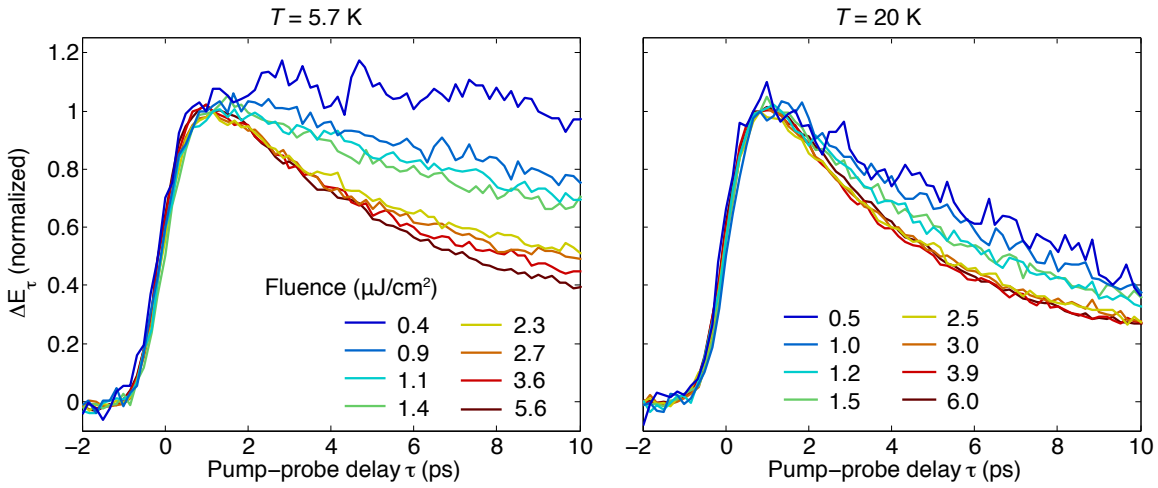

Figure A.3: Raw pump-probe data at representative temperatures. Low fluence (bluer curves) have slower decay rates than high fluence (redder curves), a hallmark of bimolecular recombination processes.

We display our measurements of $\Delta E_\tau(t = t_0)$ after optical excitation for two temperatures, both well below T_c, in Fig. A.3. Different color curves correspond to different excitation fluences. The curves have been normalized to their value at the end of the initial rapid change. At the lowest temperature, we observed a recovery with a rate that depended strongly on fluence, decreasing with decreasing fluence. At $T = 20$ K, we observed overall faster decay rates which still depended on fluence. As T increased further, the rates got even faster and the fluence dependence eventually vanished (not shown). In order to better understand these data, we focus on $\Delta E_\tau(t = t_0)$ during the first few picoseconds after excitation. The important quantity that we will consider is the recovery rate γ_0 in this short-time regime.

The initial rate γ_0 as a function of fluence at a range of temperatures is shown in Fig. A.4. There are several noteworthy features of this plot. First, in the low-excitation regime, the rate increases linearly with fluence. Second, at all temperatures, there is a finite y-intercept, which corresponds to a finite rate of recovery at zero excitation. Additionally, the

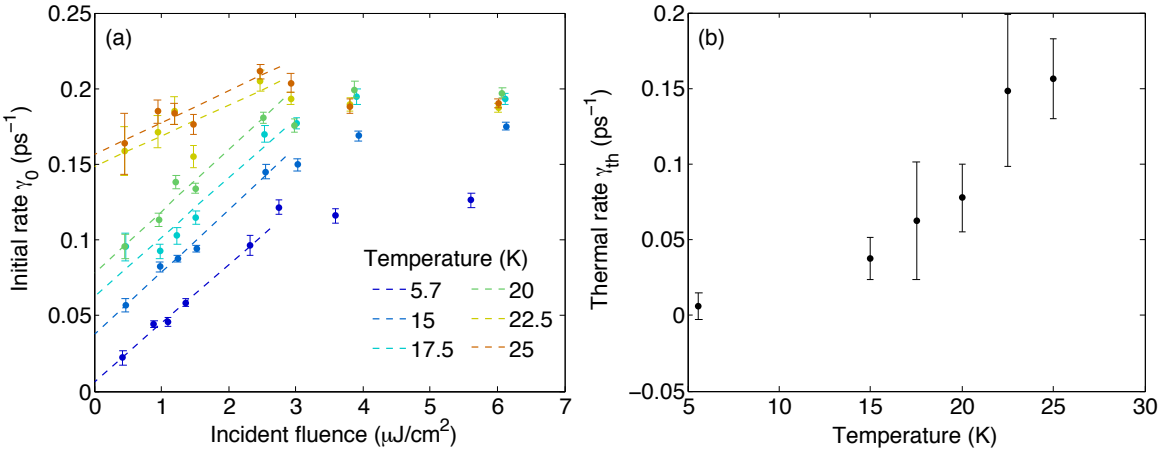

Figure A.4: (a) Initial decay rate as a function of incident fluence at different temperatures in the superconducting state. (b) Zero-fluence limit of decay rate [y-axis intercept from panel (a)], which is proportional to the thermal quasiparticle population.

slope of the fitted lines is approximately temperature independent at low temperature, but decreases at the highest temperatures. Finally, the y-intercept increases monotonically with temperature. These features provide strong evidence that the superfluid recovery proceeds by pair-wise recombination of photoexcited quasiparticles [158].

The Rothwarf-Taylor (RT) rate equations [159] can be used to understand the results presented in Fig. A.4. This set of coupled differential equations describes the coupling between the quasiparticle population n and the pairing boson population N:

$$\frac{dn}{dt} = I_{\rm qp} + 2\gamma_{\rm pc}N - \beta n^2 \tag{A.2}$$

$$\frac{dN}{dt} = \beta n^2/2 - \gamma_{\rm pc}N - \gamma_{\rm esc}(N - N_{\rm eq}). \tag{A.3}$$

Here $I_{\rm qp}$ is the external generation rate of quasiparticles (*e.g.*, by excitation with a laser pulse), $\gamma_{\rm pc}$ is the rate of quasiparticle pair creation by absorption of a phonon, and $\gamma_{\rm esc}$ is the rate at which pair-creating phonons decay into lower-energy phonons are leave the photoexcited region [158]. The time rate of change of the quasiparticle population depends on the density squared because two quasiparticles must meet in order to form a Cooper pair:

$n + n \rightarrow$ CP.

To analyze Eqs. (A.2-A.3), it is useful to separate n and N into thermal and photoexcited populations: $n = n_{\rm ph} + n_{\rm th}$ and $N = N_{\rm ph} + N_{\rm th}$. We additionally assume that $\gamma_{\rm pc}$ is small compared to the quasiparticle recombination rate [158]. At zero temperature, the thermal populations vanish, and photoexcited quasiparticles can only recombine with other photoexcited quasiparticles so that $dn/dt = -\beta n^2$ and $n_{\rm ph} + n_{\rm ph} \rightarrow$ CP is the only allowed decay process. The recovery rate $\gamma \equiv |(1/n)dn/dt| = \beta n$ then depends linearly on the density of photoexcited quasiparticles. At finite temperature, thermally generated quasiparticles open another relaxation channel for photoexcited quasiparticles. Instead of only pairing with each other, they can now also pair with the thermally present quasiparticles at a rate proportional to the thermal quasiparticle density: $n_{\rm ph} + n_{\rm th} \rightarrow$ CP. In this case, the first RT equation becomes

$$\frac{dn}{dt} = [I_{\rm qp}+2\gamma_{\rm pc}N_{\rm ph} - \beta(n_{\rm ph}^2 + 2n_{\rm th}n_{\rm ph})] + (2\gamma_{\rm pc}N_{\rm th} - \beta n_{\rm th}^2). \tag{A.4}$$

In the absence of photoexcitation, the first term in brackets vanishes. Additionally, the quasiparticles and pairing bosons should be in thermal equilibrium so that $dn/dt = (2\gamma_{\rm pc}N_{\rm th} - \beta n_{\rm th}^2) = 0 \rightarrow 2\gamma_{\rm pc}N_{\rm th} = \beta n_{\rm th}^2$. Including our previous assumption that quasiparticle recombination occurs more rapidly than pair creation, Eq. A.4 becomes (after the photoexciting pulse has passed) $dn/dt = -\beta(n_{\rm ph}^2 + 2n_{\rm th}n_{\rm ph})$. Calculating the total decay rate, we find

$$\gamma_{\rm tot} = \beta(n_{\rm ph} + 2n_{\rm th}). \tag{A.5}$$

The total initial recovery rate depends on both the thermal quasiparticle population and the photoexcited quasiparticle population. Fig. A.5 depicts the allowed recombination processes schematically.

We can now understand the temperature and excitation dependence of the initial rate [Fig. A.4(a)]. At low excitation density, $n_{\rm ph}$ increases linearly with excitation. There-

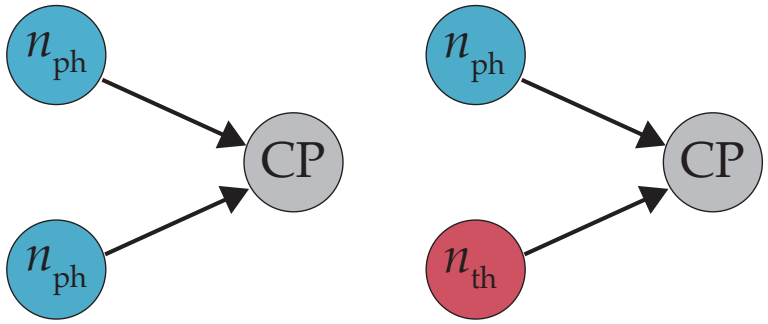

Figure A.5: Cartoon depicting different Rothwarf-Taylor recombination mechanisms. A photoexcited quasiparticles can form a Cooper pair by meeting either another photoexcited quasiparticle (left) or by meeting a thermally-generated quasiparticle (right).

fore, since the initial rate is proportional to this density, it will increase linearly with pump fluence for a fixed thermal population, which is what we observe at low temperatures. We also see that as n_{ph} tends to zero, the rate tends to a finite constant. Eq. (A.5) reveals that the intercept is proportional to the thermal quasiparticle population. We refer to this intercept as the "thermal rate" γ_{th}.

Finally, we note that this non-equilibrium measurement of the initial decay rate provides information about the equilibrium normal fluid density as a function of temperature through determination of $\gamma_{\mathrm{th}}(T)$ [Fig. A.4(b)]. Incidentally, quasiparticles in a d-wave superconductor, such as $La_{2-x}Sr_xCuO_4$, and in graphene both exhibit a Dirac dispersion, though it is anisotropic in the cuprate case [160]. As a result, both graphene and $La_{2-x}Sr_xCuO_4$ should exhibit a power law temperature dependence of the quasiparticle number density [30, 154, 160]. Indeed, a best-fit of the data in Fig. A.4(b) to a power law $\gamma_{\mathrm{th}} \propto T^{\alpha}$ yields $\alpha \sim 2$, though we clearly need finer temperature steps and greater temperature range to determine α with any degree of certainty. Note that we only fit to the first four temperature points because the fluence dependence weakens by the higher temperature points. A power law with $\alpha = 2$ has been observed in optical pump-probe measurements on

underdoped $La_{2-x}Sr_xCuO_4$ [161] and iron pnictide superconductor $Ba_{0.6}K_{0.4}Fe_2As_2$ [162]. An interesting future experiment would be to compare the temperature dependence of $\gamma_{\rm th}$ to that of the thermal quasiparticle density $n_{\rm th}(T)$ in the same sample. TDTS and OPTP are ideally suited to this sort of experiment; $n_{\rm th}(T)$ could be extracted from equilibrium TDTS measurements, while $\gamma_{\rm th}$ could be extracted from nonequilibrium OPTP experiments.

Bibliography

[1] Geim, A. K. & Novoselov, K. S. The rise of graphene. *Nat. Mater.* **6**, 183 (2007).

[2] Castro Neto, A. H., Peres, N. M. R., Novoselov, K. S. & Geim, A. K. The electronic properties of graphene. *Rev. of Mod. Phys.* **81**, 109 (2009).

[3] Das Sarma, S., Adam, S., Hwang, E. H. & Rossi, E. Electronic transport in two-dimensional graphene. *Rev. of Mod. Phys.* **83**, 407 (2011).

[4] Mak, K. F., Ju, L., Wang, F. & Heinz, T. F. Optical spectroscopy of graphene: From the far infrared to the ultraviolet. *Solid State Commun.* **152**, 1341 (2012).

[5] Mueller, T., Xia, F. & Avouris, P. Graphene photodetectors for high-speed optical communications. *Nat. Photonics* **4**, 297 (2010).

[6] Bonaccorso, F., Sun, Z., Hasan, T. & Ferrari, A. C. Graphene photonics and optoelectronics. *Nat. Photon.* **4**, 611 (2010).

[7] Koppens, F. H. L. *et al.* Photodetectors based on graphene, other two-dimensional materials and hybrid systems. *Nat. Nanotechnol.* **9**, 780 (2014).

[8] Xia, F., Mueller, T., Lin, Y.-M., Valdes-Garcia, A. & Avouris, P. Ultrafast graphene photodetector. *Nat. Nanotechnol.* **4**, 839 (2009).

[9] Gan, X. *et al.* Chip-integrated ultrafast graphene photodetector with high responsivity. *Nat. Photon.* **7**, 883 (2013).

[10] Herring, P. K. *et al.* Photoresponse of an electrically tunable ambipolar graphene infrared thermocouple. *Nano Lett.* **2**, 0–6 (2014).

[11] Horng, J. *et al.* Drude conductivity of Dirac fermions in graphene. *Phys. Rev. B* **83**, 165113 (2011).

[12] Ren, L. *et al.* Terahertz and infrared spectroscopy of gated large-area graphene. *Nano Lett.* **12**, 3711 (2012).

[13] Kim, J. Y. *et al.* Far-infrared study of substrate-effect on large scale graphene. *Appl. Phys. Lett.* **98**, 201907 (2011).

[14] Yan, H. *et al.* Infrared spectroscopy of wafer-scale graphene. *ACS Nano* **5**, 9854 (2011).

[15] Maeng, I. *et al.* Gate-controlled nonlinear conductivity of Dirac fermion in graphene field-effect transistors measured by terahertz time-domain spectroscopy. *Nano Lett.* **12**, 551 (2012).

[16] Vicarelli, L. *et al.* Graphene field-effect transistors as room-temperature terahertz detectors. *Nat. Mater.* **11**, 865 (2012).

[17] Mittendorff, M. *et al.* Ultrafast graphene-based broadband THz detector. *Appl. Phys. Lett.* **103**, 2013 (2013).

[18] Cai, X. *et al.* Sensitive room-temperature terahertz detection via the photothermoelectric effect in graphene. *Nat. Nanotechnol.* (2014).

[19] Lemme, M. C. *et al.* Gate-activated photoresponse in a graphene p-n junction. *Nano Lett.* **11**, 4134 (2011).

[20] Gabor, N. M. *et al.* Hot carrier-assisted intrinsic photoresponse in graphene. *Science* **334**, 648 (2011).

[21] Song, J. C. W., Rudner, M. S., Marcus, C. M. & Levitov, L. S. Hot carrier transport and photocurrent response in graphene. *Nano Lett.* **11**, 4688 (2011).

[22] Sun, D. *et al.* Ultrafast hot-carrier-dominated photocurrent in graphene. *Nat. Nanotechnol.* **7**, 114 (2012).

[23] Freitag, M., Low, T., Xia, F. & Avouris, P. Photoconductivity of biased graphene. *Nat. Photon.* **7**, 53 (2012).

[24] Ulbricht, R., Hendry, E., Shan, J., Heinz, T. F. & Bonn, M. Carrier dynamics in semiconductors studied with time-resolved terahertz spectroscopy. *Rev. of Mod. Phys.* **83**, 543 (2011).

[25] Beard, M. C., Turner, G. M. & Schmuttenmaer, C. A. Terahertz spectroscopy. *J. Phys. Chem. B* **106**, 7146 (2002).

[26] Nuss, M. C. & Orenstein, J. Terahertz time domain spectroscopy. In Grüner, G. (ed.) *Millimeter and Submillimeter Wave Spectroscopy of Solids*, chap. 2, 7–50 (Springer, Berlin, 1998).

[27] Lee, Y.-S. *Principles of Terahertz Science and Technology* (Springer US, 2009).

[28] Averitt, R. D. & Taylor, A. J. Ultrafast optical and far-infrared quasiparticle dynamics in correlated electron materials. *J. Phys. Condens. Matter* **14**, R1357 (2002).

[29] Ashcroft, N. W. & Mermin, N. D. *Solid State Physics* (Brooks Cole, Belmont, MA, 1976).

[30] Wallace, P. R. The band theory of graphite. *Phys. Rev.* **71**, 622 (1947).

[31] Peres, N. M. R. Colloquium: The transport properties of graphene: An introduction. *Rev. Mod. Phys.* **82**, 2673 (2010).

[32] Novoselov, K. S. *et al.* Electric field effect in atomically thin carbon films. *Science* **306**, 666 (2004).

[33] Kampfrath, T., Perfetti, L., Schapper, F., Frischkorn, C. & Wolf, M. Strongly coupled optical phonons in the ultrafast dynamics of the electronic energy and current relaxation in graphite. *Phys. Rev. Lett.* **95**, 187403 (2005).

[34] Hwang, E. H. & Das Sarma, S. Acoustic phonon scattering limited carrier mobility in two-dimensional extrinsic graphene. *Phys. Rev. B* **77**, 115449 (2008).

[35] Bistritzer, R. & MacDonald, A. Electronic cooling in graphene. *Phys. Rev. Lett.* **102**, 206410 (2009).

[36] Perebeinos, V. & Avouris, P. Inelastic scattering and current saturation in graphene. *Phys. Rev. B* **81**, 195442 (2010).

[37] Song, J. C. W., Reizer, M. Y. & Levitov, L. S. Disorder-assisted electron-phonon scattering and cooling pathways in graphene. *Phys. Rev. Lett.* **109**, 106602 (2012).

[38] Low, T., Perebeinos, V., Kim, R., Freitag, M. & Avouris, P. Cooling of photoexcited carriers in graphene by internal and substrate phonons. *Phys. Rev. B* **86**, 045413 (2012).

[39] Bolotin, K. I., Sikes, K. J., Hone, J., Stormer, H. L. & Kim, P. Temperature-dependent transport in suspended graphene. *Phys. Rev. Lett.* **101**, 096802 (2008).

[40] Dean, C. R. *et al.* Boron nitride substrates for high-quality graphene electronics. *Nat. Nanotechnol.* **5**, 722 (2010).

[41] Chen, J.-H., Jang, C., Xiao, S., Ishigami, M. & Fuhrer, M. S. Intrinsic and extrinsic performance limits of graphene devices on SiO_2. *Nat. Nanotechnol.* **3**, 206 (2008).

[42] Morozov, S. V. *et al.* Giant intrinsic carrier mobilities in graphene and its bilayer. *Phys. Rev. Lett.* **100**, 11–14 (2008).

[43] Piscanec, S., Lazzeri, M., Mauri, F., Ferrari, A. C. & Robertson, J. Kohn anomalies and electron-phonon interactions in graphite. *Phys. Rev. Lett.* **93**, 185503 (2004).

[44] Lui, C. H., Mak, K. F., Shan, J. & Heinz, T. F. Ultrafast photoluminescence from graphene. *Phys. Rev. Lett.* **105**, 127404 (2010).

[45] Freitag, M. *et al.* Energy dissipation in graphene field-effect transistors. *Nano Lett.* **9**, 1883 (2009).

[46] Berciaud, S. *et al.* Electron and optical phonon temperatures in electrically biased graphene. *Phys. Rev. Lett.* **104**, 227401 (2010).

[47] Price, A., Hornett, S., Shytov, A., Hendry, E. & Horsell, D. Nonlinear resistivity and heat dissipation in monolayer graphene. *Phys. Rev. B* **85**, 1–4 (2012).

[48] Malard, L. M., Mak, K. F., Castro Neto, A. H., Peres, N. M. R. & Heinz, T. F. Observation of intra- and inter-band transitions in the transient optical response of graphene. *New J. Phys.* **15**, 015009 (2013).

[49] Yan, H. *et al.* Time-resolved Raman spectroscopy of optical phonons in graphite: Phonon anharmonic coupling and anomalous stiffening. *Phys. Rev. B* **80**, 121403(R) (2009).

[50] Kang, K., Abdula, D., Cahill, D. G. & Shim, M. Lifetimes of optical phonons in graphene and graphite by time-resolved incoherent anti-Stokes Raman scattering. *Phys. Rev. B* **81**, 165405 (2010).

[51] Wu, S. *et al.* Hot phonon dynamics in graphene. *Nano Lett.* **12**, 5495 (2012).

[52] Chen, J.-H. *et al.* Charged-impurity scattering in graphene. *Nat. Phys.* **4**, 377 (2008).

[53] Ando, T. Screening effect and impurity scattering in monolayer graphene. *J. Phys. Soc. Jpn.* **75**, 074716 (2006).

[54] Adam, S., Hwang, E. H., Galitski, V. M. & Das Sarma, S. A self-consistent theory for graphene transport. *Proc. Natl. Acad. Sci. U.S.A.* **104**, 18392 (2007).

[55] Wooten, F. *Optical Properties of Solids* (Academic Press, New York, 1972).

[56] Basov, D. N., Averitt, R. D., van der Marel, D., Dressel, M. & Haule, K. Electrodynamics of correlated electron materials. *Rev. Mod. Phys.* **83**, 471 (2011).

[57] Dressel, M. & Grüner, G. *Electrodynamics of Solids: Optical Properties of Electrons in Matter* (Cambridge University Press, Cambridge, 2002).

[58] Drude, P. Zur elektronentheorie der metalle. *Ann. Phys.* **306**, 566 (1900).

[59] Ziman, J. M. *Principles of the Theory of Solids* (Cambridge University Press, Cambridge, 1972).

[60] Arovas, D. P. Lecture notes on condensed matter physics (2010). URL `http://physics.ucsd.edu/students/courses/winter2010/physics211b`. Accessed April 13, 2010.

[61] Frenzel, A. J. *et al.* Observation of suppressed terahertz absorption in photoexcited graphene. *Appl. Phys. Lett.* **102**, 113111 (2013).

[62] Solyom, J. *Fundamentals of the Physics of Solids* (Springer-Verlag, Berlin, 2010).

[63] Sakurai, J. J. *Modern Quantum Mechanics* (Addison Wesley, 1993).

[64] Mak, K. F. *et al.* Measurement of the optical conductivity of graphene. *Phys. Rev. Lett.* **101**, 196405 (2008).

[65] Gusynin, V. P., Sharapov, S. G. & Carbotte, J. P. On the universal ac optical background in graphene. *New J. Phys.* **11**, 095013 (2009).

[66] Nair, R. R. *et al.* Fine structure constant defines visual transparency of graphene. *Science* **320**, 1308 (2008).

[67] Li, Z. Q. *et al.* Dirac charge dynamics in graphene by infrared spectroscopy. *Nat. Phys.* **4**, 532 (2008).

[68] Wang, F. *et al.* Gate-variable optical transitions in graphene. *Science* **320**, 206 (2008).

[69] Jackson, J. D. *Classical Electrodynamics* (John Wiley & Sons, 1999), 3rd edn.

[70] Tanner, D. B. Use of x-ray scattering functions in Kramers-Kronig analysis of reflectance. *Phys. Rev. B* **91**, 035123 (2015).

[71] Gusynin, V. P., Sharapov, S. G. & Carbotte, J. P. Sum rules for the optical and Hall conductivity in graphene. *Phys. Rev. B* **75**, 165407 (2007).

[72] Kuzmenko, A. B., van Heumen, E., Carbone, F. & van der Marel, D. Universal optical conductance of graphite. *Phys. Rev. Lett.* **100**, 117401 (2008).

[73] Griffiths, D. J. *Introduction to Electrodynamics* (Prentice Hall, Upper Saddle River, 1999), 3rd edn.

[74] Boyd, R. W. *Nonlinear Optics* (Academic Press, 2008), 3rd edn.

[75] Planken, P. C. M., Nienhuys, H.-K., Bakker, H. J. & Wenckenbach, T. Measurement and calculation of the orientation dependence of terahertz pulse detection in ZnTe. *J. Opt. Soc. Am. B* **18**, 313 (2001).

[76] Fowles, G. R. *Introduction to Modern Optics* (Dover Publications, 1989), 2nd edn.

[77] Duvillaret, L., Garet, F. & Coutaz, J.-L. A reliable method for extraction of material parameters in terahertz time-domain spectroscopy. *IEEE J. Selected Topics Quantum Electron.* **2**, 739 (1996).

[78] Duvillaret, L., Garet, F. & Coutaz, J. L. Highly precise determination of optical constants and sample thickness in terahertz time-domain spectroscopy. *Appl. Opt.* **38**, 409 (1999).

[79] Beard, M. C., Turner, G. M. & Schmuttenmaer, C. A. Transient photoconductivity in GaAs as measured by time-resolved terahertz spectroscopy. *Phys. Rev. B* **62**, 15764 (2000).

[80] Beard, M. C., Turner, G. M. & Schmuttenmaer, C. A. Subpicosecond carrier dynamics in low-temperature grown GaAs as measured by time-resolved terahertz spectroscopy. *J. Appl. Phys.* **90**, 5915 (2001).

[81] Suzuki, T. & Shimano, R. Cooling dynamics of photoexcited carriers in Si studied using optical pump and terahertz probe spectroscopy. *Phys. Rev. B* **83**, 085207 (2011).

[82] Averitt, R. D. *et al.* Nonequilibrium superconductivity and quasiparticle dynamics in $YBa_2Cu_3O_{7-\delta}$. *Phys. Rev. B* **63**, 140502 (2001).

[83] Kaindl, R. A., Carnahan, M. A., Chemla, D. S., Oh, S. & Eckstein, J. N. Dynamics of Cooper pair formation in $Bi_2Sr_2CaCu_2O_{8+\delta}$. *Phys. Rev. B* **72**, 060510 (2005).

[84] Beck, M. *et al.* Energy-gap dynamics of superconducting NbN thin films studied by time-resolved terahertz spectroscopy. *Phys. Rev. Lett.* **107**, 177007 (2011).

[85] Jnawali, G., Rao, Y., Yan, H. & Heinz, T. F. Observation of a transient decrease in terahertz conductivity of single-layer graphene induced by ultrafast optical excitation. *Nano Lett.* **13**, 524 (2013).

[86] Tielrooij, K. J. *et al.* Photoexcitation cascade and multiple hot-carrier generation in graphene. *Nat. Phys.* **9**, 248 (2013).

[87] Grischkowsky, D., Keiding, S., van Exter, M. & Fattinger, C. Far-infrared time-domain spectroscopy with terahertz beams of dielectrics and semiconductors. *J. Opt. Soc. Am. B* **7**, 2006 (1990).

[88] Frenzel, A. J., Lui, C. H., Shin, Y. C., Kong, J. & Gedik, N. Semiconducting-to-metallic photoconductivity crossover and temperature-dependent drude weight in graphene. *Phys. Rev. Lett.* **113**, 056602 (2014).

[89] Suzuki, T. & Shimano, R. Time-resolved formation of excitons and electron-hole droplets in Si studied using terahertz spectroscopy. *Phys. Rev. Lett.* **103**, 057401 (2009).

[90] Kindt, J. T. & Schmuttenmaer, C. A. Theory for determination of the low-frequency time-dependent response function in liquids using time-resolved terahertz pulse spectroscopy. *J. Chem. Phys.* **110**, 8589 (1999).

[91] Beard, M. C. & Schmuttenmaer, C. A. Using the finite-difference time-domain pulse propagation method to simulate time-resolved THz experiments. *J. Chem. Phys.* **114**, 2903 (2001).

[92] Larsen, C., Cooke, D. G. & Jepsen, P. U. Finite-difference time-domain analysis of time-resolved terahertz spectroscopy experiments. *J. Opt. Soc. Am. B* **28**, 1308 (2011).

[93] Gallot, G., Zhang, J., McGowan, R. W., Jeon, T.-I. & Grischkowsky, D. Measurements of the THz absorption and dispersion of ZnTe and their relevance to the electro-optic detection of THz radiation. *Appl. Phys. Lett.* **74**, 3450 (1999).

[94] Nahata, A., Weling, A. S. & Heinz, T. F. A wideband coherent terahertz spectroscopy system using optical rectification and electro-optic sampling. *Appl. Phys. Lett.* **69**, 2321 (1996).

[95] Shan, J., Nahata, A. & Heinz, T. F. Terahertz time-domain spectroscopy based on nonlinear optics. *J. Nonlinear Opt. Phys. Mater.* **11**, 31 (2002).

[96] Yee, K. S. Numerical solution of initial boundary value problems involving Maxwell's equations. *IEEE Trans. Antennas Propag.* **AP-14**, 302 (1966).

[97] Taflove, A. & Hagness, S. C. *Computational Electrodynamics: The Finite-Difference Time-Domain Method* (Artech House, Norwood, MA, 2005), 3rd edn.

[98] Dubin, D. *Numerical and Analytical Methods for Scientists and Engineers, Using Mathematica* (Wiley-Interscience, 2003).

[99] Rumpf, R. C. Electromagnetic analysis using finite-difference time-domain (2014). URL `http://emlab.utep.edu/ee5390fdtd.htm`. Accessed April 16, 2014.

[100] Schneider, J. B. Understanding the finite-difference time-domain method (2014). URL `http://www.eecs.wsu.edu/ schneidj/ufdtd/ufdtd.pdf`. Accessed May 9, 2014.

[101] Körner, T. O. & Fichtner, W. Auxiliary differential equation: efficient implementation in the finite-difference time-domain method. *Opt. Lett.* **22**, 1586 (1997).

[102] Yang, Y., Shutler, A. & Grischkowsky, D. Measurement of the transmission of the atmosphere from 0.2 to 2 THz. *Opt. Express* **19**, 8830 (2011).

[103] Werley, C. A., Teo, S. M. & Nelson, K. A. Pulsed laser noise analysis and pump-probe signal detection with a data acquisition card. *Rev. Sci. Inst.* **82**, 123108 (2011).

[104] Yeh, K.-L. *The generation of high field terahertz radiation and its application in terahertz nonlinear spectroscopy.* Ph.D. thesis, Massachusetts Institute of Technology (2009).

[105] Iwaszczuk, K., Cooke, D. G., Fujiwara, M., Hashimoto, H. & Jepsen, P. U. Simultaneous reference and differential waveform acquisition in time-resolved terahertz spectroscopy. *Opt. Exp.* **17**, 21969 (2009).

[106] George, P. A. *et al.* Ultrafast optical-pump terahertz-probe spectroscopy of the carrier relaxation and recombination dynamics in epitaxial graphene. *Nano Lett.* **8**, 4248 (2008).

[107] Choi, H. *et al.* Broadband electromagnetic response and ultrafast dynamics of few-layer epitaxial graphene. *Appl. Phys. Lett.* **94**, 172102 (2009).

[108] Strait, J. H. *et al.* Very slow cooling dynamics of photoexcited carriers in graphene observed by optical-pump terahertz-probe spectroscopy. *Nano Lett.* **11**, 4902 (2011).

[109] Li, X. *et al.* Large-area synthesis of high-quality and uniform graphene films on copper foils. *Science* **324**, 1312 (2009).

[110] Malard, L. M., Pimenta, M. A., Dresselhaus, G. & Dresselhaus, M. S. Raman spectroscopy in graphene. *Phys. Rep.* **473**, 51 (2009).

[111] Lee, C. *et al.* Optical response of large scale single layer graphene. *Appl. Phys. Lett.* **98**, 071905 (2011).

[112] Butscher, S., Milde, F., Hirtschulz, M., Malić, E. & Knorr, A. Hot electron relaxation and phonon dynamics in graphene. *Appl. Phys. Lett.* **91**, 203103 (2007).

[113] Barreiro, A., Lazzeri, M., Moser, J., Mauri, F. & Bachtold, A. Transport properties of graphene in the high-current limit. *Phys. Rev. Lett.* **103**, 076601 (2009).

[114] Chae, D.-H., Krauss, B., von Klitzing, K. & Smet, J. H. Hot phonons in an electrically biased graphene constriction. *Nano Lett.* **10**, 466 (2010).

[115] Hwang, H. Y. *et al.* Nonlinear THz conductivity dynamics in *p*-type CVD-grown graphene. *J. Phys. Chem. B* **117**, 15819 (2013).

[116] Jensen, S. A. *et al.* Competing ultrafast energy relaxation pathways in photoexcited graphene. *Nano Letters* **14**, 5839 (2014).

[117] Docherty, C. J. *et al.* Extreme sensitivity of graphene photoconductivity to environmental gases. *Nat. Commun.* **3**, 1228 (2012).

[118] Winnerl, S. *et al.* Carrier relaxation in epitaxial graphene photoexcited near the Dirac pdddoint. *Phys. Rev. Lett.* **107**, 237401 (2011).

[119] Kim, J. *et al.* Ultrafast zero balance of the oscillator-strength sum rule in graphene. *Scientific Reports* **3**, 2663 (2013).

[120] Wu, W. F., Chiou, B. S. & Hsieh, S. T. Effect of sputtering power on the structural and optical properties of magnetron sputtered ITO films. *Semicond. Sci. Technol.* **9**, 1242 (1994).

[121] Bender, M. *et al.* Dependence of oxygen flow on optical and electrical properties of DC-magnetron sputtered ITO films. *Thin Solid Films* **326**, 72 (1998).

[122] Li, Z. Q. *et al.* Light Quasiparticles Dominate Electronic Transport in Molecular Crystal Field-Effect Transistors. *Phys. Rev. Lett.* **99**, 016403 (2007).

[123] de Boer, R. W. I., Gershenson, M. E., Morpurgo, A. F. & Podzorov, V. Organic single-crystal field-effect transistors. *Phys. Status Solidi* **201**, 1302 (2004).

[124] Kahouli, A. *et al.* Structural and dielectric study of parylene C thin films. *Appl. Phys. Lett.* **94**, 152901 (2009).

[125] Herzinger, C. M., Johs, B., McGahan, W. A., Woollam, J. A. & Paulson, W. Ellipsometric determination of optical constants for silicon and thermally grown silicon dioxide via a multi-sample, multi-wavelength, multi-angle investigation. *J. Appl. Phys.* **83**, 3323 (1998).

[126] Averitt, R. D., Rodriguez, G., Siders, J. L. W., Trugman, S. A. & Taylor, A. J. Conductivity artifacts in optical-pump THz-probe measurements of $YBa_2Cu_3O_7$. *J. Opt. Soc. Am. B* **17**, 327 (2000).

[127] Liu, X. *et al.* Metamaterials on parylene thin film substrates: Design, fabrication, and characterization at terahertz frequency. *Appl. Phys. Lett.* **96**, 011906 (2010).

[128] Breusing, M. *et al.* Ultrafast nonequilibrium carrier dynamics in a single graphene layer. *Phys. Rev. B* **83**, 153410 (2011).

[129] Brida, D. *et al.* Ultrafast collinear scattering and carrier multiplication in graphene. *Nat. Commun.* **4**, 1987 (2013).

[130] Johannsen, J. C. *et al.* Direct view of hot carrier dynamics in graphene. *Phys. Rev. Lett.* **111**, 027403 (2013).

[131] Gierz, I. *et al.* Snapshots of non-equilibrium Dirac carrier distributions in graphene. *Nat. Mater.* **12**, 1119 (2013).

[132] Müller, M., Bräuninger, M. & Trauzettel, B. Temperature dependence of the conductivity of ballistic graphene. *Phys. Rev. Lett.* **103**, 196801 (2009).

[133] Wagner, M. *et al.* Ultrafast and nanoscale plasmonic phenomena in exfoliated graphene revealed by infrared pumpâĂŞprobe nanoscopy. *Nano Letters* **14**, 894 (2014).

[134] Kim, S. *et al.* Realization of a high mobility dual-gated graphene field-effect transistor with Al_2O_3 dielectric. *Appl. Phys. Lett.* **94**, 062107 (2009).

[135] Fratini, S. & Guinea, F. Substrate-limited electron dynamics in graphene. *Phys. Rev. B* **77**, 195415 (2008).

[136] Hwang, E. H. & Das Sarma, S. Screening-induced temperature-dependent transport in two-dimensional graphene. *Phys. Rev. B* **79**, 165404 (2009).

[137] Stauber, T., Peres, N. M. R. & Guinea, F. Electronic transport in graphene: A semiclassical approach including midgap states. *Phys. Rev. B* **76**, 205423 (2007).

[138] Graham, M. W. *et al.* Transient absorption and photocurrent microscopy show that hot electron supercollisions describe the rate-limiting relaxation step in graphene. *Nano Lett.* **13**, 5497 (2013).

[139] Keimer, B., Kivelson, S. A., Norman, M. R., Uchida, S. & Zaanen, J. From quantum matter to high-temperature superconductivity in copper oxides. *Nature* **518**, 179 (2015).

[140] Nuss, M. C., Mankiewich, P. M., O'Malley, M. L. & Westerwick, E. H. Dynamic conductivity and "coherence peak" in $YBa_2Cu_3O_7$ superconductors. *Phys. Rev. Lett.* **66**, 3305 (1991).

[141] Spielman, S. *et al.* Observation of quasiparticle Hall effect in superconducting $YBa_2Cu_3O_{7-\delta}$. *Phys. Rev. Lett.* **73**, 1537 (1994).

[142] Parks, B. *et al.* Phase-sensitive measurements of vortex dynamics in the terahertz domain. *Phys. Rev. Lett.* **74**, 3265 (1995).

[143] Brorson, S. D. *et al.* Electrodynamics of high-temperature superconductors investigated with coherent terahertz pulse spectroscopy. *J. Opt. Soc. Am. B* **13**, 1979 (1996).

[144] Thorsmølle, V. K., Averitt, R. D., Shibauchi, T., Hundley, M. F. & Taylor, A. J. Dynamic coupling-decoupling crossover in the current-driven vortex state in $Tl_2Ba_2CaCu_2O_8$ probed by the Josephson plasma resonance. *Phys. Rev. Lett.* **97**, 237001 (2006).

[145] Nakamura, D., Shibuya, Y., Imai, Y., Maeda, A. & Tsukada, I. Superconducting fluctuation proved by time-domain THz spectroscopy of $La_{1.85}Sr_{0.15}CuO_4$ thin film. *Physica C* **470**, S47 (2010).

[146] Beyer, M. *et al.* Photoinduced melting of superconductivity in the high-T_c superconductor $La_{2-x}Sr_xCuO_4$ probed by time-resolved optical and terahertz techniques. *Phys. Rev. B* **83**, 214515 (2011).

[147] Bilbro, L. S. *et al.* Temporal correlations of superconductivity above the transition temperature in $La_{2-x}Sr_xCuO_4$ probed by terahertz spectroscopy. *Nat. Phys.* **7**, 298 (2011).

[148] Bilbro, L. S., Valdés Aguilar, R., Logvenov, G., Bozovic, I. & Armitage, N. P. On the possibility of fast vortices in the cuprates: A vortex plasma model analysis of THz conductivity and diamagnetism in $La_{2-x}Sr_xCuO_4$. *Phys. Rev. B* **84**, 100511 (2011).

[149] Fausti, D. *et al.* Light-induced superconductivity in a stripe-ordered cuprate. *Science* **331**, 189 (2011).

[150] Lubashevsky, Y., Pan, L., Kirzhner, T., Koren, G. & Armitage, N. P. Optical birefringence and dichroism of cuprate superconductors in the THz regime. *Phys. Rev. Lett.* **112**, 147001 (2014).

[151] Hashimoto, M., Vishik, I. M., He, R.-h., Devereaux, T. P. & Shen, Z.-X. Energy gaps in high-transition-temperature cuprate superconductors. *Nat. Phys.* **10**, 483 (2014).

[152] Corson, J., Mallozzi, R., Orenstein, J., Eckstein, J. N. & Bozovic, I. Vanishing of phase coherence in underdoped $Bi_2Sr_2CaCu_2O_{8+\delta}$. *Nature* **398**, 221 (1999).

[153] Yoshida, T. *et al.* Universal versus material-dependent two-gap behaviors of the high-Tc cuprate superconductors: Angle-resolved photoemission study of $La_{2-x}Sr_xCuO_4$. *Phys. Rev. Lett.* **103**, 037004 (2009).

[154] Tinkham, M. *Introduction to Superconductivity* (Dover, 1996), 2nd edn.

[155] Hong, T., Heo, S. J., Kim, J. H. & Bozovic, I. Time-domain terahertz spectroscopy of $LaSrAlO_4$. In *34th Int. Conf. Infrared, Millimeter, Terahertz Waves*, 1–2 (2009).

[156] Clayhold, J. A. *et al.* Statistical characterization and process control for improved growth of $La_{2-x}Sr_xCuO_4$ films. *J. Supercond. Nov. Magn.* **22**, 797 (2009).

[157] Demsar, J. *et al.* Pair-breaking and superconducting state recovery dynamics in MgB_2. *Phys. Rev. Lett.* **91**, 267002 (2003).

[158] Gedik, N. *et al.* Single-quasiparticle stability and quasiparticle-pair decay in $YBa_2Cu_3O_{6.5}$. *Phys. Rev. B* **70**, 014504 (2004).

[159] Rothwarf, A. & Taylor, B. N. Measurement of recombination lifetimes in superconductors. *Phys. Rev. Lett.* **19**, 27 (1967).

[160] Lee, P. A. & Wen, X.-G. The unusual superconducting state of underdoped cuprates. *Phys. Rev. Lett.* **78**, 4111 (1997).

[161] Mahmood, F. Private communication.

[162] Torchinsky, D. H., Chen, G. F., Luo, J. L., Wang, N. L. & Gedik, N. Band-dependent quasiparticle dynamics in single crystals of the $Ba_{0.6}K_{0.4}Fe_2As_2$ superconductor revealed by pump-probe spectroscopy. *Phys. Rev. Lett.* **105**, 027005 (2010).